Important Notice

UNIVERSITY OF CALGARY

Computational and practical developments in single- and multi-component inverse scattering series internal multiple prediction

by

Jian Sun

A THESIS

SUBMITTED TO THE FACULTY OF GRADUATE STUDIES

IN PARTIAL FULFILLMENT OF THE REQUIREMENTS FOR THE

DEGREE OF DOCTOR OF PHILOSOPHY

GRADUATE PROGRAM IN GEOLOGY AND GEOPHYSICS

CALGARY, ALBERTA

May, 2018

Abstract

Prediction and removal of internal multiples, especially those caused by unknown generators and with insufficient subsurface information, remains a very high priority research problem in seismic data processing. Inverse scattering series internal multiple predictions are data-driven approaches to prediction in which lower-order reflected events are combined nonlinearly according to well-defined ordering relationships in vertical travel time or pseudo-depth. Implementations of instances of this algorithm in any one of the applicable transform domains encounter computational challenges and challenges caused by the practicalities of field data. In this thesis I systematically examine, develop and refine inverse scattering series internal multiple prediction algorithms and their computer implementations, introducing new ideas concerning calculation domain, search parameter optimization, artifact suppression, and computational cost reduction. A key step in my strategy is to formulate the computation in the horizontal slowness, plane-wave, domains, which is possible because of the clear relationship between horizontal slowness and wavenumber. Numerical and analytic arguments indicate that these domains, which tend to involve sparse representations input events (e.g., primary reflections), is able to proceed with a relatively stationary search parameter value, producing predictions with little numerical noise, suppression of some common high-angle prediction artifacts, and, importantly, at significantly lower computational cost. I next formulate multidimensional internal multiple prediction in 2D in the coupled plane wave domain, and examine its numerical behaviour using a benchmark synthetic dataset. In particular I show a detailed input data preparation workflow. The application of the algorithm to common-midpoint (CMP) gathers requires a modified version of the algorithm, and this is also examined. This is important for efficient prediction of internal multiples caused by dipping strata, because the so-called 1.5D formulation, nominally appropriate only for layered media, can be applied with surprising accuracy to CMP gathers over dipping in-

terfaces. I demonstrate and provide a rationale for this observation. The most significant contribution of this thesis is to analyze and numerically implement the fully elastic form of the inverse scattering series internal multiple algorithm. Theory for this has been in existence since the 1990s, but to date neither implementation nor numerical analyses of any kind have been published. Here the ordering of input data events in pseudo-depth/vertical-traveltime and the relationships between these and the actual depths at which reflections took place is key to obtaining accurate multicomponent predictions. After a full analysis, a plane-wave formulation of the elastic multicomponent inverse scattering series internal multiple prediction algorithm is also introduced. Three candidate approaches are considered for input data preparation: pre-stack Stolt migration, vertical traveltime stretching, and incorporation of best-fit reference velocities. With numerical simulations and analysis, I conclude that: (1) best-fit reference velocities produce the best approximate solution obeying the ordering (travel-time monotonicity) requirement, but it requires a relative large search parameter to be chosen in practice; (2) a combination of vertical traveltime stretching and best-fit reference velocities allows the search parameter to be the chosen with a size comparable to those used in acoustic prediction, while correctly predicting all orders of internal multiples. The first numerical examples of multicomponent elastic internal multiple prediction are then presented.

Preface

The PhD thesis is written in manuscript-based format based on one technical report, one published papers, and two manuscript papers that are ready to be submitted. I am the first author of these papers. All of these work is carried out under the supervision of Dr. Kris Innanen of CREWES project at University of Calgary. Dr. Kris Innanen was involved in all of my research projects as the supervisory author.These papers are republished in this thesis with the permission from the co-authors.

Chapter 2 is an edited version of a technical report: Jian Sun and Kristopher A. Innanen (2016). Literature review and discussions of inverse scattering series on internal multiple prediction. CREWES Report, 28, 1-25.

Chapter 3 is a paper published as: Jian Sun and Kristopher A. Innanen (2018). Multi-dimensional inverse-scattering series internal multiple prediction in the coupled plane-wave domain. GEOPHYSICS, 83(2), V73-V82.

A version of chapter 4 is going to be submitted for publication: Jian Sun and Kristopher A. Innanen, Inverse scattering series internal multiple prediction on CMP gather.

A version of chapter 5 has been submitted as: Jian Sun and Kristopher A. Innanen (2018), A plane-wave formulation of elastic multicomponent inverse scattering series internal multiple prediction. GEOPHYSICS.

Acknowledgments

Firstly, I would like to express my sincere gratitude to my supervisor Dr. Kris A. Innanen for the continuous support of my Ph.D study and related research, for his patience, motivation, and immense knowledge. His guidance helped me in all the time of research and writing of this thesis. I could not have imagined having a better advisor and mentor for my Ph.D study.

Besides, I also would like to thank Dr. Gary Margrave who is an excellent teacher and patient mentor. I learned tremendous knowledges of geophysics in seismic processing and from his courses. And I also am very grateful for his guidance, patience, and weekly practices for my candidacy examination. I also thank Dr. Daniel Trad for his suggestions and help on high-resolution Radon transform. Thanks to Dr. Larry Lines for his insightful comments and encouragement. Special thanks to Laura Baird, who's always been there for supporting all CREWES students, taking care of all non-academic stuff, which allows me focusing on my research. Thanks also to Kevin Hall, Kevin Bertram, Helen Isaac, and Pat Daley for helping me with programing, forward modeling codes, processing and softwares. I gratefully acknowledge funding sources that made my Ph.D. work possible, the sponsors of Consortium for Research in Elastic Wave Exploration Seismology (CREWES) for continued support and the Natural Science and Engineering Research Council of Canada (NSERC) through the grant CRDPJ 461179-13.

I would like to thank all CREWES members, staff, students for such a stimulating research environment. My grateful thanks to Yu Geng, Raul Cova, Sergio Romahn, Scott Keating, Zhan Niu for those creative and valuable suggestions and discussions. Thanks to my labmates, Wenyong Pan, Shahpoor Moradi, Junxiao Li, Winnie Ajiduah. It's fun and my pleasure to have spent all past years with you. I also benefited from amount of people in China, Tiansheng Chen from SINOPEC, Shengjun Li from CNPC, Chuntan Han from

NIEER, for their encouragement and supports.

Many thanks go to other Chinese fellows at CREWES, Pan Pan, Bona Wu, Huaizheng Chen, Lei Yang, Yu Geng, Siming Lv and so on for their priceless friendship, for the food we cooked and eat, for the time we spent. I also appreciate the people who have communicated with me on my publications, by email or in person.

Last but not the least, I would like to thank my family: my parents (Yunkun Sun and Changqin Chen) and my sister (Li Sun) for supporting me spiritually throughout writing this thesis and my life in general. Thank my girlfriend (Kiki Xu) for her encouragement, support and always being there for me.

Dedication

To my parents and my girlfriend.

Contents

List of Tables

List of Figures

List of Symbols, Abbreviations and Nomenclature

Symbols	Definition
x	Offset or distance
x_s	Source coordinate
x_g	Receiver coordinate
x_M	Reference/midpoint coordinate
x_{sM}	Distance between source and midpoint
x_{gM}	Distance between receiver and midpoint
v_p	P-wave velocity
v_s	S-wave velocity
c_0^I	Reference velocity associated with wave-type I
v_b^{mn}	Best-fit velocity associated with downgoing wave-type n and upgoing wave-type m
ω	Angular frequency
t	Two-way traveltime
τ_0	Two-way zero-offset traveltime
τ	Two-way vertical traveltime
$\tilde{\tau}$	Two-way vertical traveltime in the reference medium
z_{si}	Thickness of ith layer below source location
z_{gi}	Thickness of ith layer below receiver location
z_{Mi}	Thickness of ith layer below midpoint location
$\tilde{z}$	Pseudo-depth: depth in the reference medium
$\tilde{z}_{stolt}$	Stolt-depth: depth obtained by Stolt migration with constant reference velocities
$\tilde{z}_b$	Pseudo-depth related to best-fit velocity
θ_s^I	Angle between incident wave and vertical direction, associated with wave-type I
θ_g^I	Angle between reflect wave and vertical direction, associated with wave-type I

k	Wavenumber
k_x	Horizontal component of wavenumber
k_s	Horizontal wavenumber associated with source coordinate
k_g	Horizontal wavenumber associated with receiver coordinate
ν	Vertical component of wavenumber
ν_s	Vertical wavenumber associated with source coordinate
ν_g	Vertical wavenumber associated with receiver coordinate
p	Horizontal slowness
p_s	Horizontal slowness associated with source coordinate
p_g	Horizontal slowness associated with receiver coordinate
p_H	Average horizontal slowness
p_m	Horizontal slowness associated with midpoint coordinate
p_h	Horizontal slowness associated with half-offset
q	Vertical slowness associated with p_X
q_s	Vertical slowness associated with source coordinate
q_g	Vertical slowness associated with receiver coordinate
$\tilde{q_s}$	Pseudo-vertical slowness associated with source coordinate and best-fit velocity
$\tilde{q_g}$	Pseudo-vertical slowness associated with receiver coordinate and best-fit velocity
d	Seismic recorded data in source/receiver/time coordinates
$\hat{d}$	Seismic recorded data in source/receiver/frequency coordinates
D	Couple plane-wave transformed data
$\hat{D}$	Couple plane-wave transformed data in frequency domain
b_1	Input for prediction algorithm
b_3	Internal multiple prediction for 1st-leading order
b_5	Internal multiple prediction for 2nd-leading order
ϵ	Searching optimum parameter

δ	Delta function
σ_{ij}, e_{ij}	Stress and strain tensor, $i, j = 1, 2, 3$
ρ, ρ_0	Density in actual and reference medium, respectively
λ, λ_0	*Lamé constants* in actual and reference medium, respectively
γ, γ_0	P-wave modulus in actual and reference medium, respectively
μ, μ_0	S-wave modulus in actual and reference medium, respectively
a_ρ a_γ a_ν	Perturbations for density, P-wave modulus, and S-wave modulus, respectively
$\mathcal{D}$	Dilatation
∇	Laplacian operator
∂	Partial derivative operator
$\vec{\boldsymbol{\sigma}}$	Stress matrix notation
$\mathbf{r}$	Coordinate vector (x, y, z)
$\boldsymbol{\mathcal{F}}$	Body force
$\mathbf{u}$	Particle displacement vector
$\boldsymbol{\mathfrak{L}}$	Wave propagating operator of actual medium in $x-$, $y-$, $z-$ components
$\boldsymbol{\mathfrak{L}}_D$	Decomposed wave propagating operator of actual medium in P- and S-wave modes
$\boldsymbol{\mathcal{L}}$	Decomposed wave propagating operator of actual medium in P-, SH-, SV-wave modes
$\boldsymbol{\mathfrak{L}}_0$	Wave propagating operator of reference medium in $x-$, $y-$, $z-$ components
$\boldsymbol{\mathfrak{L}}_{0D}$	Decomposed wave propagating operator of reference medium in P- and S-wave modes
$\boldsymbol{\mathcal{L}}_0$	Decomposed wave propagating operator of reference medium in P-, SH-, SV-wave modes
$\boldsymbol{\mathcal{G}}$	Green function of actual medium in $x-$, $y-$, $z-$ components
$\boldsymbol{\mathcal{G}}_D$	Decomposed Green function of actual medium in P- and S-wave modes
$\boldsymbol{G}$	Decomposed Green function of actual medium in P-, SH-, SV-wave modes
$\boldsymbol{\mathcal{G}}_0$	Green function of reference medium in $x-$, $y-$, $z-$ components
$\boldsymbol{\mathcal{G}}_{0D}$	Decomposed Green function of reference medium in P- and S-wave modes
$\boldsymbol{G}_0$	Decomposed Green function of reference medium in P-, SH-, SV-wave modes

$\boldsymbol{\mathcal{V}}$	Elastic scattering potential in $x-$, $y-$, $z-$ components
$\mathbf{V}$	Decomposed elastic scattering potential in P-, SH-,SV-wave modes
$\boldsymbol{\phi}$	Scalar potential of particle displacement
$\boldsymbol{\psi}$	Vector potential of particle displacement
$\boldsymbol{\Phi}$	Scalar potential of body force
$\boldsymbol{\Psi}$	Vector potential of body force
$\boldsymbol{\Pi}$	Partial derivative matrices
$\boldsymbol{\Pi}_i$	Partial derivative matrix for incident wave
$\boldsymbol{\Pi}_r$	Partial derivative matrix for reflected wave
$\boldsymbol{E}$	Rotation matrices
$\boldsymbol{E}_i$	Rotation matrix for incident wave
$\boldsymbol{E}_r$	Rotation matrix for reflected wave

Abbreviations	Definition
1.5D	Layered case
2D	Two dimensional
3D	Three dimensional
P-wave	Primary wave, compressional wave or longitudinal wave
S-wave	Secondary wave, shear wave, or transverse wave
SH-wave	Shear-horizontal wave
SV-wave	Shear-vertical wave
$\acute{P}$	Upgoing P-wave
$\grave{P}$	Downgoing P-wave
$\acute{S}$	Upgoing S-wave
$\grave{S}$	Downgoing S-wave
Pr	Primary events
IM	Internal multiple events
CMP	Common-midpoint
CFP	Common-focal-point
LRT	Linear Radon transform
HRT	Hyperbolic Radon transform
ERT	Elliptical Radon transform
RMS	Root mean square
IRLS	Iterative re-weighted least squares
RTM	Reverse time migration
FWI	Full waveform inversion
τ-p	Slant stack or linear plane-wave transform
τ-p_s-p_g	Coupled plane wave transform over source/receiver/time coordinates
τ-p_h-p_m	Coupled plane wave transform over offset/midpoint/time coordinates

Chapter 1

Introduction

1.1 Motivations

In seismic records, special events, experiencing at least one downward reflection, are called multiples which are classified as being either surface-related or interbed (internal), distinguished by their interaction (or lack of interaction) with the free-surface. The order of internal multiples refers to the number of downward reflections it experiences. Prediction and removal of internal or interbed multiples is an increasingly high priority problem in seismic data analysis. One reason for the growth of its role and importance comes from the increased sensitivity with which primary amplitudes in quantitative interpretation are now analyzed. But the importance of accurate and robust prediction of internal multiples may now be on the verge of an even greater upward jump, as full waveform methods come online.

This is counterintuitive at first, because the philosophy of full waveform methods (e.g., full waveform inversion, or FWI) is to treat the entire wave field at once, as a single, unified entity, rather than as a collection of event types (e.g., surface waves, direct arrivals, primary reflections, multiples). If we think of ourselves as working with one complex, undifferentiated wave field, why might we still need to distinguish between primaries and multiples, or any set of event types?

The behavior of FWI and least-squares algorithms tends to be determined through residuals: differences between measured data and modeled data. Updates in the Earth model (in the case of FWI) are decided based on the residuals, as are criteria for stopping the iterations, and so on. One speaks of expending effort to shrink the residuals, but in a seismic data set, where meaningful amplitude differences between modeled and measured waves can exist over an enormous dynamic range, merely finding that the residuals have shrunk may

not be enough to judge the value of an iteration or update. A reduction in residuals could be really good news if it is associated with wave events whose propagation paths include zones of interest, but it could also be close to irrelevant if associated with parts of the Earth that are of less interest or if seismic data being inverted contain arrivals unrelated to Earth properties (eg., wind noise, traffic noise, marine wave height, and so on). Furthermore, a small reduction in residuals could be better than a large reduction in residuals if the former is associated with events that have low amplitudes, and the latter is associated with events with large amplitudes. The importance of a change in the residuals could depend critically on the nature of the event in which the residual is reduced. No matter how full-waveform the processing community becomes in the future, having (at least as auxiliary information) detailed knowledge of what event type occurs in the data at specified time will be a critical technology. I do not consider specific uses of internal multiples in this thesis, but it should be emphasized that removal is just one possible approach. For instance, internal multiples can in principle be used to form seismic images (Schuster et al., 2004; Malcolm and de Hoop, 2005; Malcolm et al., 2009; Slob et al., 2014; Zuberi and Alkhalifah, 2014b,a) in the context of scattering theory.

1.2 Background

Given these motivations, what kind of internal multiple prediction/removal technology should we focus on? First, a quick review. Multiples are classified as being either surface-related or interbed, distinguished by their interaction (or lack of interaction) with the free-surface. Surface-related multiples can be eliminated because of their periodic character and deterministic predictability, especially in $\tau - p$ domain. Many innovative technologies have been developed to do so, such as predictive deconvolution (Peacock and Treitel, 1969; Taner, 1980; Treitel et al., 1982), inverse approach using feedback model (Verschuur, 1991; Verschuur et al., 1992), invariant embedding technique (Liu et al., 2000), and inverse data processing

(Berkhout and Verschuur, 2005; Berkhout, 2006).

Here I focus on the prediction/removal of interbed or internal multiples. In practice, this remains a major challenge – especially on land data – even though considerable progress has been made recently. Kelamis et al. (2002) introduced a boundary-related/layer-related approach to attenuate internal multiples in the post-stack data (CMP domain). Berkhout (2006) extended inverse data processing to attenuate internal multiples by considering them to be effective surface-related multiples through the boundary-related/layer-related approach in common-focus-point (CFP) domain. The same algorithm was applied by Luo et al. (2007), through re-datuming the top of the multiple generators and transforming internal multiples to be suppositional surface-related. However, these approaches, while powerful, all require significant subsurface knowledge. Multiple prediction and/or removal without a complete knowledge of the velocity structure will almost certainly be required to identify seismic event types before the application of full waveform processing methods, however, the options to perform multiple prediction and/or removal under such circumstances are limited.

1.3 Inverse scattering series internal multiple prediction

Inverse scattering series internal multiple technology leverages the fact that all internal multiples can be estimated through the correct combination of amplitudes and arrival times of primary reflection subevents which satisfy a certain lower-higher-lower relationship in pseudo-depth (Araújo, 1994; Weglein et al., 1997), with generators sought for in the data, in a stepwise and automatic way. This means the primaries will remain intact and no subsurface information is required. In this section, to better understand the problems existing in application of inverse scattering series internal multiple prediction, a theoretical brief review is made.

The Born series states that the propagating wavefield $\boldsymbol{G}$ in an actual medium can be expressed as a series expansion in terms of Green's function $\boldsymbol{G}_0$ in the reference medium and

scattering potential $\boldsymbol{V}$ which indicates the parameters' difference between the actual and reference medium. In matrix notation, it is written as

$$\boldsymbol{G} = \boldsymbol{G}_0 + \boldsymbol{G}_0\boldsymbol{V}\boldsymbol{G}_0 + \boldsymbol{G}_0\boldsymbol{V}\boldsymbol{G}_0\boldsymbol{V}\boldsymbol{G}_0 + \boldsymbol{G}_0\boldsymbol{V}\boldsymbol{G}_0\boldsymbol{V}\boldsymbol{G}_0\boldsymbol{V}\boldsymbol{G}_0 + \dots \tag{1.1}$$

Consider the 2D Green's function as a superposition of weighted plane-wave solution, by multiplying a weighted factor $\mathrm{i}2\nu_s$ with both sides of equation 1.1, the scattered wavefield of an incident plane wave is delineated as

$$\boldsymbol{b}_1 = \boldsymbol{\phi} - \boldsymbol{\phi}_0 = \boldsymbol{G}_0\boldsymbol{V}\boldsymbol{\phi}_0 + \boldsymbol{G}_0\boldsymbol{V}\boldsymbol{G}_0\boldsymbol{V}\boldsymbol{\phi}_0 + \boldsymbol{G}_0\boldsymbol{V}\boldsymbol{G}_0\boldsymbol{V}\boldsymbol{G}_0\boldsymbol{V}\boldsymbol{\phi}_0 + \dots \tag{1.2}$$

where

$$\phi_0(x_g, z_g, k_s, z_s, \omega) = \mathrm{i}2\nu_s G_0(x_g, z_g, k_s, z_s, \omega) \tag{1.3}$$

with $\boldsymbol{b}_1 = \mathrm{i}2\nu_s(\boldsymbol{G} - \boldsymbol{G}_0) = \mathrm{i}2\nu_s\boldsymbol{D}$ is the weighted scattered wavefield of point sources, and $\boldsymbol{D}(z_g, z_s, \omega)$ is the measured data on surface without direct waves.

Split the perturbation operator into series by orders,

$$\boldsymbol{V} = \boldsymbol{V}_1 + \boldsymbol{V}_2 + \boldsymbol{V}_3 + \dots \tag{1.4}$$

Substitute this change into scattering wavefield representation equation (1.2), equate like orders, we have,

$$\boldsymbol{b}_1 = \boldsymbol{G}_0\boldsymbol{V}_1\boldsymbol{\phi}_0, \tag{1.5a}$$

$$\boldsymbol{0} = \boldsymbol{G}_0\boldsymbol{V}_2\boldsymbol{\phi}_0 + \boldsymbol{G}_0\boldsymbol{V}_1\boldsymbol{G}_0\boldsymbol{V}_1\boldsymbol{\phi}_0, \tag{1.5b}$$

$$\boldsymbol{0} = \boldsymbol{G}_0\boldsymbol{V}_3\boldsymbol{\phi}_0 + \boldsymbol{G}_0\boldsymbol{V}_2\boldsymbol{G}_0\boldsymbol{V}_1\boldsymbol{\phi}_0 + \boldsymbol{G}_0\boldsymbol{V}_1\boldsymbol{G}_0\boldsymbol{V}_2\boldsymbol{\phi}_0 + \boldsymbol{G}_0\boldsymbol{V}_1\boldsymbol{G}_0\boldsymbol{V}_1\boldsymbol{G}_0\boldsymbol{V}_1\boldsymbol{\phi}_0, \tag{1.5c}$$

$$\vdots$$

By solving those series reversion, the certain order of scattering potential term can be obtained in terms of weighted measured data $\boldsymbol{b}_1(z_g, z_s, t)$. The 1st-order internal multiple needs to be generated by at least 3 perturbations satisfying lower-higher-lower relationship

in pseudo-depth (referred to as the depth in the reference medium). By analyzing 3rd order in inverse scattering series (equation (1.5c)), we have,

$$\begin{aligned} \boldsymbol{G}_0\boldsymbol{V}_3\boldsymbol{\phi}_0 &= -(\boldsymbol{G}_0\boldsymbol{V}_2\boldsymbol{G}_0\boldsymbol{V}_1\boldsymbol{\phi}_0 + \boldsymbol{G}_0\boldsymbol{V}_1\boldsymbol{G}_0\boldsymbol{V}_2\boldsymbol{\phi}_0 + \boldsymbol{G}_0\boldsymbol{V}_1\boldsymbol{G}_0\boldsymbol{V}_1\boldsymbol{G}_0\boldsymbol{V}_1\boldsymbol{\phi}_0) \\ &= \boldsymbol{G}_0\boldsymbol{V}_{31}\boldsymbol{\phi}_0 + \boldsymbol{G}_0\boldsymbol{V}_{32}\boldsymbol{\phi}_0 + \boldsymbol{G}_0\boldsymbol{V}_{33}\boldsymbol{\phi}_0 \end{aligned} \tag{1.6}$$

The first two terms in 3rd-order have no contribution to internal multiple (they only contribute to primary energy, see analysis discussed by Araújo (1994)).The 3rd term $\boldsymbol{G}_0\boldsymbol{V}_{33}\boldsymbol{\phi}_0$ represents several different wave propagations through three perturbations depending on the variant depth relations between perturbations shown in Figure 1.1.

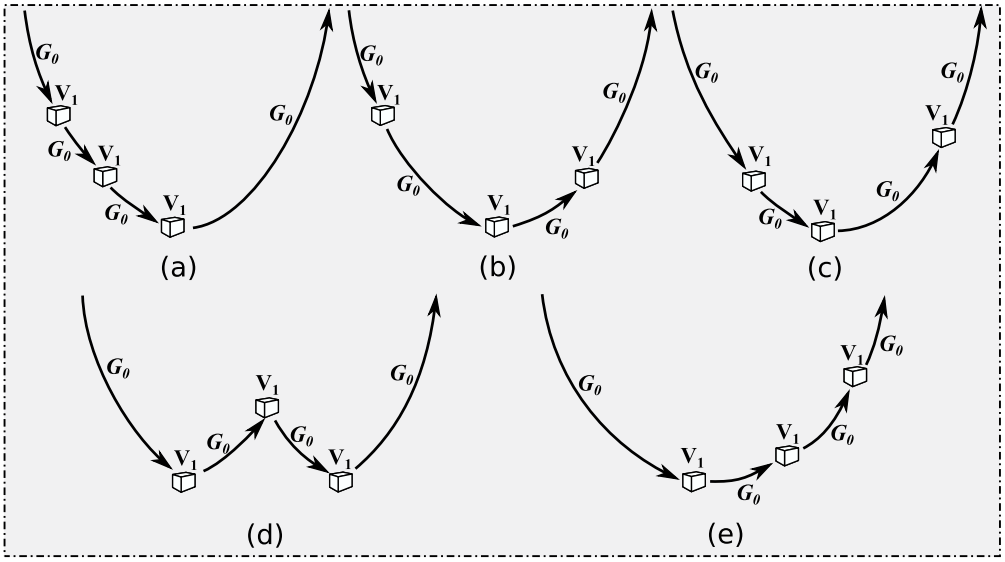

Figure 1.1: Contributions of $\boldsymbol{G}_0\boldsymbol{V}_{33}\boldsymbol{G}_0$ depending on variant depth relations between perturbations. (a) case of $z_1 < z_2 < z_3$, (b) case of $z_1 < z_3 < z_2$, (c) case of $z_3 < z_1 < z_2$, (d) case of $z2 < z_1$ and $z_2 < z_3$, (e) case of $z_3 < z_2 < z_1$.

Consider all possible wave propagations involved by $\boldsymbol{G}_0\boldsymbol{V}_{33}\boldsymbol{\phi}_0$, only one certain wave path, with perturbations satisfying lower-higher-lower relationship in pseudo-depth, has contribution to 1st-order internal multiples, shown in Figure 1.1d.

Analogously, the 2nd-order internal multiple has at least 5 perturbations, which can be contributed by $\boldsymbol{G}_0\boldsymbol{V}_1\boldsymbol{G}_0\boldsymbol{V}_1\boldsymbol{G}_0\boldsymbol{V}_1\boldsymbol{G}_0\boldsymbol{V}_1\boldsymbol{G}_0\boldsymbol{V}_1\boldsymbol{\phi}_0$ if depth of perturbations meet the needs of 'lower-higher-lower' criterion.

By solving the related terms in inverse scattering series, a data-driven internal multiple prediction algorithm can be achieved. The mathematical formula of the leading order internal multiple prediction algorithm based on inverse scattering series was demonstrated by Araújo (1994) and Weglein et al. (1997), written as,

$$\begin{aligned} b_3(k_g,k_s,\omega) = &-\frac{1}{(2\pi)^2}\iint_{-\infty}^{+\infty} \mathrm{d}k_1\mathrm{d}k_2 e^{\mathrm{i}\nu_1(z_s-z_g)} e^{\mathrm{i}\nu_2(z_g-z_s)} \int_{-\infty}^{+\infty} \mathrm{d}z_1 e^{\mathrm{i}(\nu_1+\nu_g)z_1} b_1(k_g,k_1,z_1) \\ &\times \int_{-\infty}^{z_1-\epsilon} \mathrm{d}z_2 e^{-\mathrm{i}(\nu_2+\nu_1)z_2} b_1(k_1,k_2,z_2) \int_{z_2+\epsilon}^{+\infty} \mathrm{d}z_3 e^{\mathrm{i}(\nu_s+\nu_2)z_3} b_1(k_2,k_s,z_3) \end{aligned} \tag{1.7}$$

where

$$\nu_X = \sqrt{\frac{\omega^2}{c_0^2} - k_X^2} \tag{1.8}$$

with ν_X being the vertical wavenumber associated with the lateral wavenumber k_X and a homogeneous reference velocity c_0. The integration variables z_1, z_2, and z_3 are in units of pseudo-depth, which is two-way vertical travel time scaled by the reference velocity; the pseudo-depth integration limits impose the lower-higher-lower condition. The relationships of k_g, k_1, k_2, k_s are delineated in Figure 1.2. The input b_1 is a transformed and weighted version of the measured scattering data set: $b_1(k_g,k_s,z) = -\mathrm{i}2\nu_s D(k_g,k_s,z)$, where $D(k_g,k_s,z)$ can be obtained using Stolt migration with a constant background velocity. The left hand side of equation 1.7, i.e., b_{IM}, which is a prediction of the internal multiples in D, is, next, inverse Fourier transformed over all three Fourier variables. The result, now in the (x_g,x_s,t) domain, is added to the original seismic record to attenuate the multiples. Mismatches between the prediction and the data are managed through adaptive subtraction (Abma and Kabir, 2006).

1.4 Statement of the problem

However, challenges remain in the application of these methods, particularly for land data. Luo et al. (2011) list many of the key problematic features encountered on land data, primarily noise, statics, and coupling, each of which cause trouble for multiple prediction algorithms, including those based on the inverse scattering series. Research is therefore active to address

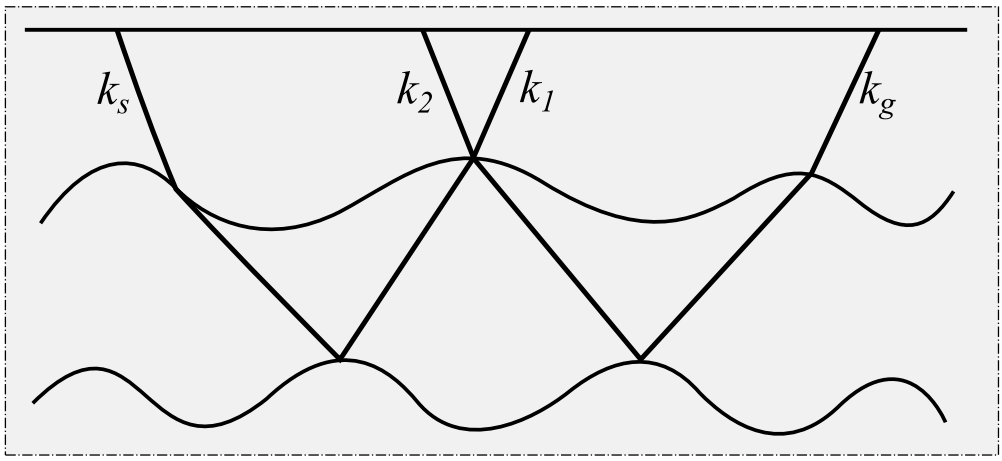

Figure 1.2: Wavenumber relations in sub-events combination of generating internal multiples

the theoretical and practical difficulties still faced by this algorithm. Herrera and Weglein (2013a); Zou and Weglein (2013) proposed a reformulated version of the algorithm that predicts the exact amplitudes of the first-order internal multiples rather than the approximate one, which was first discussed by Ramirez and Weglein (2005). To that list we would also add the increased difficulty of selecting algorithm parameters that avoid the generation of artifacts. The search parameter ϵ (Coates et al., 1996), which limits the proximity of events combined to predict multiples, is normally a single number that is selected in an ad hoc fashion, often guided by the dominant frequency of the experiment. However, wide distributions of shallow generators and generators near zones of interest can make it very difficult to fix on a suitable single value for ϵ. The use of unsuitable values can be very damaging: if chosen too large, multiples will fail to be predicted; if chosen to small, artifacts correlated with primaries appear in the prediction panel. To summarize, implementation domains, search optimum parameter selection, and expensive computational expense are major challenges of implementing inverse scattering series internal multiple prediction algorithm, which are a few objectives to be solved in this thesis.

These approaches, though powerful, are based on the acoustic approximation, and so inverse scattering series prediction technology, as it is normally implemented, is inconsistent with multi-component acquisition in onshore and ocean-bottom environments. For the

data-driven inverse scattering-based approach, wave-mode conversions in multi-component seismic records will impact the wavenumber/slowness-dependent relationships employed in the acoustic algorithm. Matson and Weglein (1996); Matson (1997) presented a 2D version of the elastic inverse scattering series prediction algorithm in wavenumber-pseudo-depth domain incorporating multicomponent data and wave-mode conversions. However, no numerical analysis or examples of the algorithm applied to a seismic gather currently appear in the literature. Unlike acoustic cases, the linear pre-processing of seismic data to achieve the input for the prediction algorithm failed to hold the monotonicity condition between pseudo-depth and actual depth. Undesired inputs would mislead the lower-higher-lower relationship and deteriorates the predicted results.

1.5 Outline

In this thesis I summarize the formulation and analysis of several techniques based on inverse series multiple prediction to address the problems listed above, and describe the algorithm design, computer implementations, and data pre-processing workflows I have developed for them. The organization of the thesis is as follows.

In Chapter 2, I briefly review inverse scattering series internal multiple prediction algorithm in original domain, i.e., wavenumber/pseudo-depth related domain. To investigate the ability of such an algorithm and observe the problems during its implementation, a three-layer geological model was created to generate a synthetic shot gathers and then examine its application on internal multiple prediction. Predicted results indicated that an inverse scattering series attenuation algorithm can predict internal multiples caused by unknown (or imperfectly known) generators in an unknown media. However, transform and aperture related artifacts were also generated in prediction. Based on this, I point out the non-compaction of the wavenumber/pseudo-depth domain prediction algorithm which increases difficulties of search parameter selection and leads to a non-stationary ϵ implementation.

Beyond that, multidimensional implementation of inverse scattering series internal multiple prediction significantly suffers from the exponential increasing computational burden because of the "spread" distribution characteristics of (k, z) domain input. Motivated by this, one of the objectives in this thesis is to seek an optimized prediction algorithm, which preserves the data-driven properties, allows a relative stationary search parameter, and reduces computational costs.

In Chapter 3, by taking advantage of the close relationships between wavenumber and horizontal-slowness, I reformulate the prediction algorithm in slowness/pseudo-depth domain. Furthermore, considering the monotonic relationship between pseudo-depth and vertical traveltime, the coupled plane-wave domain prediction formulation can also be achieved, which was first introduced by Coates et al. (1996). I present an implementation of the internal multiple prediction in the coupled plane-wave domain, which requires a tailoring of the prediction algorithm and a high fidelity τ-p_g-p_s transform. Predictions absent of almost all transform/aperture related artifacts were achieved by implementing the prediction in horizontal-slowness coherent domains. Comparing prediction inputs derived for a range of calculation domains, I conclude that the horizontal slowness domain, by concentrating the amplitudes of each sub-event, which in turn leads to a simpler and more stationary search-parameter selection, is generally optimal since models of predictability are generally plane wave models. The plane-wave domain algorithm leads to relatively stationary optimum ϵ values, and produces fewer artifacts traceable to poor parameter selection. The plane-wave domain inverse scattering series predictions appear to be well-suited to the problem of cleanly separating primary and multiple events in a waveform consistent manner. Additionally, the horizontal-slowness related input appears as a highly sparse matrix which significantly reduces its computational expense.

In Chapter 4, I propose a modified version of inverse scattering series internal multiple prediction algorithm which adapts to common-midpoint gathers. Comparing to seismic data

in source-receiver coordinates, a taper window is allowed during the CMP domain input preparation to reduce the artifacts, caused by limited apertures, because of their symmetry. Furthermore, the numerical analysis of implementing 1.5D prediction algorithm on dipping strata indicates that the CMP domain prediction algorithm is much more independent of dipping angles of generators, rather than the shot/receiver related coordinates domains. The synthetic benchmark examples show that, for small dip-angle strata, internal multiples can be predicted using 1.5D prediction algorithm with acceptable errors.

In Chapter 5, the elastic internal multiple prediction algorithm based on inverse scattering series is extended from 2D to 3D theoretically, by considering an isotropic-elastic-homogeneous reference medium. However, the prediction algorithm requires the input sorted into monotonic function of actual depth, which remains to be a big challenge because of the complexity and multiple wave-mode conversions. To achieve such an input for multicomponent internal multiple prediction, I propose several possible approaches for input preparation, such as prestack elastic Stolt migration, vertical traveltime stretching method, and incorporation of best-fit reference velocities. Their effectiveness and search optimum parameter dependencies are analyzed quantitatively with numerical simulation. Several conclusions are obtained and examined with synthetic benchmark examples. These implementations of inverse scattering series internal multiple prediction is the first time to be presented on multicomponent data.

In Chapter 6, I summarize the results obtained by the schemes and workflow proposed in this thesis. Plans for further studies are also given at the end.

Chapter 2

Inverse scattering series internal multiple prediction: Review and discussion

2.1 Introduction

Multiple attenuation and identification remains an indispensable procedure in seismic data processing and its quality will directly affect the accuracy of quantitative interpretation. Multiples are categorized into two major classes, surface-related multiples and interbed multiples. Due to their periodicity and relatively straightforward predictability, surface-related multiples can be eliminated using one of many innovative technologies, involving computations in different domains. Examples include predictive deconvolution (Taner, 1980), feedback models (Verschuur, 1991), embedding techniques (Liu et al., 2000), and inverse data processing (Berkhout and Verschuur, 2005; Berkhout, 2006; Ma et al., 2009). However, the attenuation of interbed, or internal multiples, remains a serious challenge, especially on land data, even though much considerable progresses have been made recently.

Kelamis et al. (2002) introduced a boundary-related/layer-related approach to remove internal multiples in post-stack data (CMP domain). Berkhout and Verschuur (2005) extended the inverse data processing to attenuate internal multiples by considering them as notional surface-related multiples through the boundary-related/layer-related approach in common-focus-point (CFP) domain. The same algorithm was applied by Luo et al. (2007) through re-datuming the top of the multiple generators and transforming internal multiples such that they became 'surface-related'. The common ground of those algorithms is that, as it were, extensive knowledge of subsurface is required; thus if the possibility exists that multiple removal will have to take place with incomplete knowledge of the velocity structure

and generators, the inverse scattering series approach will be optimal.

By analyzing the behaviour of the Born series in its construction of the events of a surface reflection seismic data set, Araújo (1994) and Weglein et al. (1997, 2003) demonstrated that all possible internal multiples can be estimated through the correct combination of primary and/or lower order multiple events, in an automatic way, with generating horizons and/or events sought in the data, rather than provided a priori. The processing is carried out, in short, without any subsurface information required. Recently, research has been particularly active in (1) reformulating the prediction so that its amplitudes are exact rather than approximate (Zou and Weglein, 2013), and (2) applying the existing ISS algorithm in complex environments, such as land (e.g., de Melo et al., 2014). In practical implementation, the search parameter has been focused on as a key element (Hernandez and Innanen, 2014; Innanen and Pan, 2015; Pan, 2015); in certain domains the non-stationarity of the optimum parameter choice can be a source of artifacts. In this chapter, we will review inverse scattering series internal multiple prediction both in theoretical and practical ways and investigate current major problems of implementing inverse scattering series prediction algorithm.

2.2 Internal multiple prediction algorithm in wavenumber-pseudodepth domain

2.2.1 Prediction algorithm in dipping layer cases

Weglein et al. (2003) asserts that all processing objectives of surface seismic data may be achieved directly from the data and source wavelet, using the inverse scattering series, without any subsurface information provided as input. Internal multiple removal is one of these objectives. The inverse scattering series internal multiple prediction algorithm was first introduced by Araújo (1994) and Weglein et al. (1997). It predicts the traveltimes and approximate amplitudes of all possible internal multiples by combining triplets of events satisfying an ordering relationship in pseudo-depth referred to as the *lower-higher-lower cri-*

terion. Here, the pseudo-depth is a monotonic function of actual depth (to be discussed in detail below). The algorithm as originally derived in the wavenumber-pseudo depth domain, is

$$b_{IM}(k_g,k_s,\omega) = -\frac{1}{(2\pi)^2}\iint_{-\infty}^{+\infty} \mathrm{d}k_1\mathrm{d}k_2 e^{\mathrm{i}\nu_1(z_s-z_g)} e^{\mathrm{i}\nu_2(z_g-z_s)} \int_{-\infty}^{+\infty} \mathrm{d}z_1 e^{\mathrm{i}(\nu_1+\nu_g)z_1} b_1(k_g,k_1,z_1) \\ \times \int_{-\infty}^{z_1-\epsilon} \mathrm{d}z_2 e^{-\mathrm{i}(\nu_2+\nu_1)z_2} b_1(k_1,k_2,z_2) \int_{z_2+\epsilon}^{+\infty} \mathrm{d}z_3 e^{\mathrm{i}(\nu_s+\nu_2)z_3} b_1(k_2,k_s,z_3), \tag{2.1}$$

where

$$\nu_X = \sqrt{\frac{\omega^2}{c_0^2} - k_X^2}$$

with ν_X being the vertical wavenumber associated with the lateral wavenumber k_X and a homogeneous reference velocity c_0. The integration variables z_1, z_2, and z_3 are in units of pseudo-depth, which is two-way vertical travel time scaled by the reference velocity; the pseudo-depth integration limits impose the lower-higher-lower condition. The relationships of k_g, k_1, k_2, k_s are delineated in Figure 1.2. The input b_1 is a transformed and weighted version of the measured scattering data set: $b_1(k_g,k_s,z) = -\mathrm{i}2\nu_s D(k_g,k_s,z)$, where $D(k_g,k_s,z)$ can be obtained using Stolt migration with a constant background velocity. The left hand side of equation 2.1, i.e., b_{IM}, which is a prediction of the internal multiples in D, is, next, inverse Fourier transformed over all three Fourier variables. The result, now in the (x_g,x_s,t) domain, is added to the original seismic record to attenuate the multiples. Mismatches between the prediction and the data are managed through adaptive subtraction (Abma and Kabir, 2006).

2.2.2 Prediction algorithm in layered media

Equation 2.1 indicated the combined subevents in prediction algorithm are coherent through their horizontal wavenumber components of source and receiver sides. Therefore, for layered cases, the prediction algorithm may be simplified because of an equal horizontal wavenumber at source and receiver coordinates, i.e., $k_g = k_1 = k_2 = k_s$. Using the characteristics of horizontal wavenumber components in layered cases and assuming all sources and receivers

are located at the same depth ($z_g = z_s$), equation 2.1 can be rewritten as

$$b_3(k_g,\omega) = \frac{-1}{(2\pi)^2}\int_{-\infty}^{+\infty} \mathrm{d}z_1 e^{\mathrm{i}k_z z_1} b_1(k_g, z_1) \int_{-\infty}^{z_1-\epsilon_1} \mathrm{d}z_2 e^{-\mathrm{i}k_z z_2} b_1(k_g, z_2) \int_{z_2+\epsilon_2}^{+\infty} \mathrm{d}z_3 e^{\mathrm{i}k_z z_3} b_1(k_g, z_3) \tag{2.2}$$

where, $k_z = \nu_g + \nu_s$, represents the summation of vertical wavenumbers at source and receiver sides. The horizontal component of wavenumber, here, is related to varying offsets. The epsilon ϵ is indicated as searching parameter which is a key for identifying lower-higher-lower relationship and separating subevents. Equation 2.2 demonstrated that, for layered media, internal multiples of a shot gather can be predicted by itself using inverse scattering series prediction algorithm. Beyond that, compared to 2D prediction algorithm (equation 2.1), the implementation of equation 2.2 significantly reduces memory and computational cost since is simply repeated trace-by-trace at the same k_g.

2.3 A simple numerical example

To set out some of the issues and challenges associated with the practical computation of the inverse series multiple predictions, in this section, a synthetic example based on a three-layer acoustic model is illustrated.

The geological model with velocity varying in depth only was illustrated in Figure 2.1. The source was located at the middle of geological model at a depth of 20m, and all receivers are located at surface with an interval of 20m. Four absorbing boundaries were applied for shot gather collection. Therefore, free-surface multiples were suppressed, i.e., only primaries and internal multiples were included in shot gathers. Figure 2.2 shows a generated shot gather with two primary events labeled in yellow (shown in Figure 2.2a) and two internal multiples indicated in red at zero-offset traveltime (shown in Figure 2.2b).

The input data of implementing prediction algorithm was achieved by Fourier transformation of original shot gathers over offset and travel time and then multiplied by a weighting

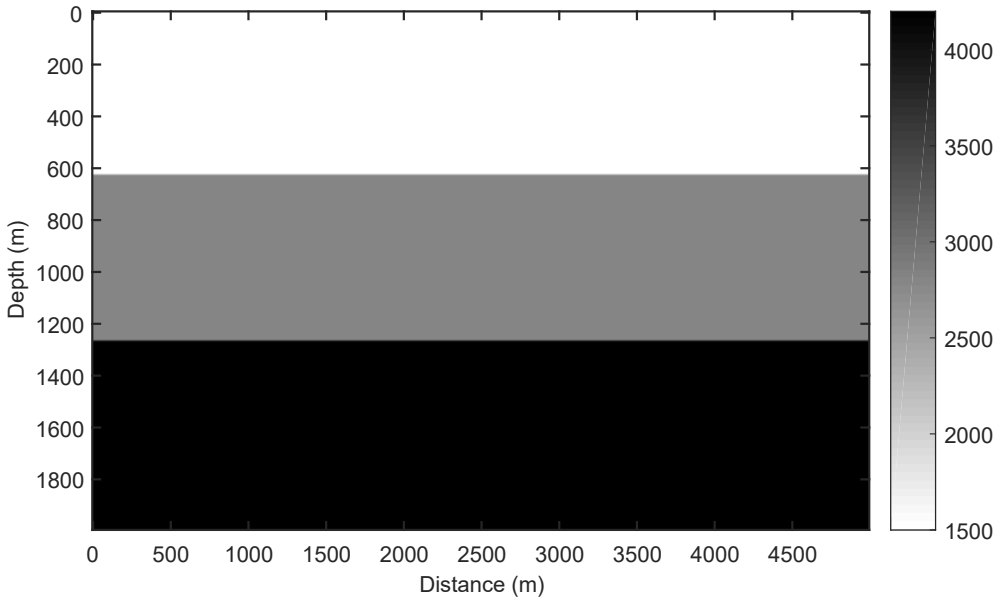

Figure 2.1: A geological model with constant density. Velocities vary from top to bottom: 1500m/s, 2800m/s, and 4200m/s.

factor. In Figure 2.3, to reduce the computational cost, we only generated the input data at the positive horizontal wavenumber k_g range. The comparison of the zero-offset trace and the stacked input trace were delineated in Figure 2.4. The lower-higher-lower criterion was not only imposed by z_1, z_2, and z_3 in equation 2.2, but also the epsilon ϵ value because of the wavelet influence. The epsilon ϵ in equation 2.2 is to separate variant subevents and to prevent aliasing generated by one single subevent, which is usually selected as the width of wavelet. However, Figure 2.3 indicated the input data in wavenumber-pseudodepth domain was spread out with increasing horizontal wavenumber. Therefore, compared to the width of wavelet, a relative larger constant value (here, $\epsilon = 337m$) is required.

The predicted internal multiples using wavenumber-pseudodepth domain inverse scattering series prediction algorithm was illustrated in Figure 2.5b. It is apparent that all internal multiples were well predicted at correct travel times, but, with waveform distortion which may be resolved by performing deconvolution before prediction. The predicted result demonstrated that inverse scattering series algorithm is able to predict all possible internal multiples with no subsurface information required and may be the promising way

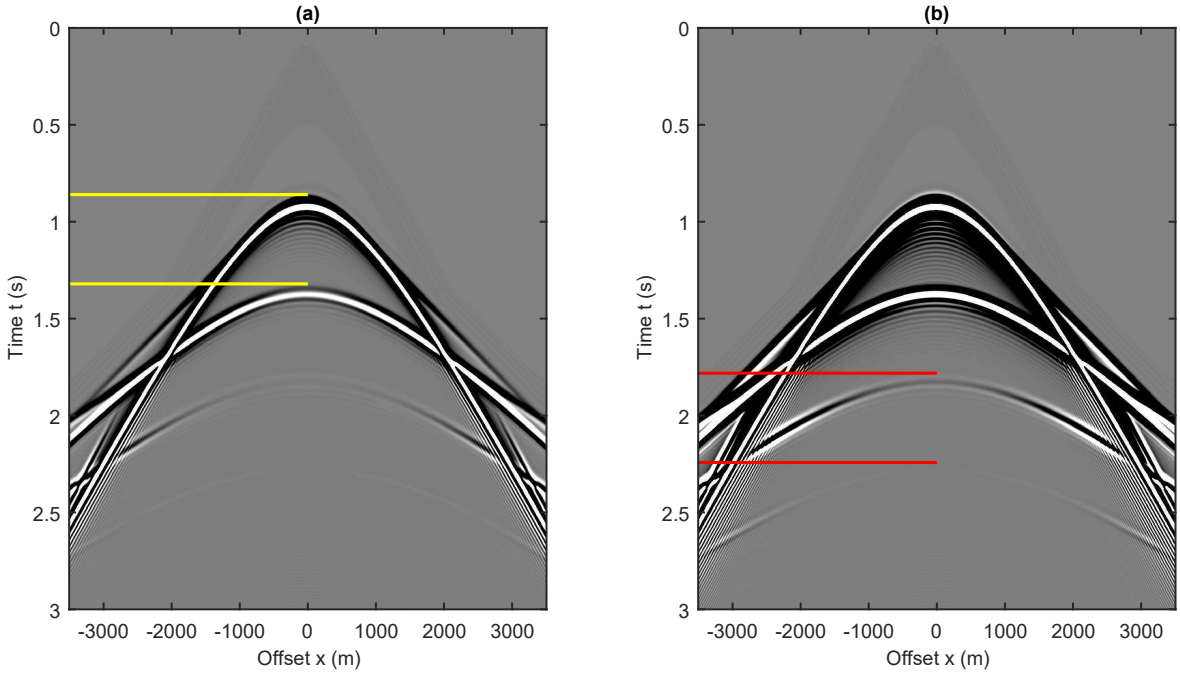

Figure 2.2: Synthetic shot gather created using model in Figure 2.1. (a) Two primary events marked in yellow; (b) 1st and 2nd order internal multiples marked in red.

to eliminate multiples in complex cases, such as land data.

2.4 Search parameter selection

The difficulties of successfully implementing inverse scattering series internal multiple prediction algorithm arise on land data due to its unique complex features such as noise, poor coupling, and thin bedding (Luo et al., 2011; Wu et al., 2011; de Melo et al., 2014). One key challenge in land inverse scattering series internal multiple prediction derives from the combination of sub-events of finite duration in time or pseudo-depth (Weglein et al., 1997). A key ingredient of separation of sub-events in pseudo-depth is the search parameter ϵ (e.g., Hernandez and Innanen, 2014), whose importance was first mentioned by Coates et al. (1996). The parameter ϵ limits the proximity of events combined to predict multiples. It is normally a single scalar number that is selected in an ad hoc fashion, often guided by the dominant frequency of the experiment. However, wide distributions of shallow generators and gener-

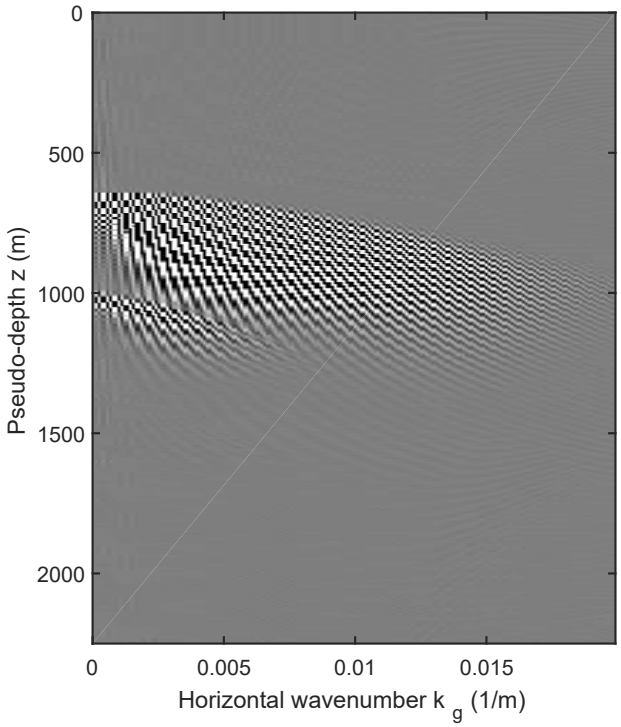

Figure 2.3: Input data for the inverse scattering series prediction algorithm; positive horizontal wavenumbers shown.

ators near zones of interest can make it very difficult to fix on a suitable single value for ϵ. The use of unsuitable values can be very damaging: if chosen too large, multiples will fail to be predicted; if chosen too small, artifacts correlated with primaries appear in the prediction panel.

A further complication is that what constitutes too large and too small may depend on what parts of the data are being considered. Figure 2.3 illustrates the fact that combinations of sub-events can become complex with increasing lateral wavenumber. Therefore, for wavenumber-pseudodepth domain prediction algorithm, a fixed search parameter is not capable of separating subevents perfectly at arbitrary wavenumber. Beyond that, implementing the internal multiple prediction using a fixed search parameter in wavenumber-pseudodepth domain may lead to large dip artifacts occurred in predicted results, especially at far offsets (Innanen and Pan, 2015). For example, we create a synthetic shot gather with far offsets using the model shown in Figure 2.1. A same search parameter $\epsilon = 337m$ was employed to

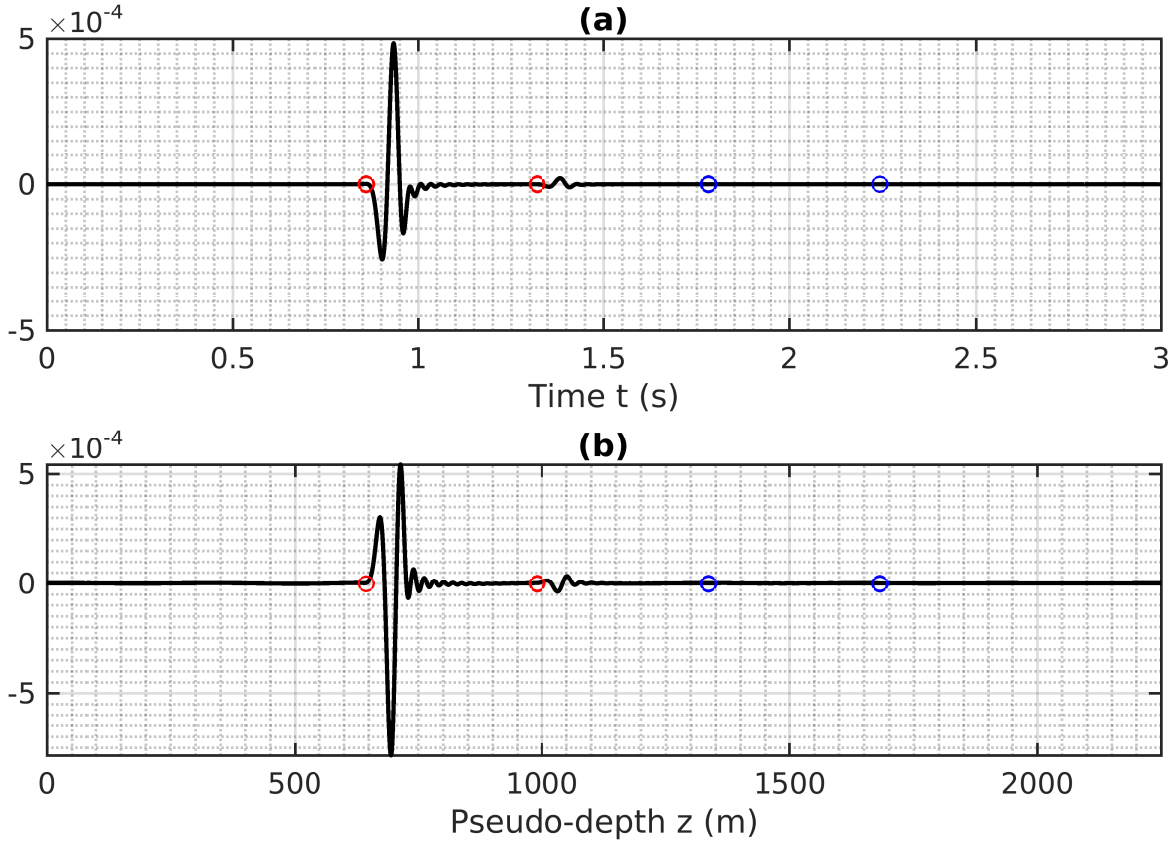

Figure 2.4: Comparison of zero-offset trace and stacked input trace. Two primaries are labelled with red circles; two internal multiples are labelled with blue circles. (a) The zero-offset trace extracted from original shot gather. (b) The input trace obtained by stacking over horizontal wavenumber.

implement internal multiple prediction in wavenumber-pseudodepth domain.

In Figure 2.6, internal multiples were successfully predicted at correct travel times, but, parts of primary events, specifically those intersecting internal multiples, are also observable in the predictions. These are called large dip artifacts, which are visible intersecting the bottom of panel at roughly -4km and 4km. Figure 2.7 shows the input for predicting internal multiples from a far-offset shot gather. At large k_g values, the sub-events are qualitatively more "spread out" in pseudo depth, and they overlap significantly. In such situations, it is impossible to find a fixed search parameter ϵ which separates the sub-events to be combined. This gives rise to the artifacts.

To solve this and enhance the precision of internal multiple prediction, two approaches

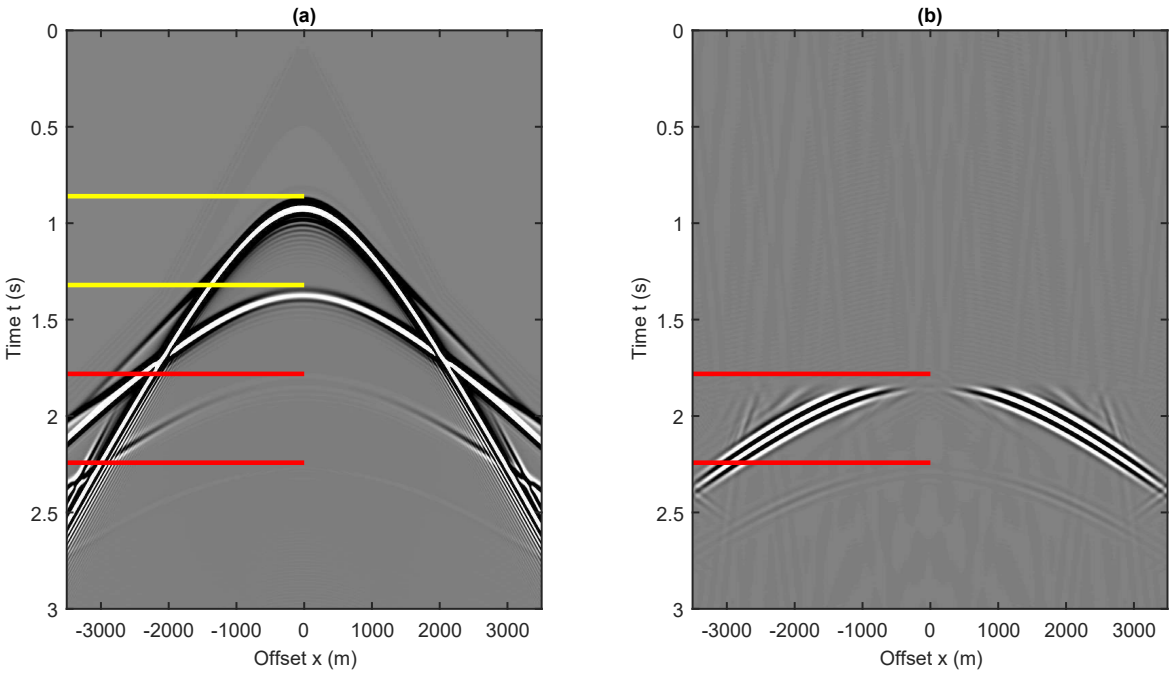

Figure 2.5: Comparison of original shot gather and internal multiple prediction. (a) The original shot gather. (b) Predicted internal multiples.

can be taken: (1) employing a non-stationary search parameter, (2) formulate the prediction algorithm in a domain in which stationarity in ϵ is appropriate. Innanen and Pan (2015) proposed variable search parameter (ϵ), as a linear function of k_g (see in Figure 2.8). However, a variable $\epsilon(k_g)$ cannot fix the problems arising from overlapping sub-events at high angle (large k_g). This observation has led me to follow the second approach in this thesis.

2.5 Conclusion

The inverse scattering series internal multiple attenuation algorithm predicts the exact traveltimes and approximate amplitudes of multiples by combining data sub-events. The lack of requirement for an accurate velocity model makes the approach extremely attractive as a means to eliminate multiples in complex environments. This could be particularly important for application on land data, but here many challenges remain. In this chapter, the essentials of the algorithm were reviewed and a numerical implementation in the wavenumber/pseudo-

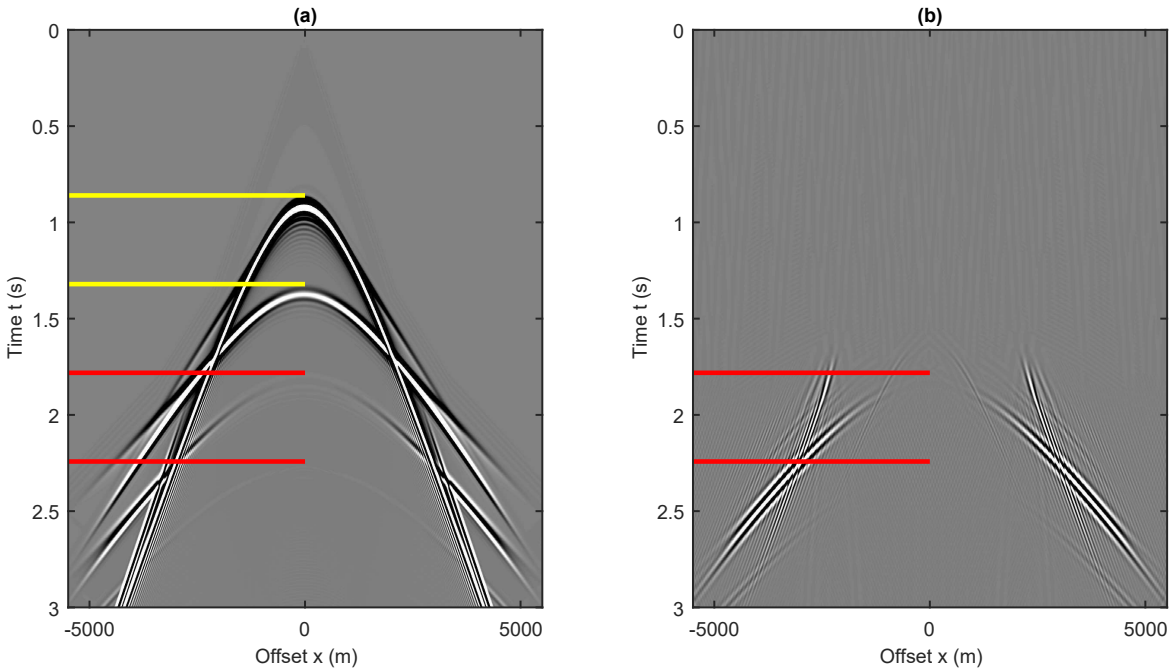

Figure 2.6: Large dip artifacts caused by a fixed search parameter ϵ in (k_g, z) domain. (a) Synthetic data from a two-interface acoustic model. (b) Prediction generated using a fixed search parameter $\epsilon = 337m$. Large dip artifacts are visible intersecting the bottom of panel at roughly -4km and 4km.

depth domain was discussed. A point central to the goals of the next chapters can then be quickly established. Internal multiples are accurately predicted at near offsets with a constant search parameter, but, large dip artifacts occurred in predicted results, especially at far offsets, because of the tendency of the input to become less sparse in pseudo-depth as the lateral wavenumber increases. This "non-compact" character of the wavenumber/pseudo-depth domain algorithm also results in higher computational costs. In coming chapters, the objective is to address the problems arising from the non-compact input through a reformulation which (1) suppresses overlap of subevents at all angles, (2) permits a relative stationary search parameter to be selected, and (3) leads to a significantly reduced computational expense.

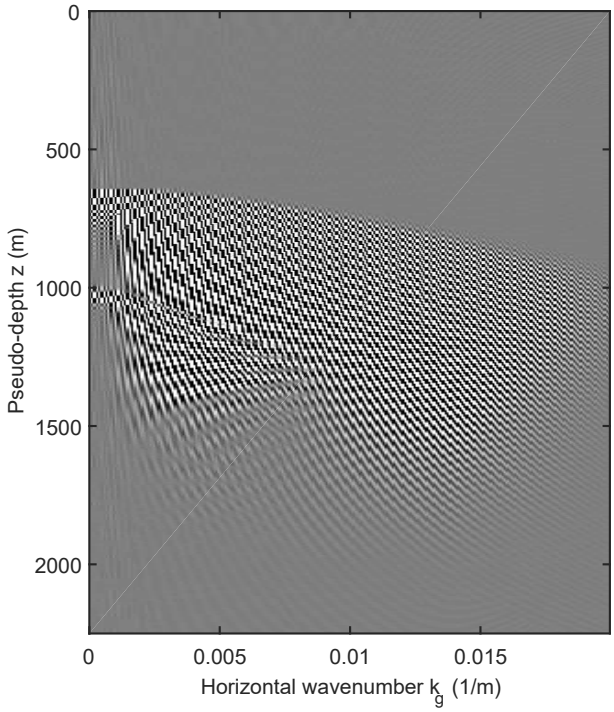

Figure 2.7: The distribution of input $b_1(k_g, z)$ at positive wavenumber obtained using far-offset data.

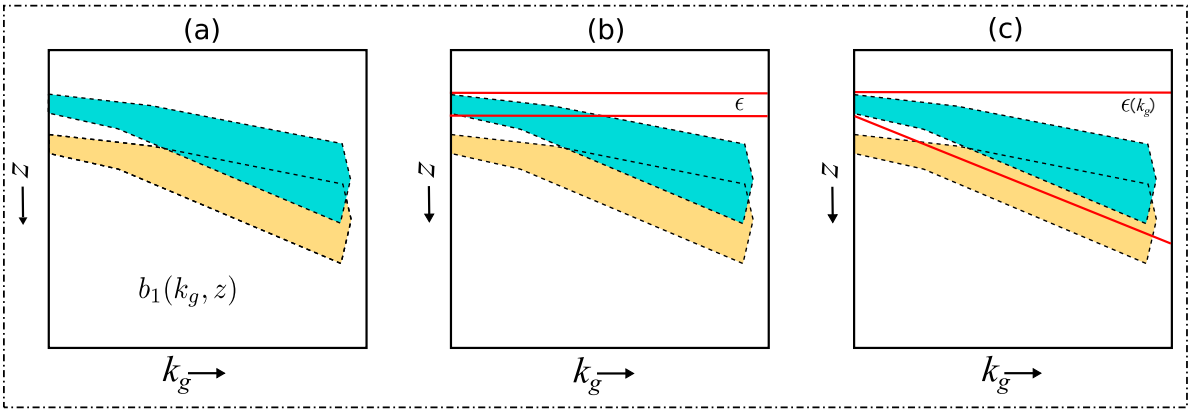

Figure 2.8: Variable search parameter in (k_g, z) domain (edited after Innanen and Pan, 2015). (a) Input $b_1(k_g, z)$; (b) search parameter ϵ fixed at a size appropriate to $k_g = 0$; (c) approximate $\epsilon(k_g)$, chosen to capture the "spread" of the sub-event.

Chapter 3

Multidimensional inverse scattering series internal multiple prediction in the coupled plane-wave domain

3.1 Summary

As I have pointed out, the inverse scattering series internal multiple prediction and attenuation algorithm predicts multiples using certain combinations of input seismic reflection data events, which are computed in the wavenumber/pseudo-depth or plane-wave/vertical travel-time (i.e., τ-p) domains. Significant differences can arise in the algorithms' output and computational expense depending on which domain is used. Many of these are traceable to the response of the algorithm to the users' choice of the search-limiting parameter ϵ. The question of which domain is optimal can be addressed with benchmark synthetics. The compactness of the input to the plane-wave domain algorithm leads to the expectation that it will have a reduced computational expense. Also, the lack of increase in the dominant period (i.e., "width") of input events as the horizontal slowness increases leads to the expectation that it will respond well to a constant ϵ. Both of these expectations are borne out with a 1.5D benchmark example. A 2D plane-wave prediction requires the data to be transformed to the τ-p_g-p_s, or coupled plane-wave, domain, involving both source-side and receiver-side horizontal slownesses. An implementation of this transform leads to the first numerical examples of full 2D inverse series τ-p prediction. The arrival times, relative amplitudes, and moveout patterns of multiples from dipping horizons are seen in a benchmark synthetic example to be faithfully determined in the plane-wave formulation; waveform mismatches are, however, observed, which are traceable to the numerics of the forward and inverse transforms. High resolution Radon transforms are a good candidate to improve the match.

3.2 Introduction

A wide range of powerful and well-characterized methods exist for predicting internal multiples (e.g., Kelamis et al., 2002; Berkhout and Verschuur, 2005; Berkhout, 2006; Luo et al., 2007; Ramirez et al., 2015; Löer et al., 2016). Of these, fully data-driven methods, in particular the internal multiple attenuation method derived from the inverse scattering series (Araújo, 1994; Weglein et al., 1997, 2003), have many of the features needed to successfully proceed in complex land environments (Luo et al., 2011)—lack of requirement for an accurate velocity model or clear move-out differences, and lack of need for known generators being important examples. Research is therefore active to address the theoretical and practical difficulties still faced by this algorithm. One of these is the approximate nature of the prediction amplitude, discussed by Ramirez and Weglein (2005) and addressed by Herrera and Weglein (2013a) and Zou and Weglein (2013). The difficulty of selecting the algorithm's internal parameter ϵ, which limits the proximity of events combined to create the prediction, when its optimum value is not constant across experimental variables (Innanen, 2017), and the computational complexity of its full multidimensional form, have also recently been examined.

The domain in which the prediction's nonlinear data operations takes place appears to have a strong influence on the seriousness of some of these issues. One of the early forms of the algorithm involves computation in the τ-p, or plane wave, domain (Coates et al., 1996). The τ-p version of the algorithm has been used to theoretically analyze its behavior (Nita and Weglein, 2009b), but to date questions about actually calculating in this domain have not been broached. It has furthermore recently been pointed out that 1D and 1.5D time- and offset-time domain versions of the algorithm, which have several useful features (Innanen, 2017), properly extend to 2D and 3D only if a plane-wave/τ-p formulation is used. Motivated by these facts, in this Chapter I present computational procedures for 1.5D and 2D internal multiple prediction in the plane-wave domain and illustrate some of its key positive

characteristics, the main one concerning the relative stationarity of optimum parameter ϵ. These results were discussed in less detailed form by (Sun and Innanen, 2015, 2016c).

The 1.5D plane-wave algorithm, appropriate for data acquired over a layered, laterally-invariant medium, requires, as input, data which have undergone a "standard" τ-p, or slant-stack, transform. These transformed data, after weighting, are combined nonlinearly in the prediction calculation. Insight into the benefits of prediction in this domain, especially relative to issues like parameter selection for land data processing (Fu et al., 2010; Wu et al., 2011; Sonika et al., 2012; Ras et al., 2012; de Melo et al., 2014, 2015), can be arrived at by inspection of this pre-processed and transformed data.

In general multidimensional media, an incoming wave component with a certain horizontal slowness scatters from a heterogeneity into outgoing waves with a wide range of slownesses. In 2D, therefore, the plane-wave domain requires independently varying source-side horizontal slownesses p_s and receiver-side slownesses p_g. Procedures for such transforms are available for seismic data processing and inversion (Diebold and Stoffa, 1981; Stoffa et al., 2006); here I base the numerical preparation of input data for internal multiple prediction on these procedures. Thereafter (1) numerical examples of 1.5D prediction allow us to exemplify the stationarity of optimal ϵ values, and (2) synthetic 2D coupled plane-wave predictions may be produced, implementations and numerical examples of which have not, to our knowledge, appeared in the literature before.

3.3 Internal multiple prediction algorithms: review

Araújo (1994) and Weglein et al. (1997) demonstrated that internal multiple predictions are obtained by summing over triplets of events whose pseudo-depths or vertical travel-times satisfy a lower-higher-lower relationship, wherein the phases of the lower (or deeper) two events are added and the phase of the higher (or shallower) event is subtracted. This process requires the knowledge of the source signature. Let $d(x_g, x_s, t)$ represent a fully deghosted 2D

seismic data set involving waves downgoing from the source and upgoing to the receiver, with x_g being the inline receiver coordinate, x_s being the inline source coordinate, and t being the two-way travel time. Let $D(k_g, k_s, \omega)$ represent the data set after Fourier transformation across all three coordinates, with k_g and k_s being the wavenumbers conjugate to x_g and x_s, respectively, and ω being the angular frequency. The standard formulation of inverse scattering series internal multiple prediction is (Araújo, 1994; Weglein et al., 1997)

$$\begin{aligned} b_{IM}(k_g, k_s, \omega) = &- \frac{1}{(2\pi)^2} \iint_{-\infty}^{+\infty} \mathrm{d}k_1 \mathrm{d}k_2 e^{\mathrm{i}\nu_1(z_s - z_g)} e^{\mathrm{i}\nu_2(z_g - z_s)} \int_{-\infty}^{+\infty} \mathrm{d}z_1 e^{\mathrm{i}(\nu_1 + \nu_g)z_1} b_1(k_g, k_1, z_1) \\ &\times \int_{-\infty}^{z_1 - \epsilon} \mathrm{d}z_2 e^{-\mathrm{i}(\nu_2 + \nu_1)z_2} b_1(k_1, k_2, z_2) \int_{z_2 + \epsilon}^{+\infty} \mathrm{d}z_3 e^{\mathrm{i}(\nu_s + \nu_2)z_3} b_1(k_2, k_s, z_3), \end{aligned} \tag{3.1}$$

where

$$\nu_X = \sqrt{\frac{\omega^2}{c_0^2} - k_X^2}$$

with ν_X being the vertical wavenumber associated with the lateral wavenumber k_X and a homogeneous reference velocity c_0. The integration variables z_1, z_2, and z_3 are in units of pseudo-depth, which is two-way vertical travel time scaled by the reference velocity; the pseudo-depth integration limits impose the lower-higher-lower condition. The input b_1 is a transformed and weighted version of the measured scattering data set: $b_1(k_g, k_s, z) = -i2\nu_s D(k_g, k_s, z)$. The left hand side of equation 3.1, i.e., b_{IM}, which is a prediction of the internal multiples in D, is, next, inverse Fourier transformed over all three Fourier variables. The result, now in the (x_g, x_s, t) domain, is added to the original seismic record to attenuate the multiples. Mismatches between the prediction and the data are managed through adaptive subtraction (e.g., Abma and Kabir, 2006; Keating et al., 2016).

3.3.1 Slowness/pseudo-depth domain

In addition to obeying the lower-higher-lower relationship, any three events combined to reconstruct the ray-path of an internal multiple (these events are called *sub-events* in the context of prediction) are also related through their wavenumber components on source and

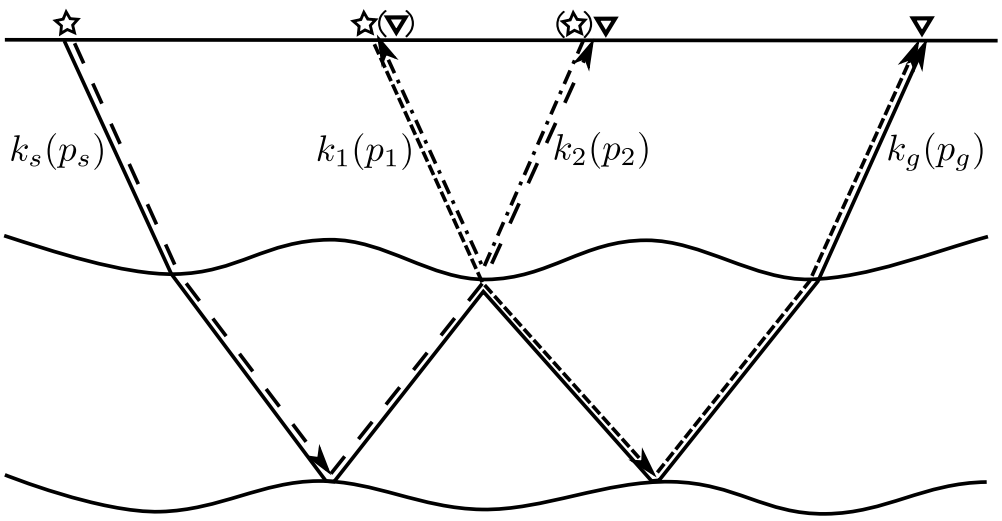

Figure 3.1: Ray-path schematic of primaries (dashed line) and internal multiple (solid line) with corresponding source and receiver locations. See also (Coates et al., 1996) and (Nita and Weglein, 2009b).

receiver sides. Figure 3.1 illustrates the ray-path relationships between primaries and predicted internal multiples, which can be labeled according to their contributing wavenumbers, i.e., k_g, k_s, k_1, and k_2 in equation 3.1.

The prediction algorithm in equation 3.1 can also be re-written in terms of slownesses by taking advantage of the close relationships between k's and p's ($k = \omega p$):

$$\begin{aligned} b_{IM}(p_g, p_s, \omega) =& \frac{-1}{(2\pi)^2} \iint_{-\infty}^{+\infty} \mathrm{d}p_1 \mathrm{d}p_2 e^{\mathrm{i}\omega q_1 (z_s - z_g)} e^{\mathrm{i}\omega q_2 (z_g - z_s)} \int_{-\infty}^{+\infty} \mathrm{d}z_1 e^{\mathrm{i}\omega (q_1 + q_g) z_1} b_1(p_g, p_1, z_1) \\ & \times \int_{-\infty}^{z_1 - \epsilon} \mathrm{d}z_2 e^{-\mathrm{i}\omega (q_2 + q_1) z_2} b_1(p_1, p_2, z_2) \int_{z_2 + \epsilon}^{+\infty} \mathrm{d}z_3 e^{\mathrm{i}\omega (q_s + q_2) z_3} b_1(p_2, p_s, z_3), \end{aligned} \tag{3.2}$$

where

$$q_X = \sqrt{\frac{1}{c_0^2} - p_X^2},$$

and where q_X is the vertical slowness associated with the horizontal slowness p_X, and the reference velocity c_0. The input b_1 is, again, a transformed and weighted version of the input data $b_1(p_g, p_s, z) = -i2q_s D(p_g, p_s, z)$, where in this case the data have been decomposed into their source and receiver side horizontal slowness components, p_s and p_g respectively, and pseudo-depth z as before.

3.3.2 Coupled plane-wave domain

Pseudo-depth z and intercept time τ are related through depth wavenumber and angular frequency (Nita and Weglein, 2009b):

$$k_z z = \omega\tau, \tag{3.3}$$

where the depth wavenumber is the sum of the vertical wavenumbers on the source and receiver sides, $k_z = \nu_g + \nu_s$. Because wavenumber and slowness are related by $k_z = \omega q$, equation 3.3 can be re-written as

$$qz = \tau, \tag{3.4}$$

where $q = q_g + q_s$ is the sum of the vertical slownesses on the source and receiver sides. Equation 3.4 makes clear (see also Nita and Weglein, 2009b) that any comparative remarks made between one pseudo-depth and another can also be made about the corresponding intercept times, i.e.,

$$z_1 > z_2 \Longleftrightarrow \tau_1 > \tau_2. \tag{3.5}$$

Substituting equation 3.4 into equation 3.2, the full plane-wave form of the prediction algorithm is obtained (Coates et al., 1996):

$$\begin{aligned} b_{IM}(p_g, p_s, \omega) =& \frac{-1}{(2\pi)^2} \iint_{-\infty}^{+\infty} \mathrm{d}p_1 \mathrm{d}p_2 e^{\mathrm{i}\omega(\tau_{1s}-\tau_{1g})} e^{\mathrm{i}\omega(\tau_{1g}-\tau_{1s})} \int_{-\infty}^{+\infty} \mathrm{d}\tau_1 e^{\mathrm{i}\omega\tau_1} b_1(p_g, p_1, \tau_1) \\ & \times \int_{-\infty}^{\tau_1-\epsilon} \mathrm{d}\tau_2 e^{-\mathrm{i}\omega\tau_2} b_1(p_1, p_2, \tau_2) \int_{\tau_2+\epsilon}^{+\infty} \mathrm{d}\tau_3 e^{\mathrm{i}\omega\tau_3} b_1(p_2, p_s, \tau_3), \end{aligned} \tag{3.6}$$

where p_g and p_s are the source and receiver horizontal slownesses respectively (these are equal in 1D and 1.5D calculations). The input is the 3D[1] volume calculated by scaling the data after double τ-p_s-p_g transformation: $b_1(p_g, p_s, \tau) = -i2q_s D(p_g, p_s, \tau)$. As with equation 3.1, the ray-path relationships between primaries and predicted internal multiples can be understood through the scheme in Figure 3.1, this time according to their contributing slownesses, i.e., p_g, p_s, p_1, and p_2 in equation 3.6. The quantities p_1 and p_2 represent horizontal slownesses at both

[1]This is a 3D data volume, not a 3D seismic acquisition being treated.

source and receiver locations within the algorithm. This will be of practical computational importance, as it requires that matching source and receiver slownesses must be available either naturally through acquisition or through data reconstruction.

3.4 Preparation of τ-p_s-p_g domain prediction inputs

Multidimensional internal multiple prediction can be implemented in the coupled plane-wave domain via equation 3.6. To do so requires that the seismic records be mapped into the plane wave-domain and weighted to create the input. Traditional τ-p mapping, also known as slant-stack, was introduced by Ocola (1972) and Diebold and Stoffa (1981) and is usually implemented by considering travel times for varying offsets and fixed source locations,

$$t = p_g x + \sum_i z_{si}(q_{si} + q_{gi}), \tag{3.7}$$

or, varying offsets and fixed receiver locations,

$$t = p_s x + \sum_i z_{gi}(q_{si} + q_{gi}), \tag{3.8}$$

where t is the travel time of the event being described, and x is the offset. The variables q_{si} and q_{gi} are the vertical components of slowness in the i^{th} layer for the source and receiver respectively. The depths z_{si} and z_{gi} are the thicknesses of the i^{th} layer below the source and receiver locations respectively. Diebold and Stoffa (1981) also introduced a reference point M, located between source and receiver (M is the midpoint in the common midpoint gather), and applied the τ-p transform based on this reference point location:

$$t = p_s x_{sM} + p_g x_{gM} + \sum_i z_{Mi}(q_{si} + q_{gi}), \tag{3.9}$$

where x_{sM} and x_{gM} are the distances between the source and geophone and the reference point respectively. The quantity z_{Mi} represents the thicknesses of the i^{th} layer below the reference point. A schematic illustration of ray-paths is given in Figure 3.2.

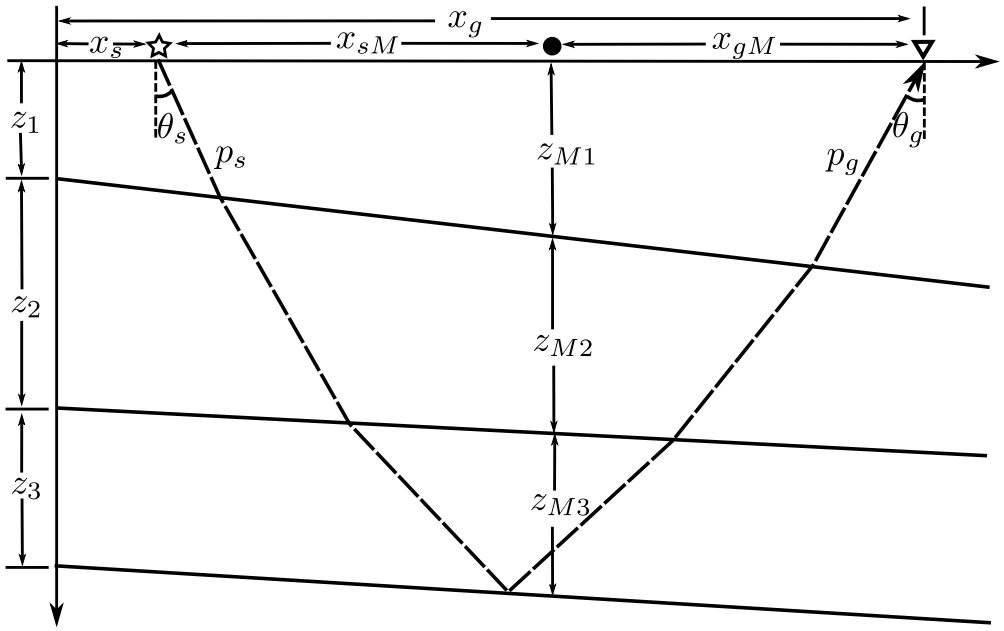

Figure 3.2: The ray-path geometry schematic of $\tau - p$ mapping with respect to the reference point, after Diebold and Stoffa (1981).

In order to make use of the Diebold-Stoffa scheme to create input for multiple prediction, an alteration is necessary to the algorithm in equation 3.6. Suppose the coordinate system is so chosen that the offset is positive (i.e., $x = x_g - x_s > 0$) when the source is on the left. From equation 3.9, I observe that the horizontal slowness has the opposite sign for the same ray-path if the source and receiver locations are exchanged, i.e., $p'_s = -p_g, p'_g = -p_s$. To account for this, I note that p_1 and p_2 in the integration over τ_2 in equation 3.6 must be multiplied by -1. The coupled τ-p_s-p_g transform is then carried out as follows. The origin $x = 0$, which is located on the one side of source and receiver, is selected as the reference point. Then

$$t = p_s x_s + p_g x_g + \sum_i z_i (q_{si} + q_{gi}), \tag{3.10}$$

where x_s and x_g are the source and receiver locations respectively, and z_i is the thickness of i^{th} layer below the origin. Equation 3.10 indicates that the coupled τ-p_s-p_g transform is a variant of the single τ-p transform, with a particular phase shift carried out over source and

receiver locations respectively (Stoffa et al., 2006). This can be expressed as

$$D(p_s, p_g, \tau) = \iint d(x_s, x_g, \tau + p_s x_s + p_g x_g) \mathrm{d}x_s \mathrm{d}x_g. \tag{3.11}$$

Alternatively, the forward double τ-p_s-p_g transform for a fixed frequency can be expressed as

$$\hat{D}(p_s, p_g, \omega) = \iint \hat{d}(x_s, x_g, \omega) e^{+\mathrm{i}\omega(p_s x_s + p_g x_g)} \mathrm{d}x_s \mathrm{d}x_g, \tag{3.12}$$

and the inverse transform as

$$\hat{d}(x_s, x_g, \omega) = \iint \hat{D}(p_s, p_g, \omega) e^{-\mathrm{i}\omega(p_s x_s + p_g x_g)} \mathrm{d}p_s \mathrm{d}p_g, \tag{3.13}$$

where as before $d(x_s, x_g, t)$ represents a 2D seismic data set with respect to source and receiver locations, and now $\hat{d}(x_s, x_g, w)$ represents the data set after Fourier transformation over time, and finally $\hat{D}(p_s, p_g, \omega)$ represents the coupled τ-p_s-p_g transformed data set for a fixed frequency. For a full 3D case, the plane wave transformation must also be carried out with respect to the second lateral dimension.

I assume a multi-shot 2D seismic data set is recorded over a three-layer model (containing a shallow dipping reflector and a deeper flat reflector), with shots occupying each receiver location (either through acquisition or regularization). Figure 3.3 illustrates the procedure used for the double τ-p_g-p_s transform using gather extracted from a synthetic data set whose details are set out in the next section. In Figure 3.3a, a common shot gather extracted from a raw data volume $d(x_g, x_s, t)$, at a particular location x_s (specifically 636m in this example), is illustrated. The data are next transformed across receiver coordinate into the horizontal slowness domain ($x_g \rightarrow p_g$), such that for the given shot point I obtain a gather in the t-p_g domain. This is illustrated in Figure 3.3b. Repeating this for all sources I create a data volume in the (t,p_g,x_s) domain, from which common p_g gathers can be extracted. In Figure 3.3c the $p_g = 0$ gather is illustrated. The complete double τ-p_g-p_s transform is finally obtained by transforming the source coordinate into horizontal slowness. A common $p_g = 0$ gather in the p_s domain is extracted and illustrated in Figure 3.3d.

One source of computational efficiency that is available to the plane-wave domain prediction formulation is already apparent at this stage. The data in the x_g-x_s and p_g-p_s domains at two fixed values of frequency (10 Hz and 20 Hz) are compared in Figure 3.4. The energy in the p_g-p_s domain is more compactly represented than it is across the x_g-x_s coordinates. Because the data are weighted and integrated in a computationally expensive manner once for each output domain coordinate, domains in which the number of nonzero input values is small are naturally more competitive. In this particular example the compactness is related to limited ranges of dips in the reflecting horizons. The slownesses and frequencies in the double plane-wave domain can be quantitatively connected with the maximum dipping angles of contributing interfaces (Liu et al., 2000). Therefore prior knowledge limiting the maximum dip of contributing interfaces can be used to shrink the number of integrations needed.

3.5 Prediction in 1.5D: compactness and stationarity

To examine the differences between predictions involving the horizontal slowness, wavenumber, pseudo-depth and/or vertical time, I take the algorithms as set out earlier and reduce them to reflect a 1.5D (point source, depth-varying medium) configuration, which I will approximate with 2D (line source/receiver) modeling. If the Earth is layered, the algorithms in the horizontal slowness/pseudo-depth and plane-wave domains, p-z and p-τ respectively, simplify to reflect the fact that $p_g = p_s = p$. If additionally all sources and receivers are at the same depth, the plane wave domain prediction algorithm in equation 3.6 reduces to

$$b_{IM}(p,\omega) = -\frac{1}{(2\pi)^2}\int_{-\infty}^{+\infty} \mathrm{d}\tau_1 e^{\mathrm{i}\omega\tau_1} b_1(p,\tau_1) \int_{-\infty}^{\tau_1-\epsilon} \mathrm{d}\tau_2 e^{-\mathrm{i}\omega\tau_2} b_1(p,\tau_2) \int_{\tau_2+\epsilon}^{+\infty} \mathrm{d}\tau_3 e^{\mathrm{i}\omega\tau_3} b_1(p,\tau_3), \tag{3.14}$$

where $p = 2p_s$ is the horizontal slowness and τ is the intercept time. As before, the input is a transformed and scaled version of the data: $b_1(p,\tau) = -i2q_sD(p,\tau)$. The transformed data $D(p,\tau)$ are in this case computed from a standard τ-p or slant-stack transformation

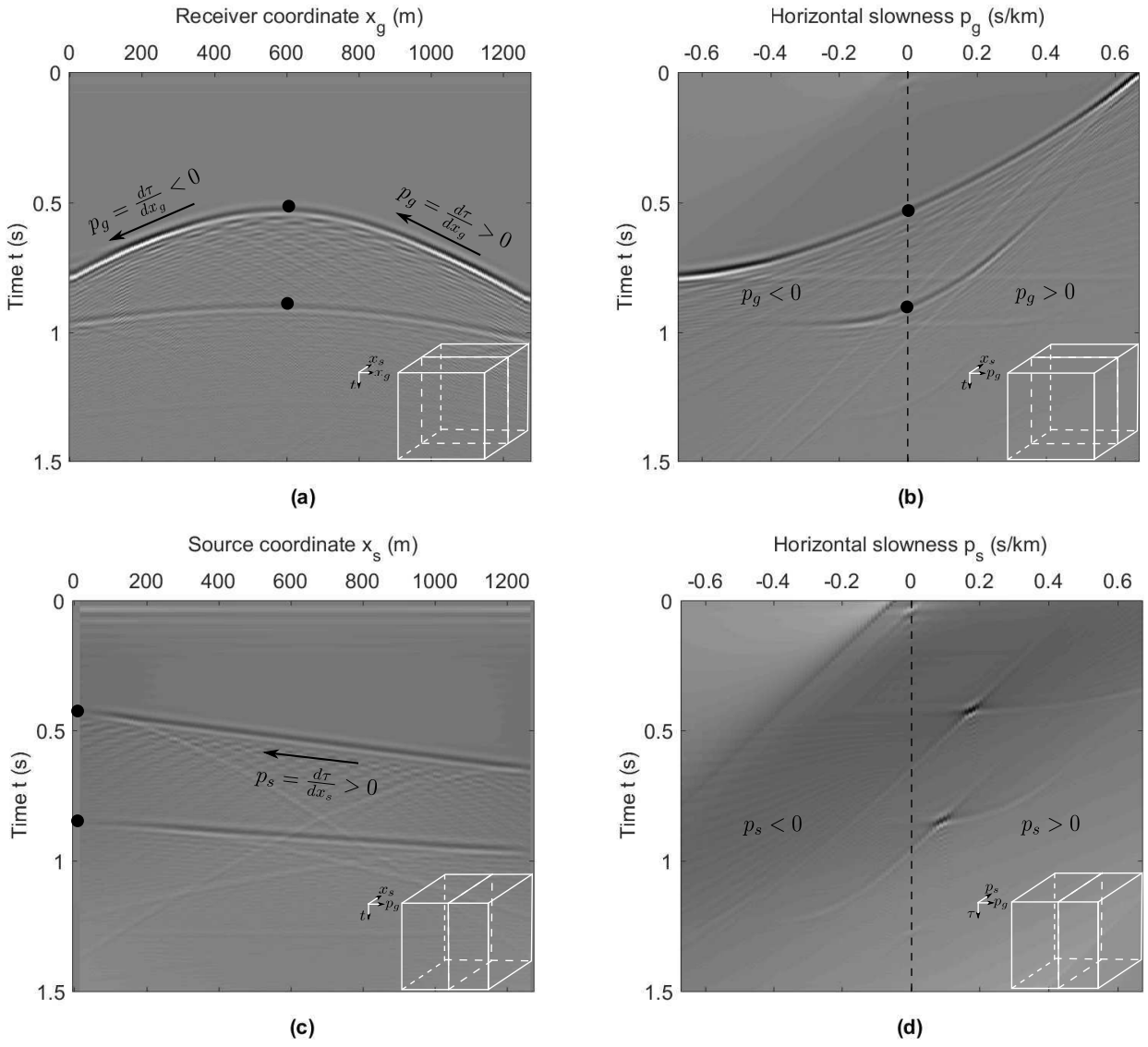

Figure 3.3: Double τ-p_g-p_s transform workflow. (a) A shot gather ($x_s = 636m$) extracted from a synthetic volume $d(t, x_g, x_s)$; (b) a common shot gather in $t - p_g$ domain obtained by transforming $x_g \rightarrow p_g$; (c) the common $p_g = 0$ gather extracted from the (t, p_g, x_s) volume; (d) the common $p_g = 0$ gather extracted from the final double τ-p_g-p_s transformed data volume.

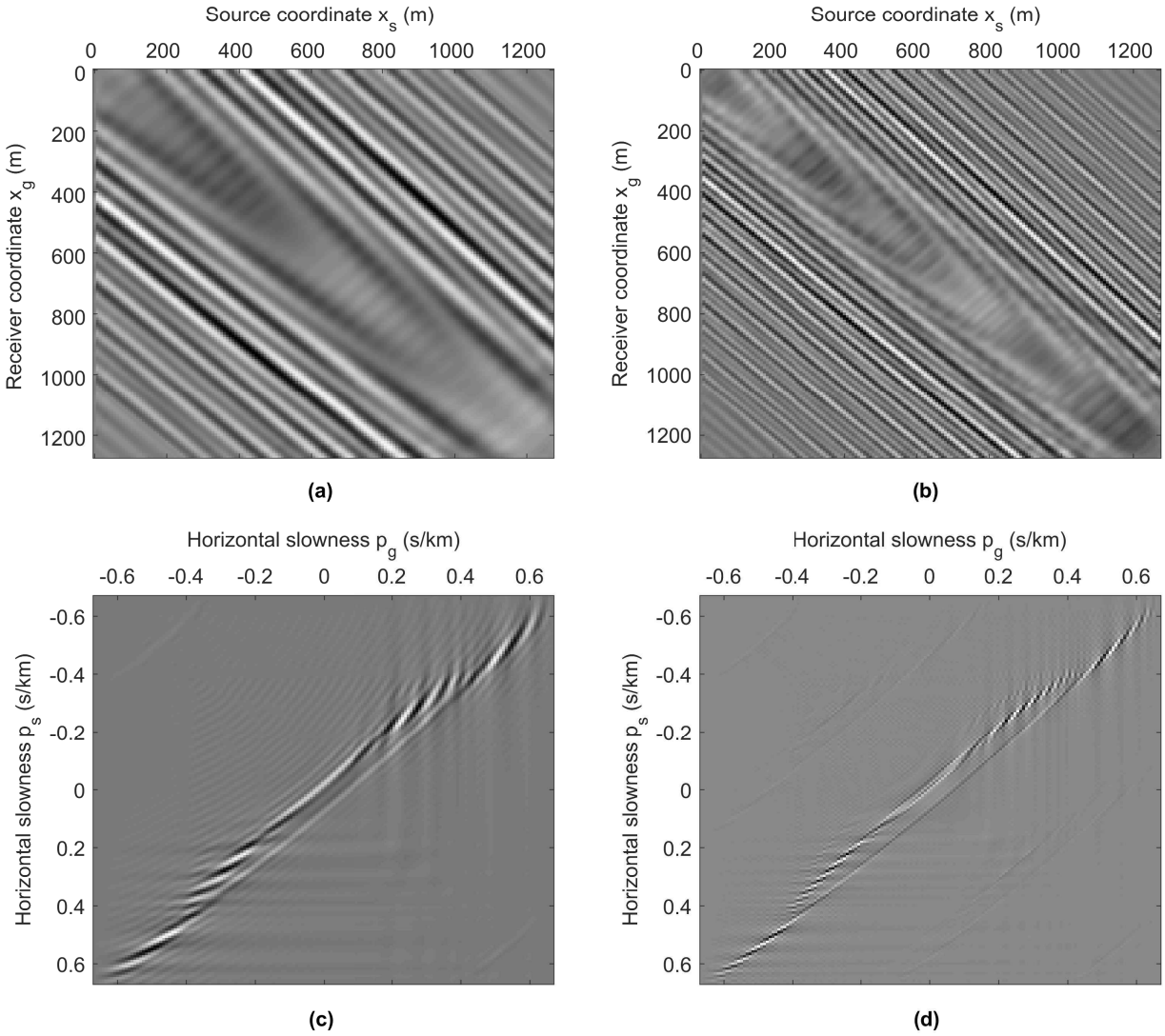

Figure 3.4: Comparison of data compactness at fixed frequencies. (a) Space domain data (x_g, x_s) at 10 Hz; (b) space domain data (x_g, x_s) at 20 Hz; (c) plane-wave domain data at 10 Hz; (d) plane-wave domain data at 20 Hz.

of a shot gather. Similarly, the internal multiple prediction algorithm in the horizontal slowness/pseudo-depth domain (equation 3.2) reduces in the 1.5D case to

$$b_{IM}(p,\omega) = \frac{-1}{(2\pi)^2}\int_{-\infty}^{+\infty} \mathrm{d}z_1 e^{\mathrm{i}\omega q z_1} b_1(p,z_1) \int_{-\infty}^{z_1-\epsilon} \mathrm{d}z_2 e^{-\mathrm{i}\omega q z_2} b_1(p,z_2) \int_{z_2+\epsilon}^{+\infty} \mathrm{d}z_3 e^{\mathrm{i}\omega q z_3} b_1(p,z_3), \tag{3.15}$$

where $q = 2q_s = \frac{2\cos\theta}{c_0}$ is the vertical slowness, and c_0 is the velocity in the reference medium. From equation 3.4, the pseudo-depth can be seen to be related to τ by $z = \frac{c_0\tau}{2\cos\theta}$. The input is $b_1(p,z) = -i2q_sD(p,z)$; computing this input is equivalent to carrying out a normal move-out correction of a shot gather in plane wave domain, using the reference velocity. The input data will therefore (deliberately) have events with different degrees of apparent over- or under-correction: in other words, sub-events with root-mean-square (RMS) velocities lower than the reference velocity would be over-corrected; sub-events with RMS velocity higher than the reference velocity would be under-corrected. This over/under-correction is a natural part of the algorithm, and does not lead to incorrect predictions. However, it does produce in the input a characteristic p-dependence which should be monitored for its effect on optimum choice of parameter ϵ (Innanen and Pan, 2015; Innanen, 2017).

A three-layer synthetic model with two flat reflectors is introduced from which to compute a synthetic shot gather, which can then be used as input to the various forms of internal multiple prediction algorithm. The model is illustrated in Figure 3.5. Density is held constant throughout, and velocities in the geological model vary from 1500m/s in the top, to 2800m/s in the middle layer, to 4200m/s in the bottom layer. Synthetic seismic data are generated from the velocity model illustrated in Figure 3.5 using a fourth-order finite difference scheme with four absorbing boundaries. A shot record with a source point at the center is shown in Figure 3.6(a). With the top of the model also absorbing, no free-surface multiples are created, only primaries and internal multiples. The analytically calculated arrival times at zero offset of the two primaries are illustrated with white solid lines, and those of the first and second orders of internal multiples are illustrated with white dashed lines. The τ-p

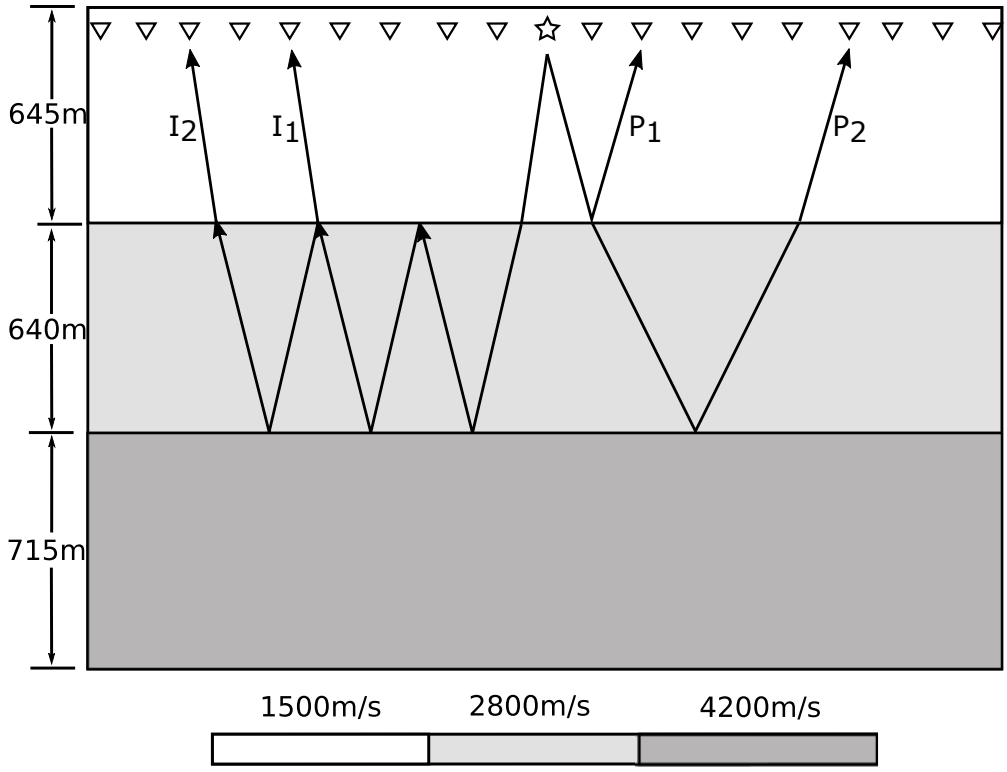

Figure 3.5: Synthetic velocity model (density is held fixed). Velocities are $1500m/s$ in the top layer, $2800m/s$ in the middle layer, and $4200m/s$ in the bottom layer.

transform of the shot gather is calculated and illustrated in Figure 3.6(b).

Properly weighted input to the prediction algorithms in both the plane wave domain and the horizontal slowness/pseudo-depth domain are obtained by multiplying the data in both the p-τ and p-z domains by the weight $-i2q_s$, as shown in Figures 3.7(a) and 3.7(b), respectively. The input $b_1(k_g, z)$ for the wavenumber/pseudo-depth domain implementation is also obtained for comparison and illustrated in Figure 3.7(c). The searching limiting parameter ϵ is key to the proper combination of data variations in the prediction of internal multiples. It is a constant in the original forms of the attenuation algorithm (i.e., equations 3.1, 3.2, and 3.6 in this Chapter). An optimal ϵ value will generate a complete prediction of multiples without introducing artifacts. If ϵ is chosen too small, artifacts correlated with primaries appear; if it is chosen too large, multiple predictions will be missed (Sun and Innanen, 2016b; Innanen, 2017). In Figure 3.7(c), the energy in each sub-event is increasingly

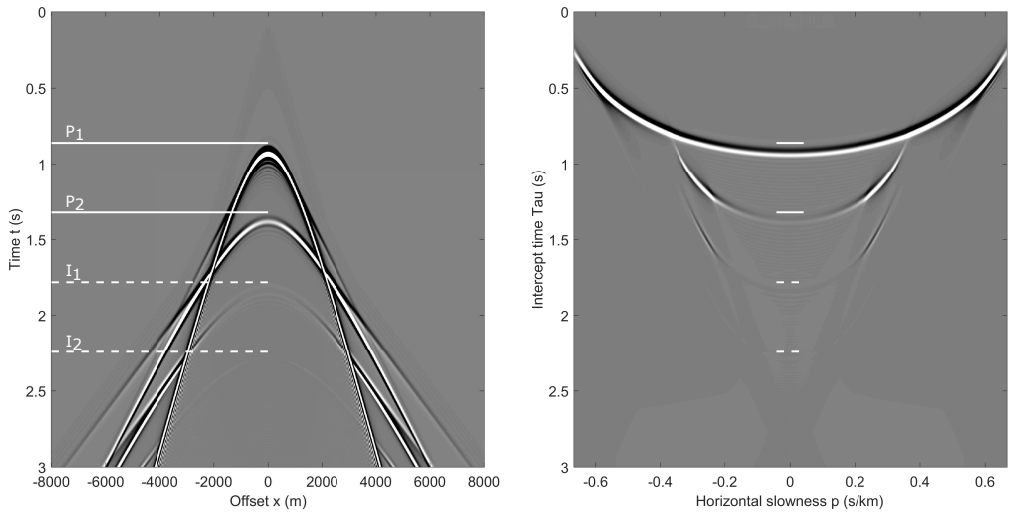

(a) (b)

Figure 3.6: Synthetic seismic data created from the velocity model illustrated in Figure 3.5: (a) the shot gather; (b) the data in the τ-p transformation of the raw data.

distributed in pseudo-depth as the wavenumber k_g increases. This means internal multiple prediction in the k_g-z domain will involve a non-stationary search parameter to separate the certain sub-events in the combination. A key positive feature of the prediction input in the plane-wave domain(s) is now visible: compared to the k_g-z domain, the inputs plotted in Figure 3.7(a) and Figure 3.7(b) exhibit compactness in the depth- and/or time-coordinate direction, and, critically, a separation between sub-events which does not vary strongly with p. These two facts together mean that an "aggressive" and nonstationary ϵ can be avoided (Innanen, 2017). The input for p-z versus the p-τ domain inputs can also be compared. In Figure 3.7(b) a greater degree of noise is evident, which is due to the effects of linear interpolation used in the change of variables.

I then select the stationary search parameter ϵ to be slightly larger than the width of one sub-event in a stacked trace, as illustrated in Figure 3.8. Here, a constant value of $\epsilon = 0.2s$ is selected for implementation in p-τ domain, and $\epsilon = 150m$ is selected for implementation in p-z domain. The same ϵ is used for the wavenumber/pseudo-depth example.

The three related predictions, computed from the raw data in Figure 3.6(a) transformed

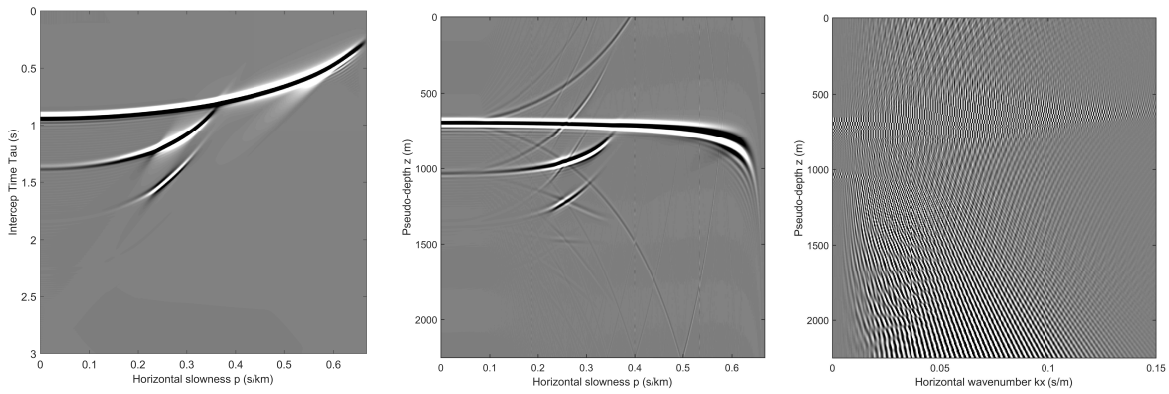

(a) (b) (c)

Figure 3.7: The three inputs to internal multiple prediction, plotted for positive p or k_g only: (a) the p-τ input for plane wave domain prediction, (b) the p-z input for horizontal slowness/pseudo-depth domain prediction, (c) the k_g-z input for wavenumber/pseudo-depth domain prediction.

into the three domains as shown in Figure 3.7, are plotted together in Figure 3.9. As expected, using a fixed search parameter in k_g-z domain prediction produces spurious high-angle artifacts into the prediction due to the spread-out energy of the input as the wavenumber increasing. Innanen and Pan (2015) propose a nonstationary ϵ to mitigate this. However, as visible in Figure 3.9(c), because of the constancy of the size of sub-events across the p spectrum, the implementations both in the p-τ and the p-z domains generate clean results despite having been computed with a single stationary ϵ value. The p-z domain prediction is noisier, because of the background noise in the input shown in Figure 3.7(b). This can be fixed with more sophisticated interpolation in the mapping to pseudo-depth, but, on balance, I conclude that the full plane-wave domain naturally produces the most artifact-free output of the three domains.

3.6 2D coupled plane-wave domain prediction

Next I consider the numerical characteristics of the full 2D coupled plane-wave domain internal multiple prediction algorithm. I again create a benchmark 2D synthetic reflection seismic data set, created using a fourth order finite difference simulation of waves in an

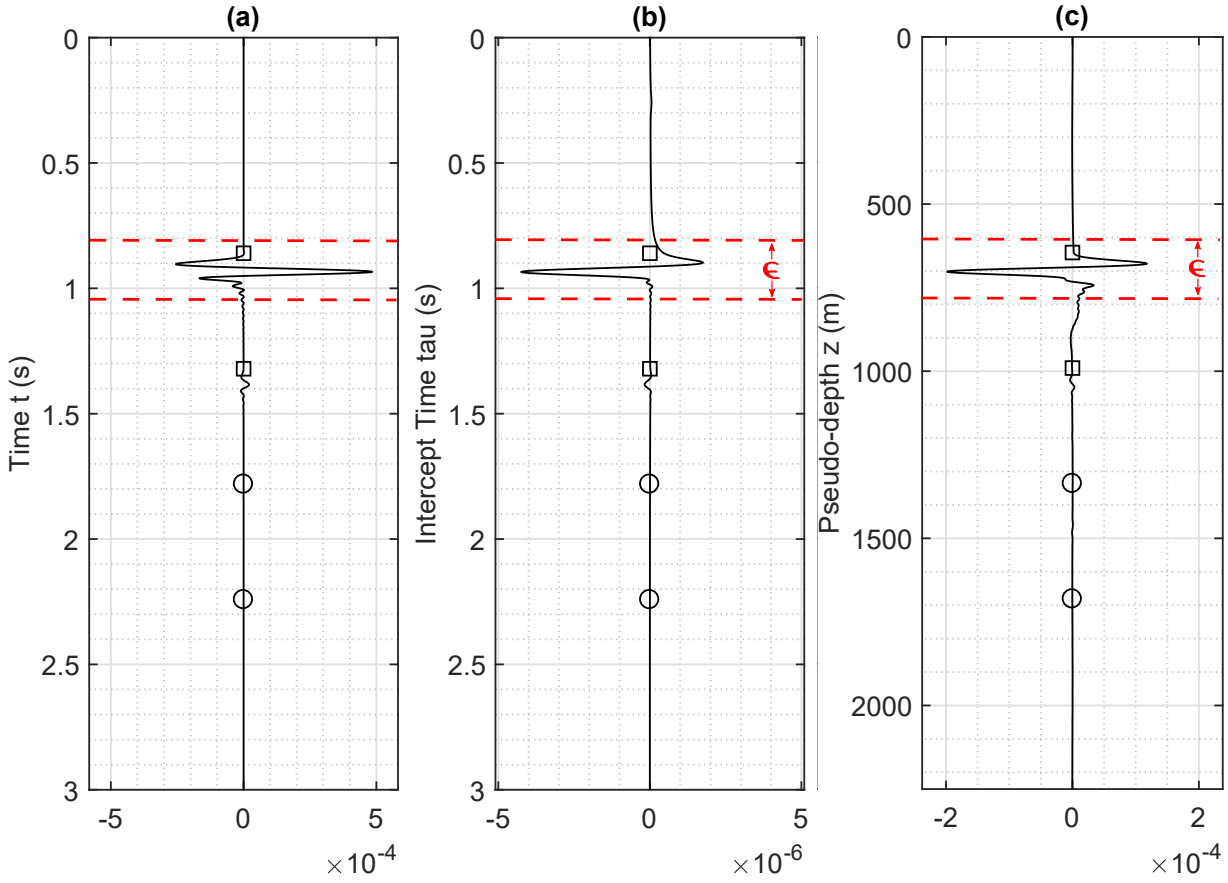

Figure 3.8: Trace comparisons and choice of search-limiting parameter ϵ: (a) zero-offset trace extracted from the raw data; (b) input $b_1(p, \tau)$ stacked over p, (c) input $b_1(p, z)$ stacked over p.

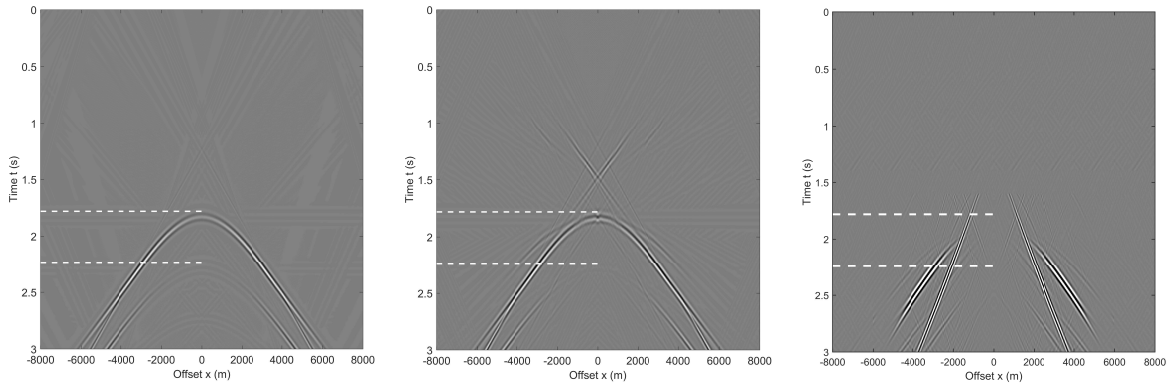

(a) (b) (c)

Figure 3.9: Internal multiple prediction gathers as computed in the three different domains, from the raw data as plotted in Figure 3.6(a): (a) prediction in p-τ domain with a constant $\epsilon = 0.2s$ and the input shown in Figure 3.7(a), (b) prediction in the p-z domain with a constant $\epsilon = 150m$ and the input shown in Figure 3.7(b), (c) prediction in the k_g-z domain with a constant $\epsilon = 150m$ and the input shown in Figure 3.7(c).

acoustic, constant density medium with absorbing boundaries. The velocity model contains 4-layers and three reflectors, two dipping and one flat, as shown in Figure 3.10. 160 geophones at 20 m intervals were embedded just below the surface, and shot records were generated with a 20Hz Ricker wavelet for source locations moving from left to right and occupying each geophone location. An Ormsby filter of [5Hz, 10Hz, 30Hz, 40Hz] is applied on all shot records. The source-receiver-time volume of multi-shot records is illustrated in Figure 3.11.

In Figure 3.12 three common shot gathers extracted from the 3D volume are illustrated, corresponding to sources located at 780m, 1580m, and 2380m. Three primaries are identifiable and are indicated with arrows; the other five events in each shot gather are first-order internal multiples. Some discretization noise and boundary reflections are visible but these do not obscure the real arrivals or alter our interpretations. The 2D character of the data due to the dipping layer is clearly visible, for instance in the lateral shift of the apexes of the hyperbolas.

After the removal of any directly-arriving wave energy (Weglein et al., 1997), which I have carried out through modeling and subtraction, the main pre-processing step is the double

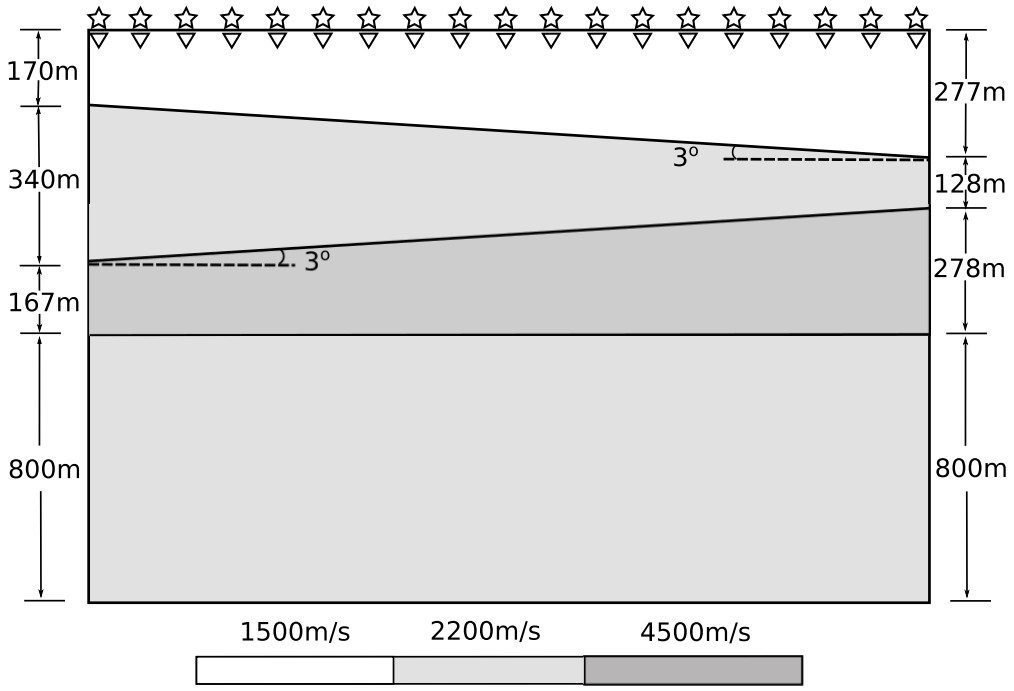

Figure 3.10: Four-layer velocity model for benchmark synthetic for the 2D internal multiple prediction algorithm. A fourth order finite difference solution of the acoustic constant density wave equation with absorbing boundaries is employed. The layer velocities are: $1500m/s$ in the top layer, $2200m/s$ in the second layer, $4500m/s$ in the third layer, and $2200m/s$ in the bottom layer.

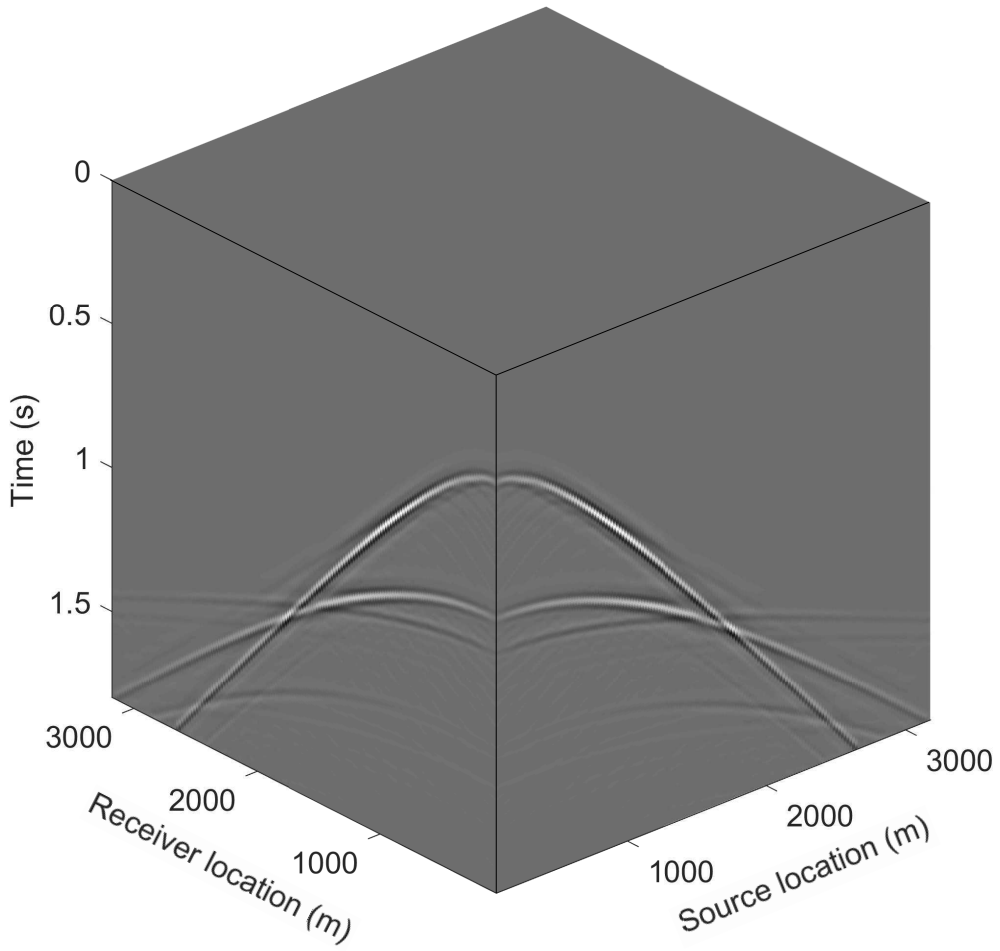

Figure 3.11: Illustration of the synthetic source-receiver-time data volume generated from the velocity model in Figure 3.10.

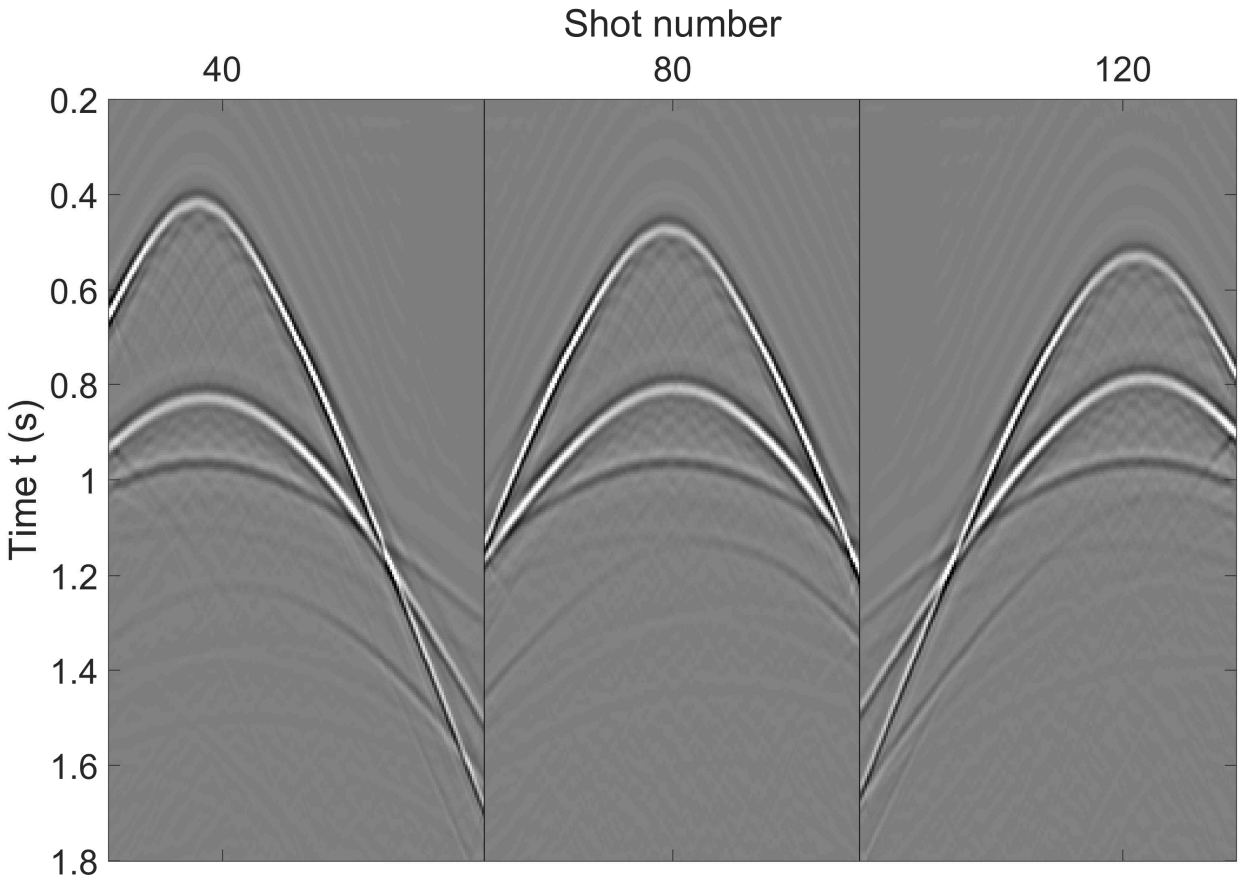

Figure 3.12: Three common shot gathers extracted from volume $d(x_g, x_s, t)$,from left to right: 40th-shot, 80th-shot, and 120th-shot.

τ-p_s-p_g transform (as in equation 3.12), which after being carried out on the data set leads to a 3D volume in horizontal slowness (for source and receiver, separately) and intercept time. Three common p_s gathers extracted from this volume, at p_s values of -0.3s/km, 0.0s/km, and 0.3s/km, are plotted in Figure 3.13. I note that relative to the 1.5D case, the signals in the double τ-p_s-p_g domain are less localized and exhibit some "butterfly" artifacts. These are aperture effects which can be mitigated with muting or by invoking high-resolution transforms (e.g., Sacchi and Porsani, 1999; Trad et al., 2003); here I apply muting only, remarking (in the discussion section) about the possible role high-resolution transforms may play in the future. Next, the data volume is scaled by the factor $-i2q_s$ to produce the final form of the input for the prediction algorithm. In Figure 3.14 three common p_s gathers extracted from the algorithm input volume $b_1(p_g, p_s, \tau)$ at the same values of p_s used in Figure 3.11 (-0.3s/km, 0.0s/km, and 0.3s/km) are illustrated.

The internal multiple prediction is then calculated on the transformed input for all of the 160 shot gathers via equation 3.6. An inverse τ-p_g-p_s transform is, lastly, applied to return the prediction to source-receiver-time coordinates. The predicted internal multiple volume is plotted in Figure 3.15. Extractions from this volume corresponding to three shot positions (the same locations as those in Figure 3.12), are shown in Figure 3.16.

Comparing Figures 3.12 and 3.16, I conclude that the predicted internal multiples correctly capture the arrival times, moveout patterns, and relative amplitudes. For instance, the brightening visible in the multiples at the right edge of shot 40 and the left edge of shot 120 is clearly captured in the prediction. However, the side lobes of the predicted multiples are somewhat wider than those of the events in the input data. This is likely tied to our current robust coupled τ-p_g-p_s transform algorithm and wavelet-dependent factor, which lowers the resolution of the inverse-transformed results.

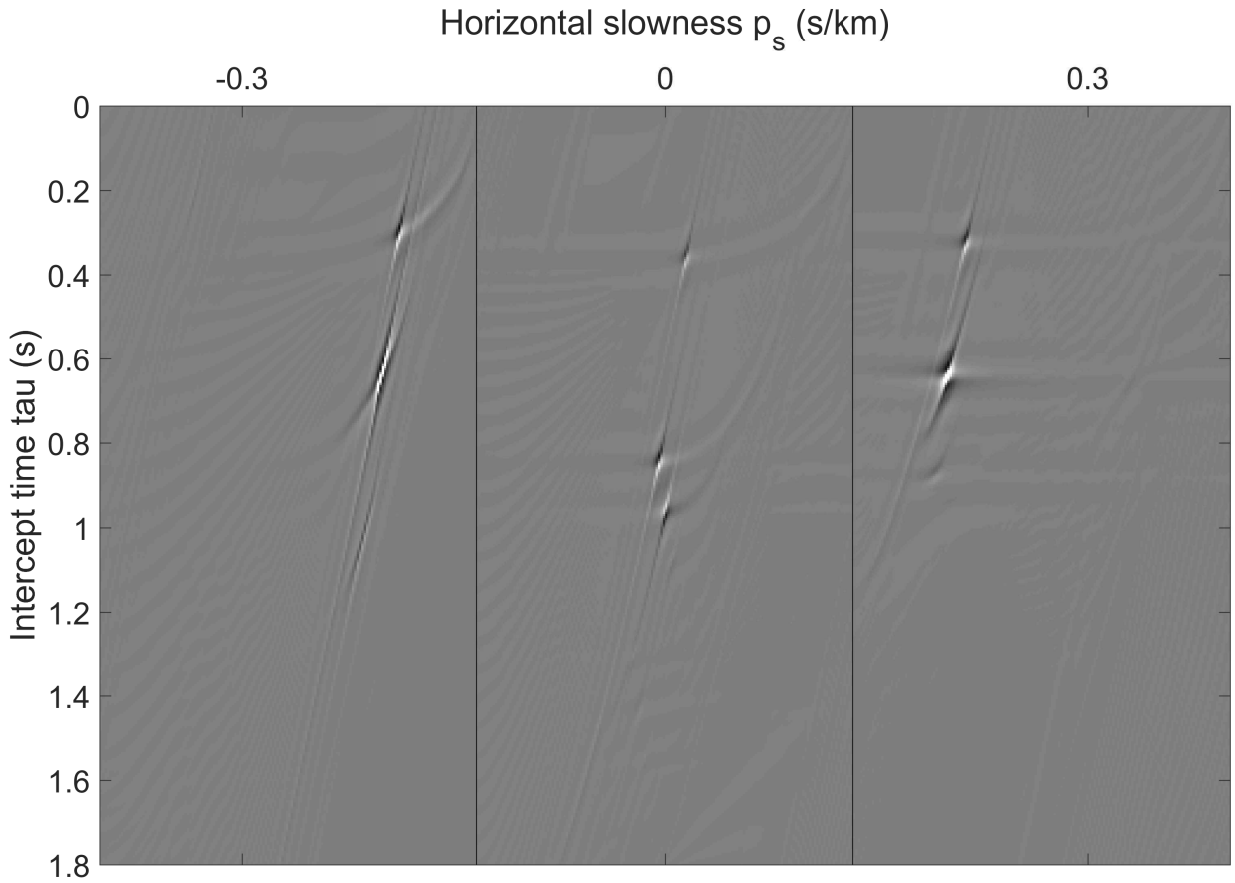

Figure 3.13: Three common p_s gather extracted from the double plane-wave transformed data volume. From left to right: $p_s = -0.3s/km, 0s/km, 0.3s/km$.

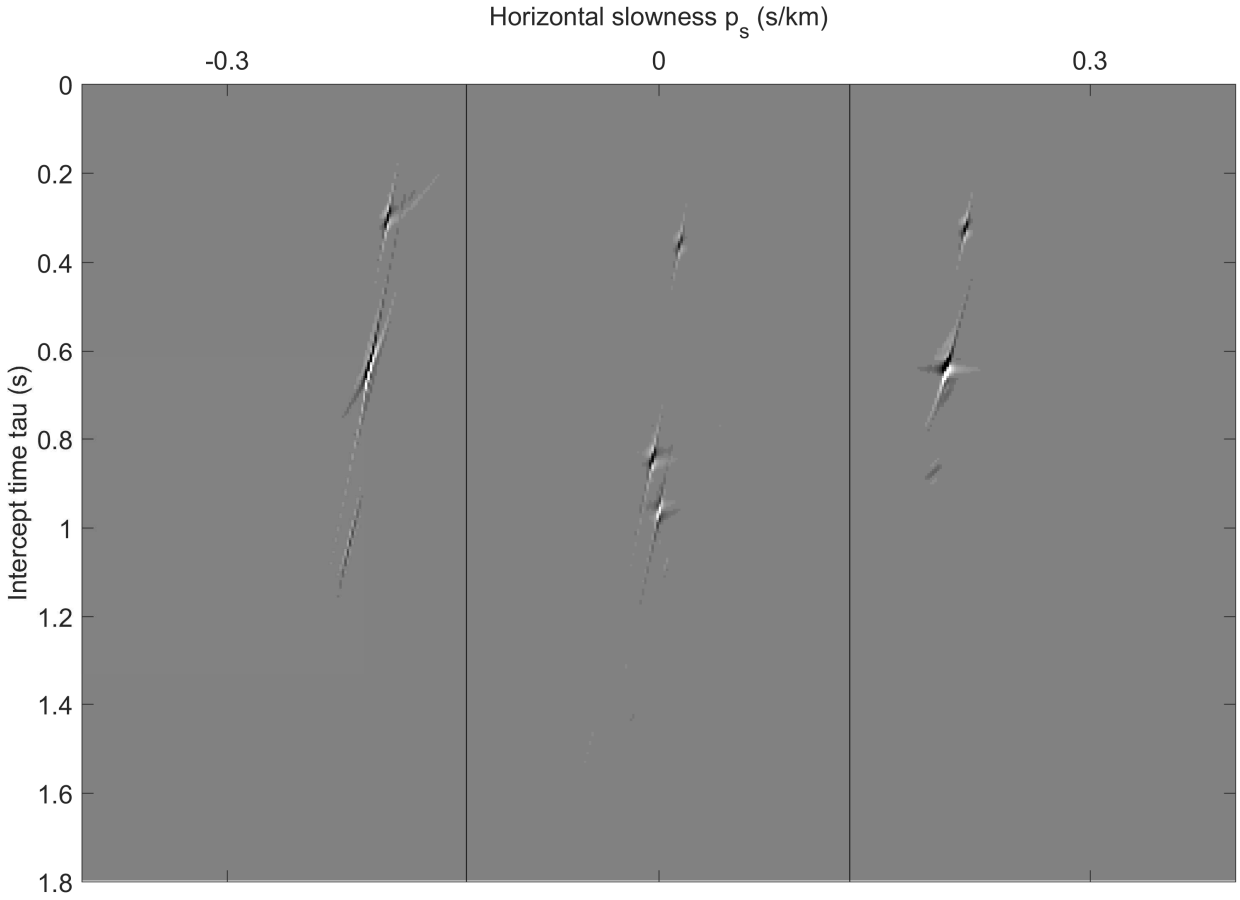

Figure 3.14: Three common p_s gather extracted from prediction input volume $b_1(p_g, p_s, \tau)$. From left to right: $p_s = -0.3s/km, 0, 0.3s/km$.

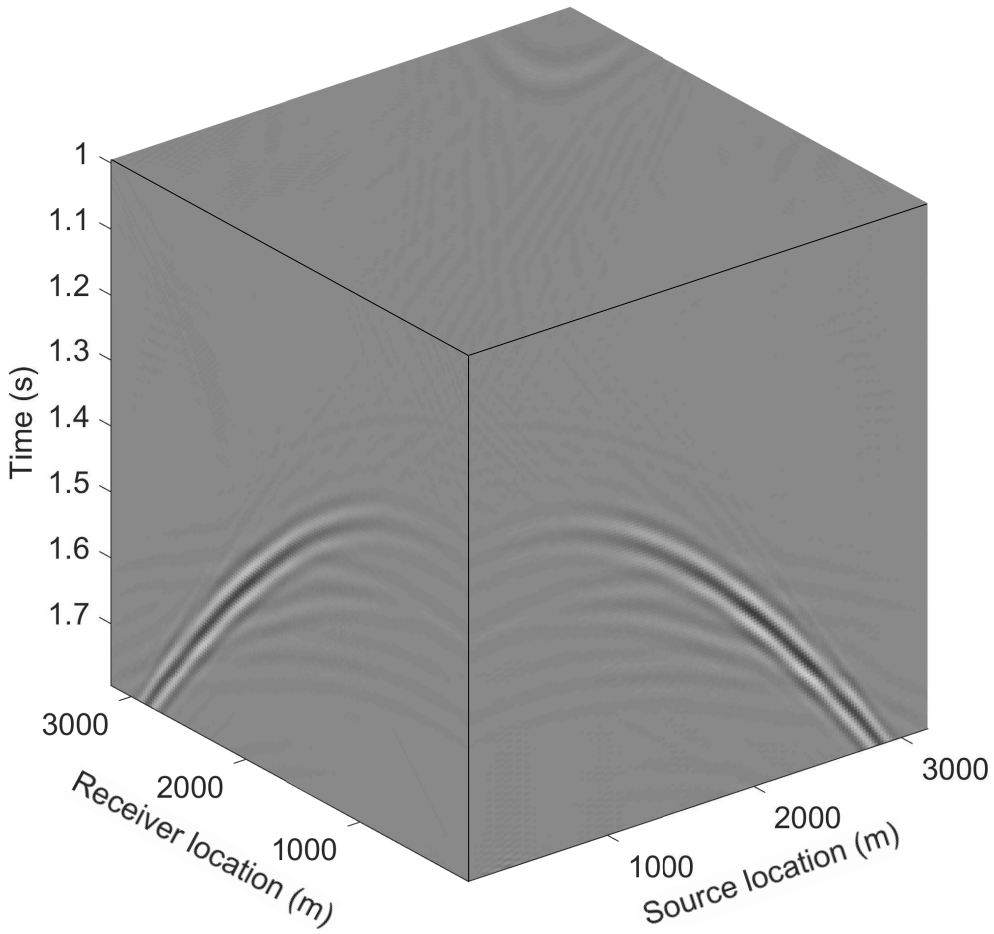

Figure 3.15: Predicted internal multiple source-receiver-time volume.

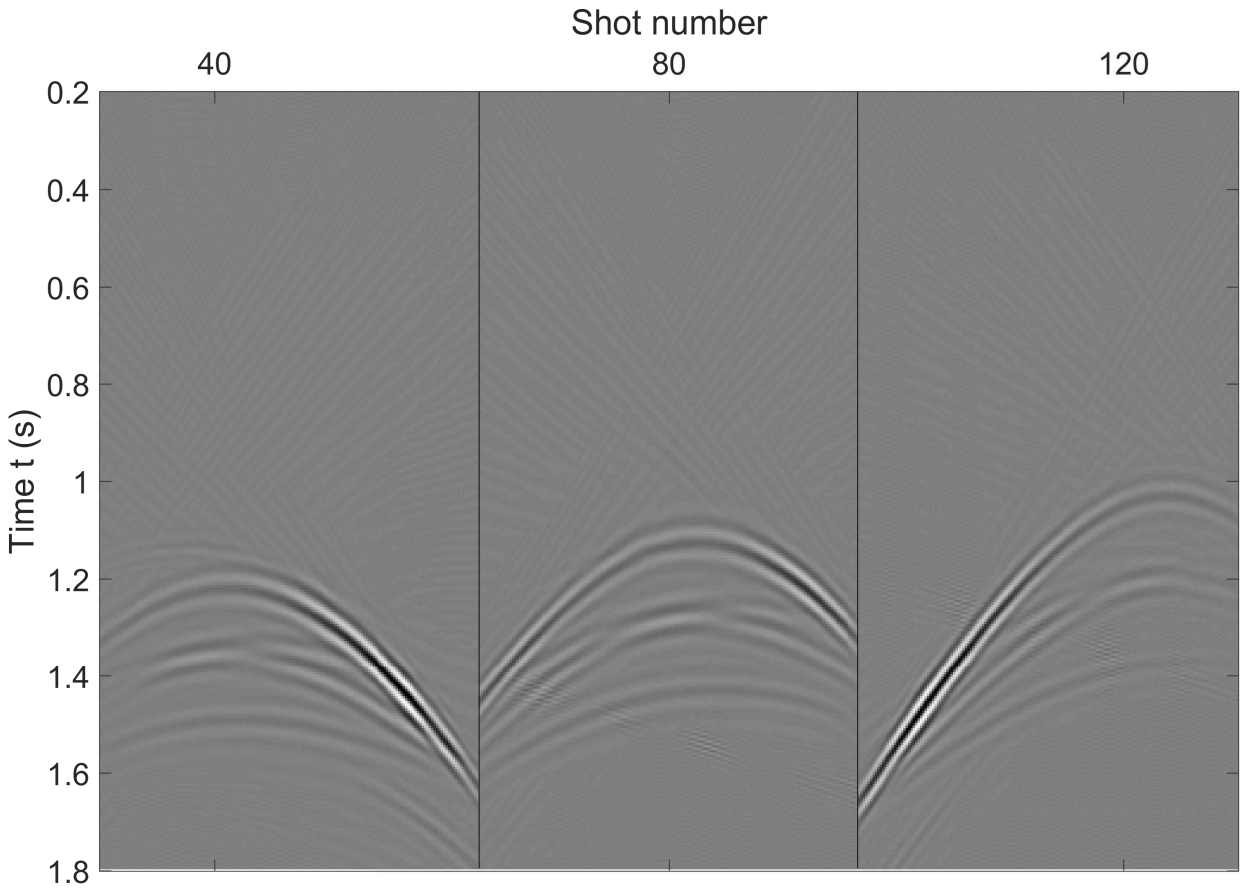

Figure 3.16: Three common shot gathers extracted from the internal multiple prediction volume in Figure 3.15; for comparison these are the same shot points as those of the raw shot gathers illustrated in Figure 3.12.

3.7 Conclusions

Internal multiples in complex and incompletely characterized media, caused by unknown or imperfectly known generators, can be predicted with the inverse scattering series internal multiple attenuation algorithm in an automatic manner. Implementation domain and parameter selection are important aspects of successful application of this method, especially on land. I present an implementation of the internal multiple prediction in the coupled (or double) plane-wave domain, which requires a tailoring of the prediction algorithm and a high fidelity τ-p_g-p_s transform. Comparing prediction inputs derived for a range of calculation domains, I conclude that the horizontal slowness domain, by concentrating the amplitudes of each sub-event, which in turn leads to a simpler and more stationary search-parameter selection, is generally optimal. The plane-wave domain algorithm leads to relatively stationary optimum ϵ values, and produces fewer artifacts traceable to poor parameter selection.

These conclusions provide incentive to implement the 2D coupled plane-wave version of the prediction algorithm, which has not been reported before in the literature (though the formula itself dates back to the 1990s). The input in this domain appears as a highly sparse matrix which significantly reduces its computational expense.

The coupled plane-wave domain is observed to cleanly separate primary and multiple events, capturing relative amplitudes, travel times and event trajectories. Standard slant-stack transforms of the type I have used to date tend to impose resolution restrictions, however, and this can be observed to affect the waveform match between the prediction and the actual multiples. Next steps in research branch from this observation. First, the presence in the literature of high-resolution Radon transform methodologies (e.g., Sacchi and Porsani, 1999; Trad et al., 2003) suggests a natural next step in mitigating the resolution issues arising from transform effects, and from many of the issues arising in prediction on field data where data completeness is often a problem. And the high-resolution Radon transform may significantly reduce the computational expense of 3D prediction, which is the subject of

current research. Second, elastic inverse scattering series prediction methods, which properly incorporate and account for multiples involving elastic conversions, exist, but their implementation in the plane-wave domain (rather than the wavenumber/pseudo-depth) introduces some difficulties. The fidelity of the plane-wave domain predictions illustrated in this Chapter provides good reason to engage with those difficulties in extending to multicomponent prediction. I will report on progress in this area in a future communication.

Chapter 4

Inverse scattering series internal multiple prediction in common-midpoint domain

4.1 Summary

Inverse scattering series internal multiple prediction accommodates fully multidimensional subsurface geological structures and 3D seismic survey data, but the computational expense of the algorithm makes its application on large 2D and small 3D data sets (even in the coupled plane-wave domain) impractical. The 1D prestack (1.5D) version of the algorithm is, in comparison, computationally quite cheap, and it is natural to ask whether using this algorithm on data over structures with (say) shallow dip is possible without the introduction of serious error. Here the difference between between data records over dipping strata sorted into shot/receiver and common midpoint (CMP) gathers is important, and so this is theoretically analyzed. Numerical analysis of prediction error shows that the 1.5D prediction algorithm has a much greater capacity for accommodating dipping generators in the CMP domain than on shot/receiver gathers. In the CMP domain the 1.5D algorithm is remarkably forgiving to dip, though it is not difficult to choose dipping angles large enough to cause the 1.5D prediction algorithm to fail in both CMP and shot/receiver domains (making the full 2D internal multiple prediction algorithm necessary). The key contribution I make in this chapter is the introduction of a modified version of the prediction algorithm appropriate for CMP gathers, which is derived based on the full 2D plane-wave theory.

4.2 Introduction

Seismic records associated with individual sources (shot or source records) are often sorted into common midpoint (CMP) gathers (e.g., Yilmaz, 2001). Multiple attenuation methods have been formulated for application on CMP gathers, based on their periodicity or difference of velocity stacking between multiples and primaries, such as predictive deconvolution, Radon transform (Foster and Mosher, 1992; VerWest, 2002; Trad, 2003) and velocity stacking (Hampson, 1986; Lumley et al., 1995; Yilmaz, 2001) which works at near- or far-offsets, respectively, for surface-related or layer-interbed multiples. However, in complex land data, with no periodicity and unclear velocity discriminations, interbed multiples prediction encounters difficult challenges, and the inverse scattering series approach may be warranted. It turns out that a re-formulation of the 1D prestack (1.5D) version of the inverse series method in the CMP domain has a greatly reduced sensitivity to small-to-moderate angle dipping strata as compared to its standard form. In this chapter, I modify the algorithm to accommodate CMP gather input. Considering computational burden of multidimensional implementation, for some cases, internal multiples may be predicted using 1.5D prediction algorithm with acceptable tolerances of prediction errors. The numerical simulated examples allow us to exemplify the error analysis of implementing 1.5D algorithm on dipping strata and examine the difference between CMP gathers and shot/receiver records.

4.3 Plane-wave domain inverse scattering series internal multiple prediction review

Araújo (1994) and Weglein et al. (1997) originally presented the prediction algorithm in the wavenumber/pseudo-depth $(k_g, k_s, \tilde{z})$ domain. Based on the close relationship of wavenumber and horizontal slowness ($k = \omega p$), Sun and Innanen (2018) re-wrote the algorithm in the horizontal-slowness/pseudo-depth $(p_g, p_s, \tilde{z})$ domain, pointing out some advantages in this

implementation. By taking advantage of the connection between pseudo-depth and vertical traveltime (Nita and Weglein, 2009b; Sun and Innanen, 2015), Sun and Innanen (2018) also formulated internal multiple prediction in the coupled plane-wave domain (p_g, p_s, τ), which was first presented by Coates et al. (1996), and summarized some further significant advantages of the algorithm, such as reduced computational burden, and the relative ease of selection of the search parameter ϵ.

Let $d(x_g, x_s, t)$ represent a fully deghosted 2D seismic data set involving waves downgoing from the source and upgoing to the receiver, with x_g being the inline receiver coordinate, x_s being the inline source coordinate, and t being the two-way traveltime. Let $D(p_g, p_s, \tau)$ represent the data set after coupled plane-wave transformation across all three coordinates, with p_g and p_s being the horizontal slowness conjugate to x_g and x_s, respectively, and τ being the vertical traveltime coupling with p_g and p_s. The plane-wave domain inverse scattering series internal multiple prediction algorithm is written as (Coates et al., 1996; Sun and Innanen, 2018)

$$\begin{aligned} b_{IM}(p_g, p_s, \omega) =& \frac{-1}{(2\pi)^2} \iint_{-\infty}^{+\infty} \mathrm{d}p_1 \mathrm{d}p_2 e^{\mathrm{i}\omega(\tau_{1s}-\tau_{1g})} e^{\mathrm{i}\omega(\tau_{1g}-\tau_{1s})} \int_{-\infty}^{+\infty} \mathrm{d}\tau_1 e^{\mathrm{i}\omega\tau_1} b_1(p_g, p_1, \tau_1) \\ & \times \int_{-\infty}^{\tau_1-\epsilon} \mathrm{d}\tau_2 e^{-\mathrm{i}\omega\tau_2} b_1(p_1, p_2, \tau_2) \int_{\tau_2+\epsilon}^{+\infty} \mathrm{d}\tau_3 e^{\mathrm{i}\omega\tau_3} b_1(p_2, p_s, \tau_3), \end{aligned} \tag{4.1}$$

where

$$q_X = \sqrt{\frac{1}{c_0^2} - p_X^2}, \tag{4.2}$$

with q_X being the vertical slowness associated with the horizontal slowness p_X, and the reference velocity c_0. The input is the 3D[1] data volume calculated by scaling the data after coupled τ-p_s-p_g transformation: $b_1(p_g, p_s, \tau) = -i2q_s D(p_g, p_s, \tau)$. These three events combined to reconstruct the ray-path of internal multiples are interrelated through their horizontal slowness on source and receiver sides. Figure 4.1 shows the relationship scheme between primaries and predicted internal multiple according to their contributing slownesses,

[1]This is a 3D data volume, not a 3D seismic acquisition being treated.

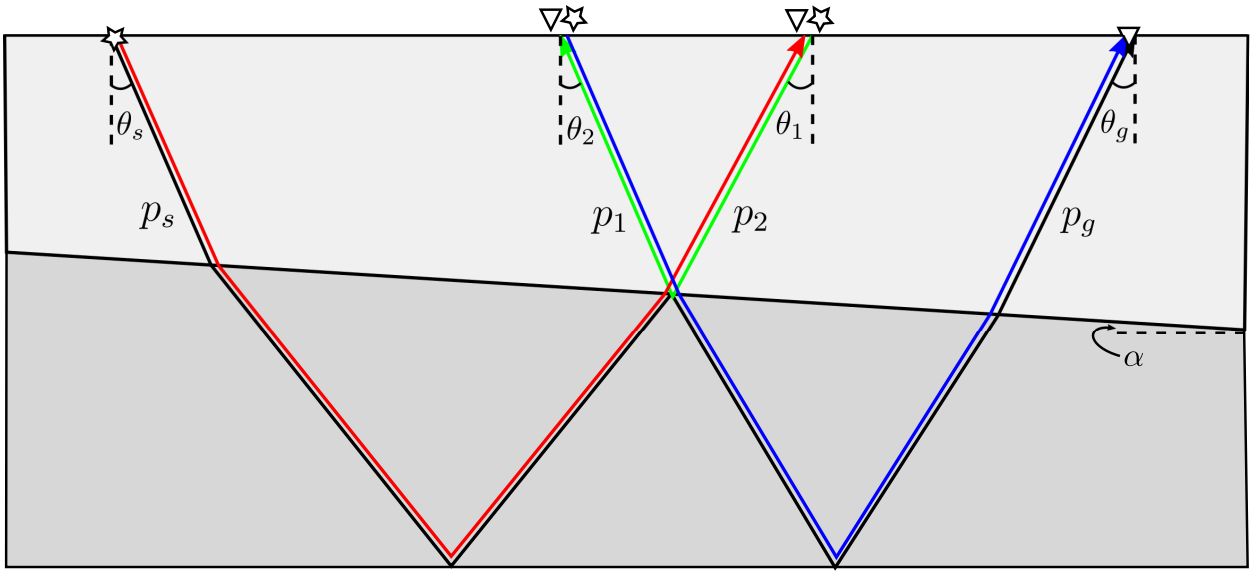

Figure 4.1: Ray-path schematic of primaries (dashed line) and internal multiple (solid line) with corresponding source and receiver locations. See also Coates et al. (1996).

i.e., p_g, p_s, p_1, and p_2 in equation 4.1. The quantities p_1 and p_2 represent horizontal slownesses at both source and receiver locations within the algorithm. This will be of practical computational importance, as it requires that matching source and receiver sides slownesses must be available either naturally through acquisition or through data reconstruction. As shown in Figure 4.1, the exact traveltime of internal multiple can be calculated by summing over two primaries from lower reflector and then subtracting the one from upper interface.

4.4 Developments on the 1D prestack algorithm

The prediction algorithm in the coupled plane-wave domain (p_g, p_s, τ) can be simplified to reflect the fact that $p_g \equiv p_2 \equiv p_1 \equiv p_s \equiv p$, if a layered Earth is assumed. With the additional assumption that all sources and receivers are located at the same depth, the plane-wave domain prediction algorithm in equation 4.1 reduces to

$$b_{IM}(p,\omega) = -\frac{1}{(2\pi)^2}\int_{-\infty}^{+\infty} \mathrm{d}\tau_1 e^{\mathrm{i}\omega\tau_1} b_1(p,\tau_1) \int_{-\infty}^{\tau_1-\epsilon} \mathrm{d}\tau_2 e^{-\mathrm{i}\omega\tau_2} b_1(p,\tau_2) \int_{\tau_2+\epsilon}^{+\infty} \mathrm{d}\tau_3 e^{\mathrm{i}\omega\tau_3} b_1(p,\tau_3), \tag{4.3}$$

where p is the horizontal slowness whose physical meaning is related to the type of input. τ is the vertical traveltime coupling with horizontal slowness p. As indicated before, the input is a transformed and scaled version of the originally recorded data: $b_1(p,\tau) = -i2q_sD(p,\tau)$. The transformed data $D(p,\tau)$ are in this case computed from a standard τ-p or slant-stack transformation of a shot/receiver gather, or CMP gather.

Equation 4.3 implies that, for layered media, all internal multiples in a common shot/receiver, or CMP gather, can be reconstructed from that gather alone (this is an expected result, since all shot and CMP records are identical over layered media). Compared to equation 4.1, the 1.5D prediction algorithm is much more efficient since the prediction can be looping over trace-by-trace (common p trace) due to the independence of variant horizontal slowness p. However, for dipping strata, predicting internal multiples using a 1.5D algorithm loses accuracy.

4.4.1 1.5D prediction scheme on common shot/receiver gathers

Implementation of the 1.5D internal multiple prediction algorithm in the plane wave domain requires a traditional slant-stack transform of the seismic record multiplied by a weighting factor as input. Ocola (1972) and Diebold and Stoffa (1981) demonstrated that traditional $\tau - p$ mapping can be performed by considering traveltimes for varying offsets in a common shot gather,

$$t = p_g x + \sum_i z_{si}(q_{si} + q_{gi}), \tag{4.4}$$

or, varying offsets in a common receiver gather,

$$t = p_s x + \sum_i z_{gi}(q_{si} + q_{gi}), \tag{4.5}$$

where t is the two way traveltime of the event being described, and x is the offset. The variables q_{si} and q_{gi} are the vertical components of slowness in the i^{th} layer for the source and receiver respectively. The depths z_{si} and z_{gi} are the thicknesses of the i^{th} layer below the source and receiver locations respectively.

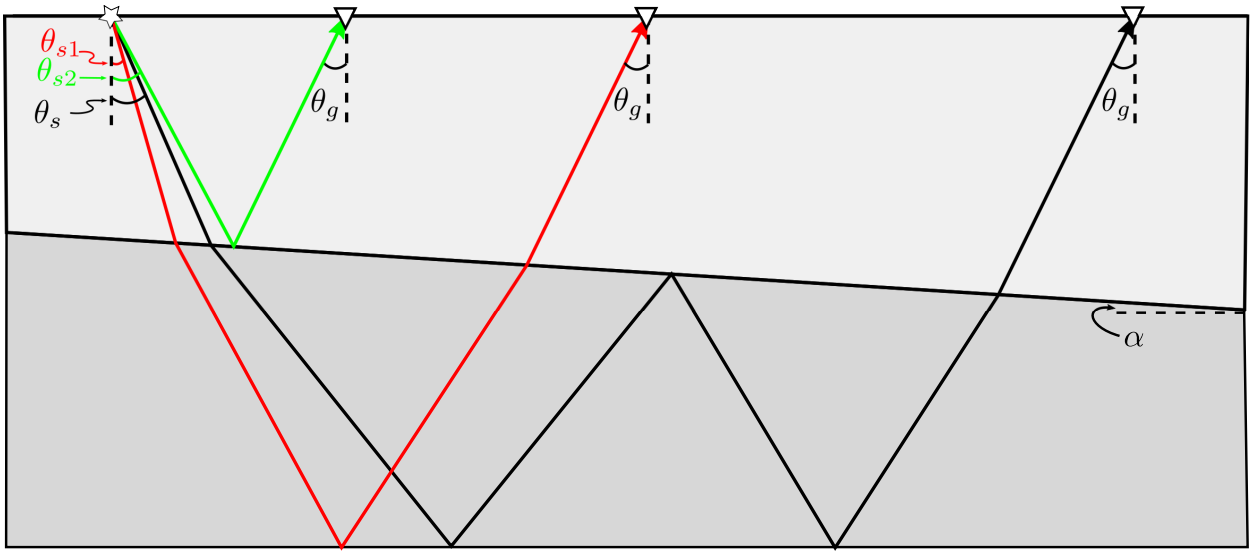

Figure 4.2: Combinations of events in a common shot gather for internal multiple prediction using 1.5D algorithm. Both primaries and internal multiples shared the same horizontal slowness corresponds to receiver side, i.e., p_g.

Equation 4.4 and 4.5 indicate that the horizontal slowness is associated with the receiver side ($p_g = \frac{sin\theta_g}{c_0}$) when the $\tau - p$ transformation is performed to a shot gather; the horizontal slowness is associated with the source side ($p_s = \frac{sin\theta_s}{c_0}$) when the transformation is applied to a receiver gather. Therefore, rather than the scheme illustrated in Figure 4.1, the 1.5D prediction algorithm (equation 4.3), for a common shot gather, predicts internal multiples based on lower-higher-lower ordering within traces with a common p_g; for a common receiver gather, it reconstructs internal multiples by combining sub-events within a common p_s trace. For example, Figure 4.2 illustrates common shot gather internal multiple prediction. The traveltime of the internal multiple indicated in black is predicted by twice the traveltime of the red primary reflection minus the traveltime of the green event. All primaries and predicted multiples in Figure 4.2 share the same receiver side horizontal slowness p_g.

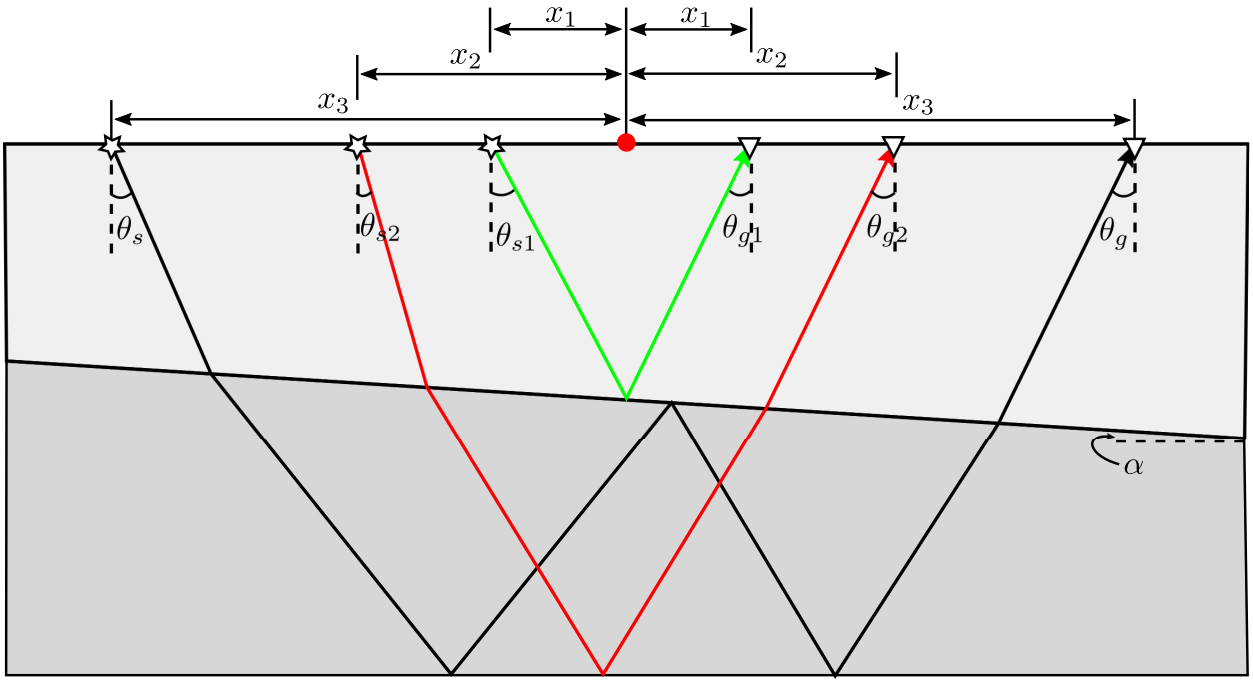

Figure 4.3: Combinations of events in a CMP gather for internal multiple prediction using 1.5D algorithm. All events in combination shared the same average horizontal slowness, i.e., $p_H = \dfrac{p_g + p_s}{2} = \dfrac{p_{g1} + p_{s1}}{2} = \dfrac{p_{g2} + p_{s2}}{2}$.

4.4.2 1.5D prediction scheme on common-midpoint gathers

To perform traditional $\tau - p$ transform on CMP gathers, Diebold and Stoffa (1981) also introduced a reference point M, located between the source and receiver, where M is the location of midpoint in the CMP gather. Based on this reference point location, the traditional $\tau - p$ transform on a CMP gather can be written as

$$t = p_H x + \sum_i z_{Mi}(q_{si} + q_{gi}), \tag{4.6}$$

where p_H is the average horizontal slowness, i.e., $p_H = \dfrac{p_g + p_s}{2}$, with respect to varying offsets x. The quantity z_{Mi} represents the thicknesses of the i^{th} layer below the midpoint. This implies that, with the weighted traditional $\tau - p$ transformed CMP gather as an input, implementing internal multiple prediction using 1.5D algorithm is performed by looping over common average horizontal slowness p_H traces. For instance, for a common CMP gather, the internal multiple shown in Figure 4.3 is predicted by doubling traveltime of the red primary event and then subtracting traveltime of the green one. All these events in Figure 4.3 are sorted in the CMP gather and have the equivalent average horizontal slowness p_H.

4.5 Numerical analysis of 1.5D algorithm on 2D cases

Before implementing internal multiple prediction with 1.5D algorithm on dipping strata, it is necessary to investigate the dipping angle dependency of the 1.5D algorithm and to discuss the discrepancy of performance using variant input types. To do so, we numerically simulated all ray-paths of primaries and 1st order internal multiples on a two-interface model, shown in Figure 4.2 or 4.3. The shallower reflector dips with an angle α (here, $\alpha > 0$ if depth of interface increases from left to right) while the deeper one is flat.

4.5.1 Shot gather error analysis

For a common shot gather, under a fixed source location and a fixed thickness of the 1st layer below the source point ($z_s = 400m$), ray-paths of three related events shown in Figure 4.2 were simulated with varying offsets x and dipping angles α. In addition to traveltimes of all ray-paths, the receiver-side horizontal slowness was also calculated for a certain offset x with a receiver angle θ_g, i.e., $p_g = \dfrac{sin\theta_g}{c_0}$. Therefore, using equation 4.4, the vertical traveltime (to distinguish with the one in CMP gather, here, it is indicated as τ_s) associated with a fixed p_g is $\tau_s = t - p_g x$.

The vertical traveltimes of three events extracted from common shot gathers in Figure 4.2 are plotted in Figure 4.4a. The top one represents vertical traveltimes of the first primary reflection, indicated in green in Figure 4.2, with varying dipping angles and receiver-side horizontal slownesses p_g. The middle one delineates vertical traveltimes of the second primary event, indicated in red in Figure 4.2. The bottom one are vertical traveltimes of internal multiples shown in Figure 4.2.

With 1.5D algorithm, the vertical traveltimes of the internal multiples are predicted by doubling vertical traveltimes of the second primary events and then subtracting vertical traveltimes of the first primaries, i.e., $\tau_{black} = 2\tau_{red} - \tau_{green}$. Compared to recorded internal multiples, the predicted errors with varying dipping angles α and horizontal slowness p_g were plotted in Figure 4.4b. Figure 4.4b demonstrated that, for shot gather internal multiple prediction on dipping strata with 1.5D algorithm, the absolute values of prediction errors dramatically raised (up to 0.2s) along increasing dipping angles and horizontal slownesses.

4.5.2 CMP gather error analysis

To analyze the behaviors of 1.5D prediction algorithm with CMP gathers on dipping layered cases, we also modeled all ray-paths and calculated traveltimes of three reflection events in Figrue 4.3 with varying offsets and dipping angles. With a fixed CMP location and a fixed

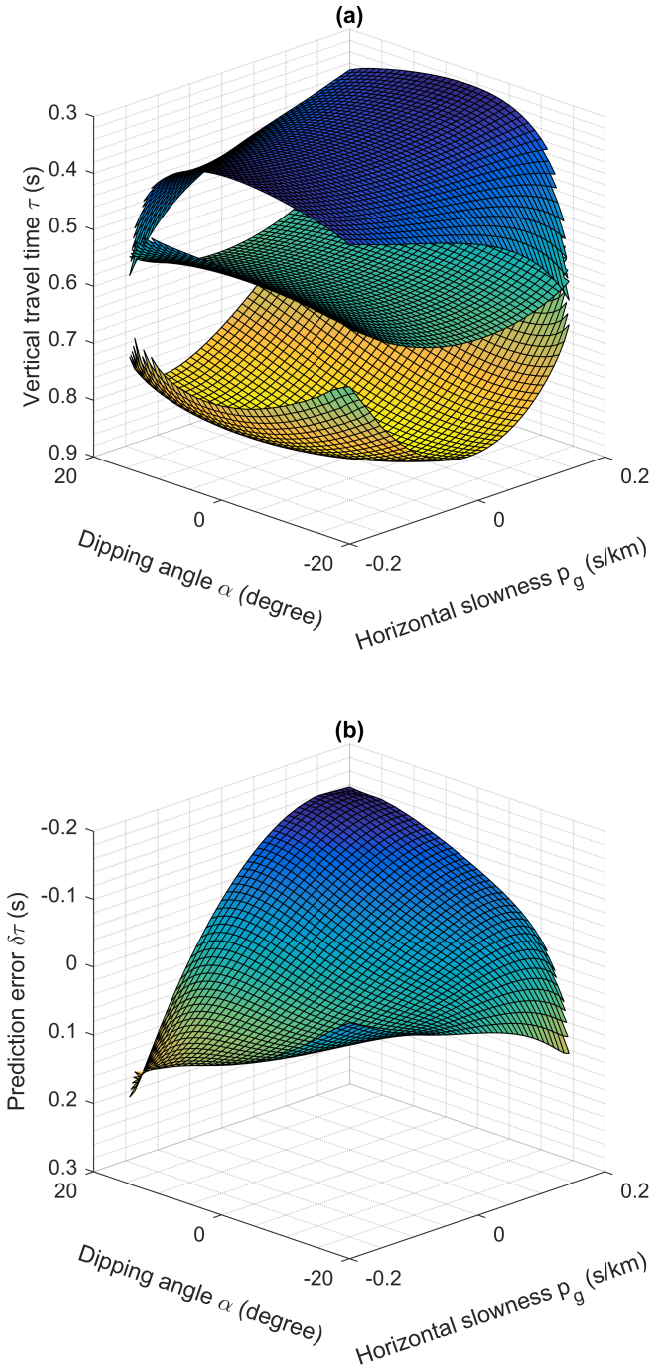

Figure 4.4: Error analysis of 1.5D algorithm on 2D cases using common shot gathers. (a) Vertical traveltimes of three events, shown in Figure 4.2, extracted from a common shot gather with varying dipping angles α and horizontal slownesses p_g, i.e., the top one represents vertical traveltimes of 1st primary reflection, indicated in green in Figure 4.2; the middle one shows vertical traveltimes of 2nd primary event, indicated in red i Figure 4.2; the bottom one delineates vertical traveltimes of internal multiples shown in Figure 4.2. (b) Prediction errors with shot gathers using 1.5D algorithm.

thickness of 1st layer below CMP ($z_M = 400m$), the obtained traveltimes were sorted into common average horizontal slowness p_H manner, i.e., $\tau_M = t - p_H x$. Here, τ_M represents the relative vertical traveltime related to CMP location and average horizontal slowness p_H.

Figure 4.5a shows vertical traveltimes τ_M of primaries and internal multiples extracted from CMP gathers, which their relationships were shown in Figure 4.3. The top one corresponds to the first primary indicated in green in Figure 4.3; the middle one represents the second primary indicated in red in Figure 4.3; and the bottom one delineates vertical traveltimes of internal multiples, with varying dipping angles α and average horizontal slownesses p_H respectively. Based on equation 4.3, the vertical traveltimes of internal multiples can be predicted by a lower-higher-lower combination over a fixed average horizontal slowness p_H. The prediction errors using CMP gather along varying dipping angles and average horizontal slownesses were plotted in Figure 4.5b. As indicated in Figure 4.5b, except the condition of around $\alpha = -20°$ and $p_H = 0.2s/km$, the predicted errors remained in range of $[-0.05, 0.06]$, which were much smaller than prediction errors of common shot gathers.

The comparisons of prediction errors between common shot and midpoint gathers, to analyzed instinctively, were extracted at fixed dipping angles and at fixed horizontal slownesses, respectively. Figure 4.6a-c show predicted errors of common shot and midpoint gathers at fixed dipping angle $\alpha = [-25°, 0°, 25°]$, separately, where the error of shot gather prediction is indicated in orange, and the prediction error of CMP gather is illustrated in dark-blue. In Figure 4.6a, with a fixed dipping angle $\alpha = -25°$, the error of internal multiple prediction using shot gather approximate linearly rises while the predicted error in CMP domain remains in a relatively smaller range. Figure 4.6b shows the prediction error of shot and CMP gathers with $\alpha = 0°$, i.e., a layered case. As indicated previously, under layered cases, 1.5D prediction algorithm can predict correct traveltime of internal multiples on both shot and CMP gathers. In Figure 4.6c, the error of predicted traveltime of internal multiples is calculated with $\alpha = 25°$. Similar with Figure 4.6a, comparing with the prediction error of shot

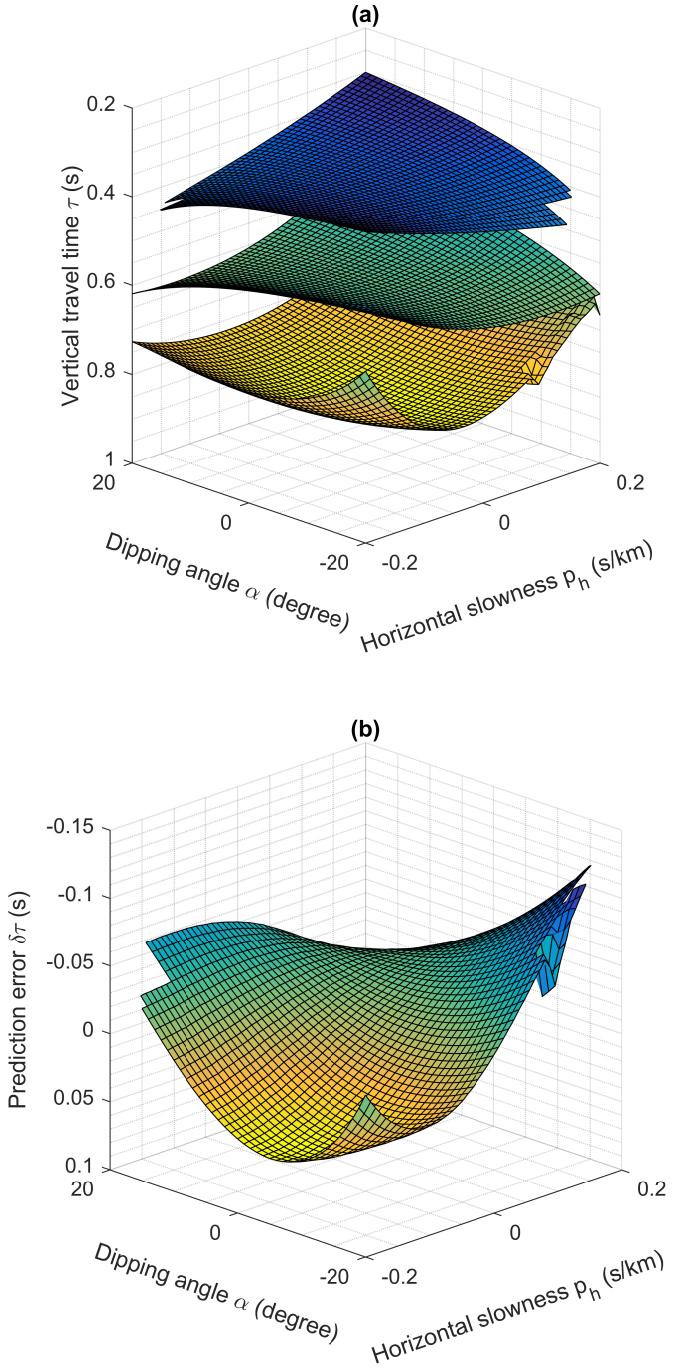

Figure 4.5: Error analysis of 1.5D algorithm on 2D cases using CMP gathers. (a) Vertical traveltimes of three events, shown in Figure 4.3, extracted from a CMP gather with varying dipping angles α and average horizontal slownesses p_H, i.e., the top one represents vertical traveltimes of 1st primary reflection, indicated in green in Figure 4.3; the middle one shows vertical traveltimes of 2nd primary event, indicated in red i Figure 4.3; the bottom one delineates vertical traveltimes of internal multiples shown in Figure 4.3. (b) Prediction errors with CMP gathers using 1.5D algorithm.

gathers, the implementation of 1.5D prediction algorithm in CMP domain input produces a much stable and independent results with varying horizontal slownesses, even under a large dipping angle condition.

The prediction errors of common shot and midpoint gathers at fixed horizontal slowness $p = [-0.1, 0.0, 0.1]s/km$ are also extracted and plotted in Figure 4.6d-f, respectively. All predicted errors of common shot and midpoint gathers are zero at dipping angle $\alpha = 0°$ in Figure 4.6d-f, which agrees with the fact in equation 4.3. However, at fixed horizontal slownesses, the prediction errors of shot and CMP gathers does not show the linear relationship with varying dipping angles and limited advantages may be found in CMP domain.

4.6 Example 1: 2D prediction with 1.5D algorithm

In this section, we created a three-layer model with velocity varies from top to bottom: [2200,3500,2200]m/s. The dipping angle of the top interface is 10°, and the lower one is flat. 640 shot gathers were generated to exact the CMP gather where the midpoint was located at the middle of model indicated as a red dot in Figure 4.7. The extracted CMP gather is shown in Figure 4.9a. To compare with prediction of CMP gather, a shot gather located at the same location was also selected and plotted in Figure 4.8a, for implementing 2D internal multiple prediction using 1.5D algorithm.

The internal multiple prediction of shot gather was shown in Figure 4.8b. Using 1.5D algorithm on shot gather, the prediction lost accuracy due to the outlying horizontal slowness caused by the dipping angle of reflector, especially at large offsets. For example, in Figure 4.8b, the traveltime prediction of the 1st-order internal multiple at largest negative offset was less than 0.7s, which was not agreed by the original shot record shown in Figure 4.8a. A non-stationary least-square subtraction was applied to remove the multiples from shot records, shown in Figure 4.8c. After subtraction, multiples were attenuated at near offsets, but failed at large offsets.

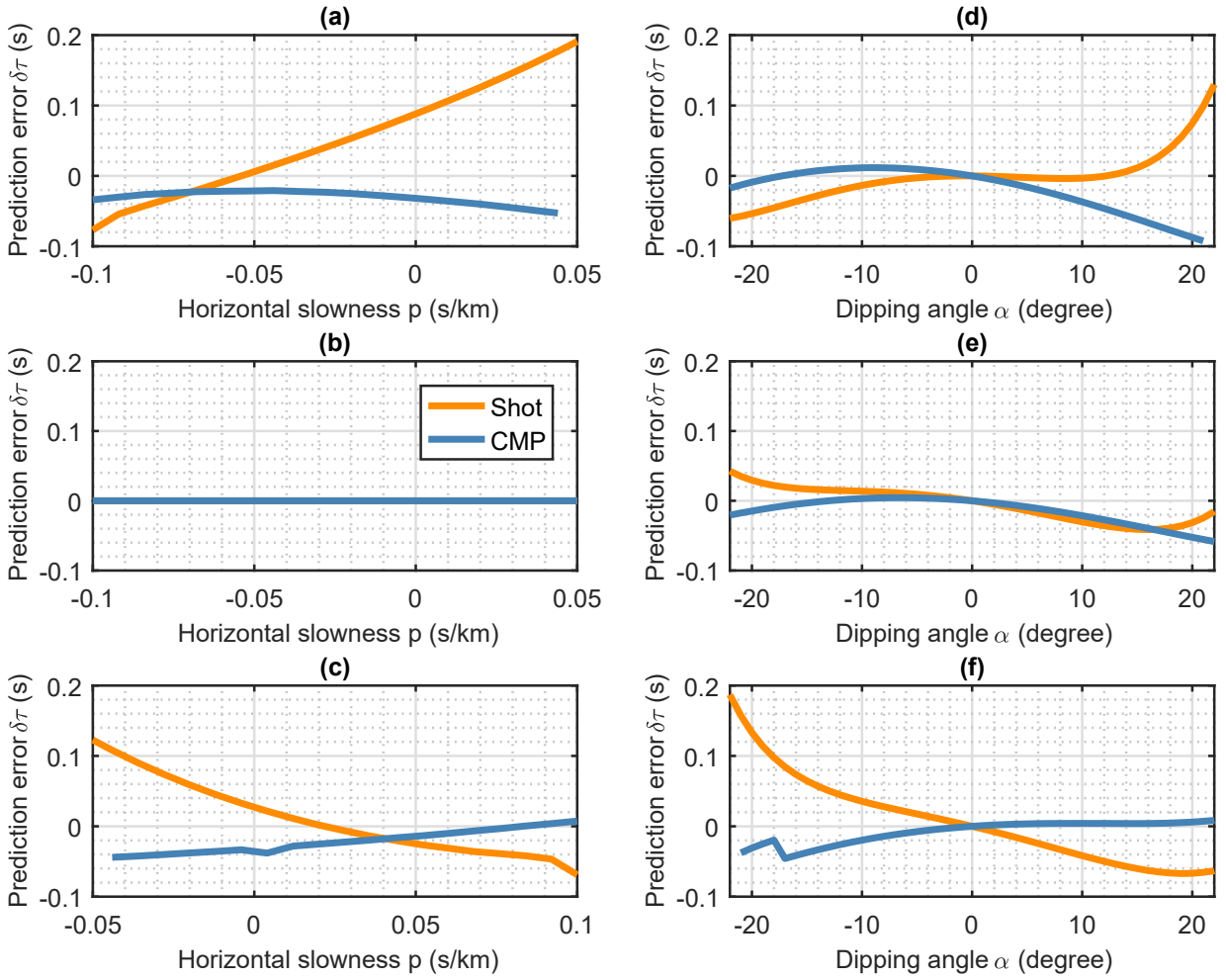

Figure 4.6: Comparisons of predicted errors between common shot and midpoint gathers at fixed dipping angle $\alpha = [-25°, 0°, 25°]$ and at fixed horizontal slowness $p = [-0.1, 0.0, 0.1]s/km$, respectively. The prediction errors of common shot gathers are indicated in orange and the one of CMP gathers are illustrated in dark-blue. (a) Comparisons of prediction errors at $\alpha = -25°$ with varying p. (b) Comparisons of prediction errors at $\alpha = 0°$ with varying p. (c) Comparisons of prediction errors at $\alpha = 25°$ with varying p. (d) Comparisons of prediction errors at $p = -0.1s/km$ with varying α. (e) Comparisons of prediction errors at $p = -0.0s/km$ with varying α. (f) Comparisons of prediction errors at $p = 0.1s/km$ with varying α. Note, for shot gathers, p represents p_g; for CMP gathers, p represents p_H.

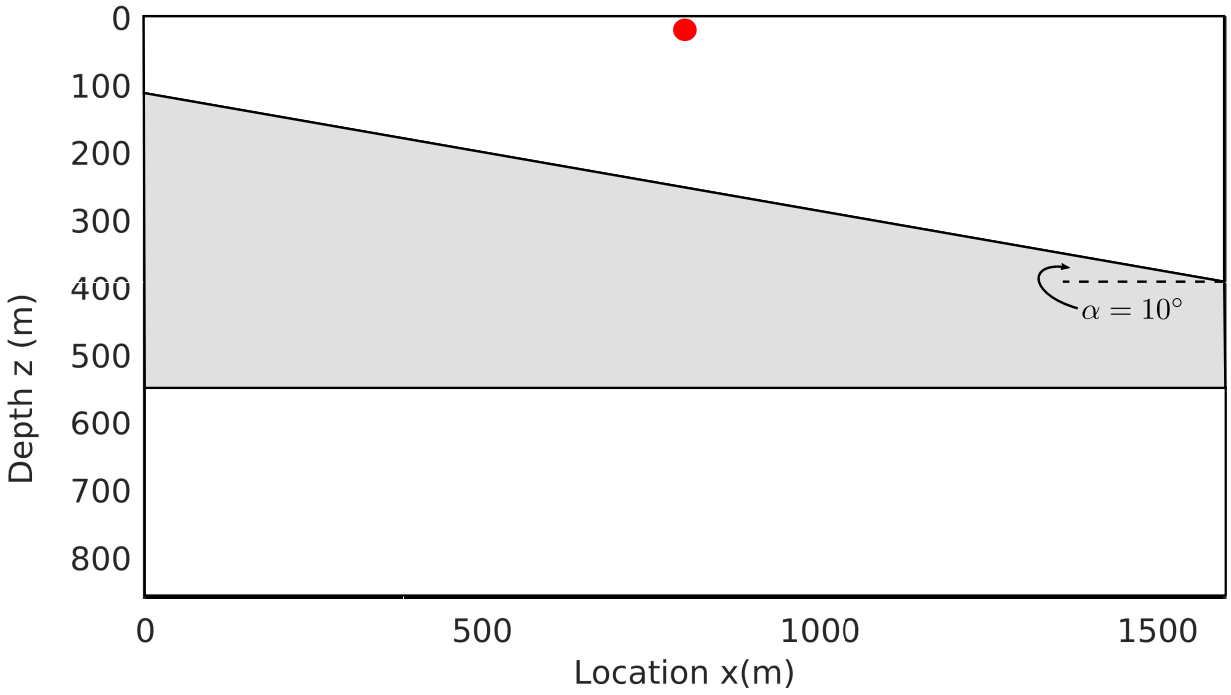

Figure 4.7: Two-interface model with one dipping and one flat reflectors. The dipping angle of the 1st interface is 10°. Here, the red dot indicates the source location for a common shot gather, and represents the CMP location for a CMP gather.

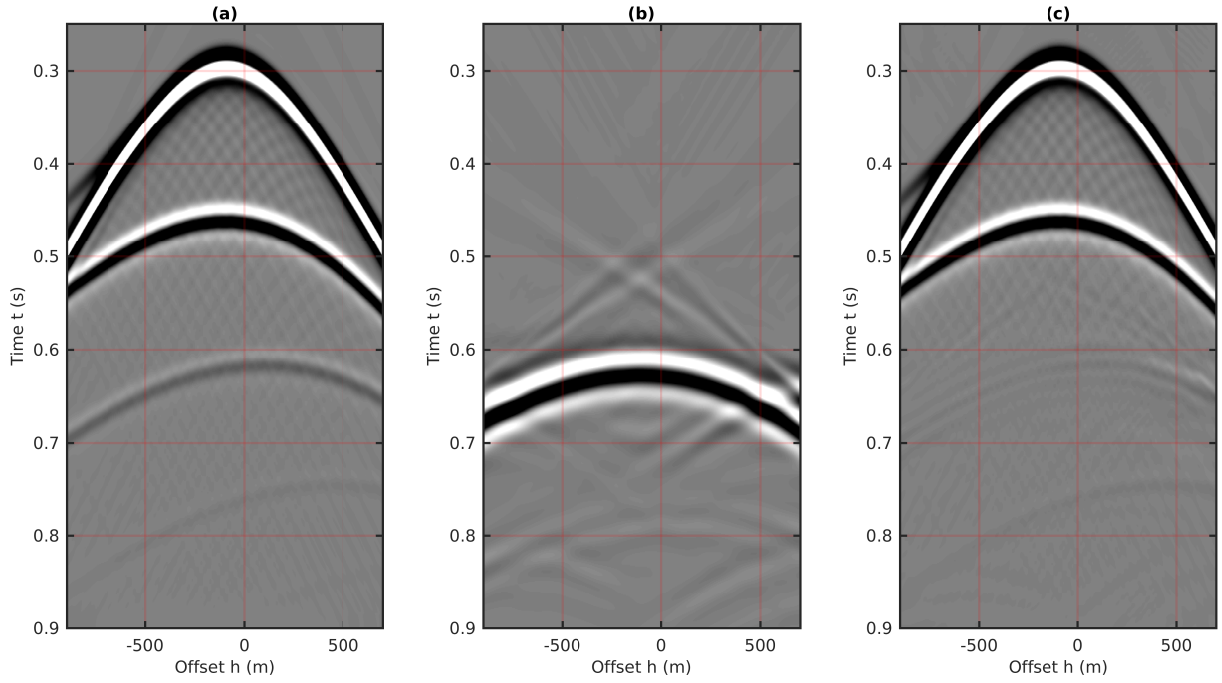

Figure 4.8: 2D internal multiple prediction in a common shot gather using 1.5D algorithm. (a) A shot gather created using velocity model shown in Figure 4.7 with source location indicated as the red dot. (b) Internal multiple prediction using equation 4.3. (c) The shot gather after least-square matching subtraction, i.e., c=a-factor*b.

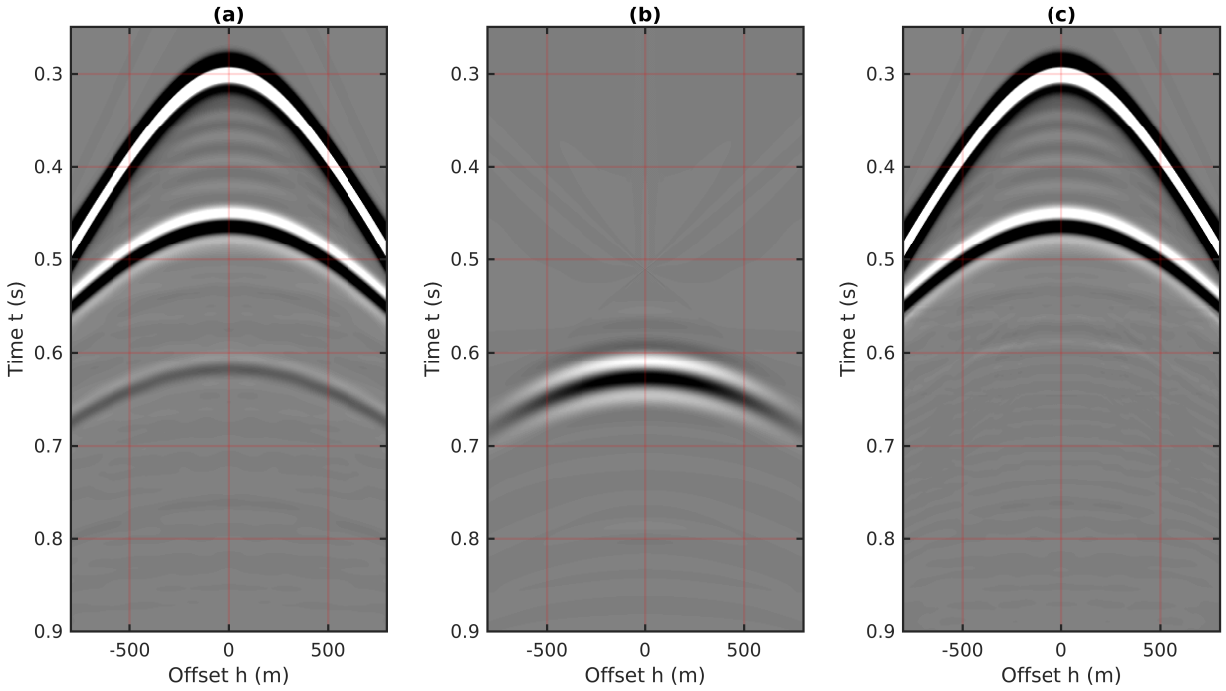

Figure 4.9: 2D internal multiple prediction in a CMP gather using 1.5D algorithm. (a) A CMP gather created using velocity model shown in Figure 4.7 with CMP location indicated as the red dot. (b) Internal multiple prediction using equation 4.3. (c) The CMP gather after least-square matching subtraction, i.e., c=a-factor*b.

Figure 4.9b shows 2D internal multiple prediction on CMP gather using 1.5D algorithm. The predicted traveltime of internal multiple was 0.6s at zero-offset and was around 0.69s at largest offsets which are consistent with original shot record. Compared to the shot gather prediction, internal multiples in CMP gather were well predicted both at near and far offsets. Figure 4.9c indicates that internal multiples were well eliminated using prediction of CMP gather and a non-stationary least square subtraction.

4.7 Plane-wave domain multidimensional internal multiple prediction algorithm in CMP gather

The numerical analysis and implementation indicated that, for internal multiple prediction on dipping strata, 1.5D inverse scattering algorithm has a comparatively tolerability on

CMP gathers instead of shot/receiver gathers, which is benefited from the average horizontal slowness. However, the accuracy of predicted internal multiples traveltime is significantly reduced when the dipping angle of reflector is extremely large. The 2D prediction algorithm on CMP gather is still necessary even though 1.5D implementation may handle most of simplified cases in practice.

Let $\tilde{d}(x_m, x_h, t)$ represents the sorted CMP gather of data $d(x_s, x_g, t)$, with varying offsets and CMP locations, and its coupled $\tau - p_m - p_h$ transformation across three variables is delineated as $\tilde{D}(p_m, p_h, \tau_M)$ with p_m and p_h representing the horizontal slowness conjugate to CMP location x_m and half-offset $x_h/2$, respectively, and τ_M being the vertical traveltime coupling with p_m and p_h. Considering the usual variable changes

$$\begin{aligned} p_m &= p_g + p_s \\ p_h &= p_g - p_s \end{aligned} \tag{4.7}$$

Substitute equation 4.7 into equation 4.1, the 2D inverse scattering series internal multiple prediction algorithm on CMP gathers can be achieved. Its mathematical formulation is written as

$$\begin{aligned} &b_{IM}(p_{m0}, p_{h0}, \omega) = \\ &\frac{-1}{(2\pi)^2} \iiiint_{-\infty}^{+\infty} \mathrm{d}p_{h1}\mathrm{d}p_{h2}\mathrm{d}p_{h3}\mathrm{d}p_{m3} e^{\mathrm{i}\omega(\tau_{1s}-\tau_{1g})} e^{\mathrm{i}\omega(\tau_{1g}-\tau_{1s})} \int_{-\infty}^{+\infty} \mathrm{d}\tau_1 e^{\mathrm{i}\omega\tau_1} b_1(p_{m1}, p_{h1}, \tau_1) \\ &\times \int_{-\infty}^{\tau_1-\epsilon} \mathrm{d}\tau_2 e^{-\mathrm{i}\omega\tau_2} b_1(p_{m2}, p_{h2}, \tau_2) \int_{\tau_2+\epsilon}^{+\infty} \mathrm{d}\tau_3 e^{\mathrm{i}\omega\tau_3} b_1(p_{m3}, p_{h3}, \tau_3), \end{aligned} \tag{4.8}$$

where the relationships of p_{m0}, p_{m1}, p_{m2}, p_{m3}, p_{h0}, p_{h1}, p_{h2}, p_{h3} are delineated as

$$\begin{cases} p_{m2} = p_{h2} + p_{h3} + p_{m3} \\ p_{m1} = p_{h1} + 2p_{h2} + p_{h3} + p_{m3} \\ p_{m0} = p_{h1} + p_{h2} + p_{m3} \\ p_{h0} = p_{h1} + p_{h2} + p_{h3} \end{cases} \tag{4.9}$$

with the input b_1 for inverse scattering series internal multiple prediction algorithm is calculated as $b_1(p_m, p_h, \tau) = -\mathrm{i}2q_s D(p_m, p_h, \tau)$. Here, q_s is the vertical slowness with respect to

source side, which can be obtained as

$$q_s = \sqrt{\frac{1}{c_0^2} - \frac{(p_m - p_h)^2}{4}} \tag{4.10}$$

The implementation of equation 4.8 can be achieved by iterating all possible p_{h1}, p_{h2}, p_{h3}, and p_{m3} while p_{mX} and p_{hX} $(X = 0, 1, 2, 3)$ are in a reasonable range of $[p_m^{min}, p_m^{max}]$ and $[p_h^{min}, p_h^{max}]$, respectively (See the pseudo-code in algorithm 1). Equation 4.8 has the intact capabilities of predicting all possible internal multiples following the same criteria as equation 4.1 does, but, requires the input as a weighted version of data sorted in CMP locations and offsets instead of source-receiver coordinates.

Algorithm 1 Pseudo-code for implementation of equation 4.8

```
for each p_{m3} ∈ [p_m^{min}, p_m^{max}] do
    for each p_{h3} ∈ [p_h^{min}, p_h^{max}] do
        for each p_{h2} ∈ [p_h^{min}, p_h^{max}] do
            for each p_{h1} ∈ [p_h^{min}, p_h^{max}] do
                p_{m2} = p_{h2} + p_{h3} + p_{m3}
                p_{m1} = p_{h1} + 2p_{h2} + p_{h3} + p_{m3}
                p_{m0} = p_{h1} + p_{h2} + p_{m3}
                p_{h0} = p_{h1} + p_{h2} + p_{h3}
                while p_{m2}, p_{m1}, p_{m0} ∈ [p_m^{min}, p_m^{max}] and p_{h0} ∈ [p_h^{min}, p_h^{max}] do
                    Implementing equation 4.8
                end while
            end for
        end for
    end for
end for
```

4.8 Example 2: 2D prediction with 2D algorithm

Next, implementation of the full 2D internal multiple prediction using CMP gathers in coupled plane-wave domain is considered. A benchmark 2D synthetic reflection dataset is created using a fourth-order finite-difference forward modeling with acoustic constant-density and four absorbing boundaries. The velocity model contains three layers and two reflectors, one flat interface and one dipping in 30 degree, as shown in Figure 4.10. From the top to

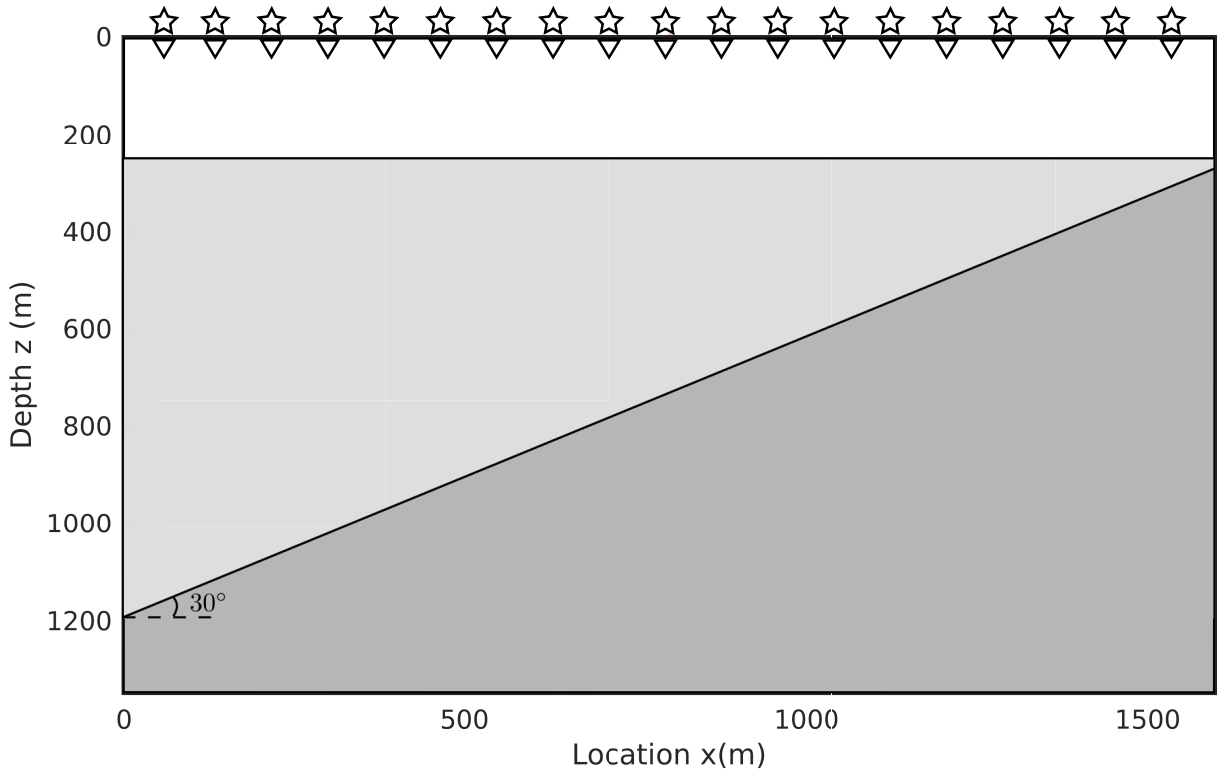

Figure 4.10: Geological model with two interfaces, including one flat and one dipping reflectors. The dipping angle of the second interface is 30°. From the top to bottom, velocities are $[2200m/s, 2800m/s, 4200m/s]$.

bottom, velocities are $[2200m/s, 2800m/s, 4200m/s]$. 160 geophones at 2.5m intervals were embedded at 10m below the surface, and shot records were generated with a 25 Hz Ricker wavelet for source locations moving from left to right and occupying each geophone location. The source-receiver-time volume of multishot records, after removing direct waves, is shown in Figure 4.11.

The multishot records are resorted into CMP domain with CMP-offset-time coordinate and illustrated in Figure 4.12. To observe the 2D character of the data in CMP domain, we extracted three CMP gathers from the resorted CMP volume which are shown in Figure 4.13. As shown in Figure 4.13, two primaries and the first order internal multiple are clearly visible. Similar with the 2D internal multiple prediction in source-receiver coordinate related input, the coupled plane-wave transform is applied to CMP data volume which leads to a 3D volume

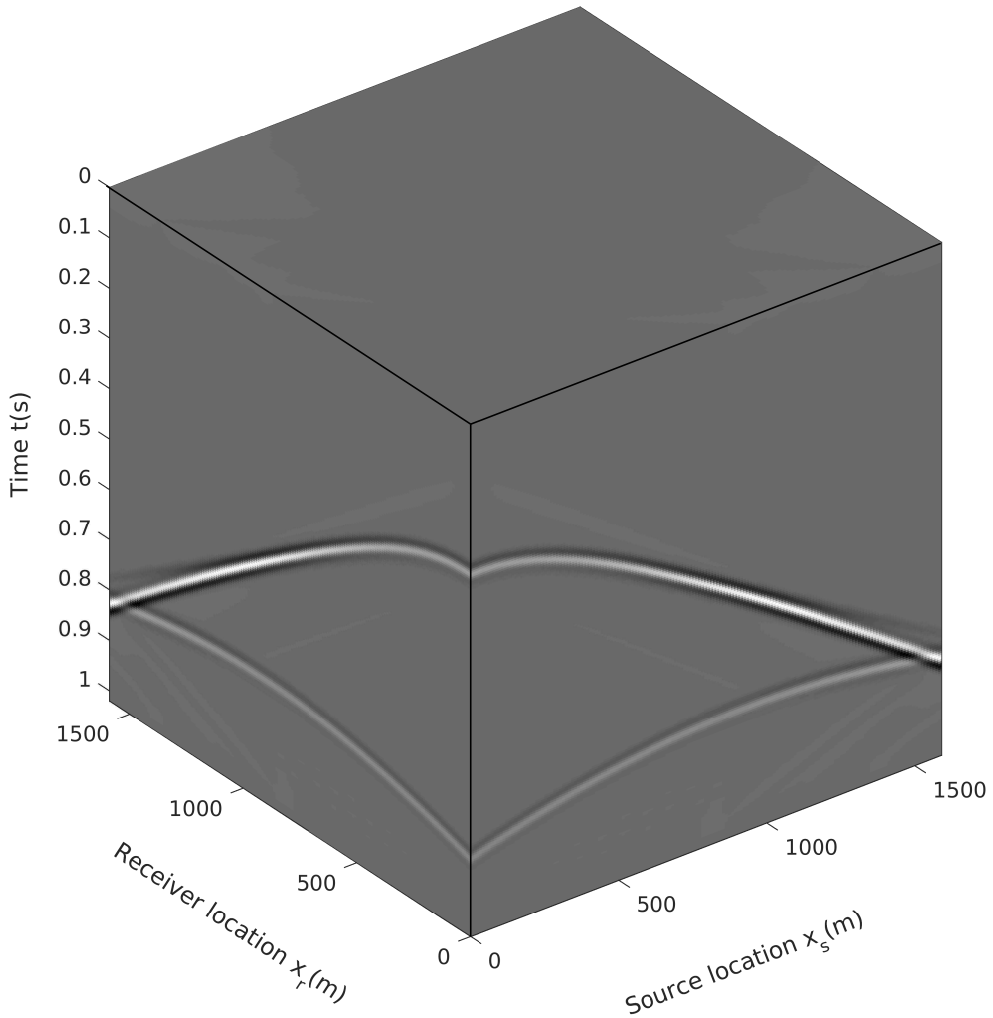

Figure 4.11: Multishot records sorted in source-receiver-time coordinate with velocity model shown in Figure 4.10.

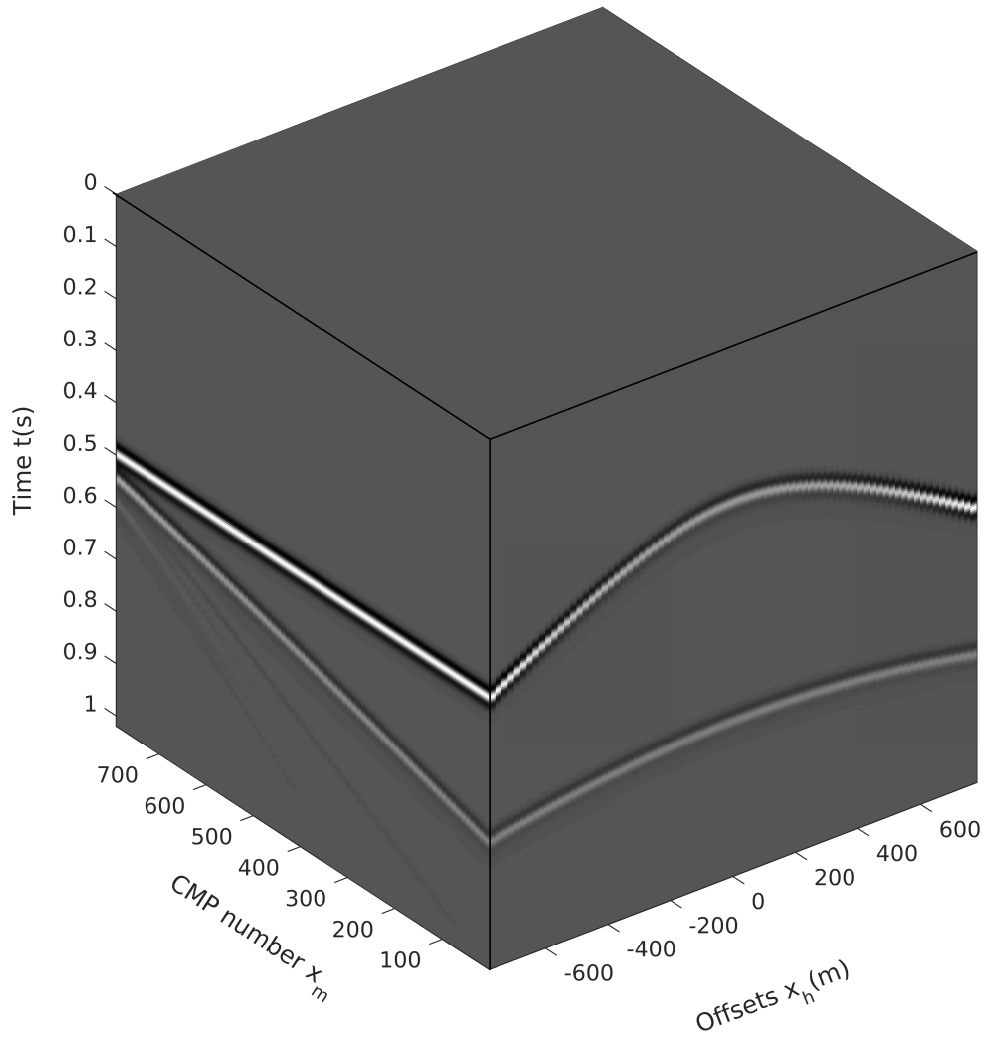

Figure 4.12: Multishot records sorted in CMP-offset-time coordinate.

in horizontal slowness (related to CMP locations and half-offsets) and vertical traveltime. Next, the transformed data volume is weighted by the factor $-\mathrm{i}2q_s$ to generate the final form of the input for the prediction algorithm. Three common p_m gathers extracted from this volume are plotted in Figure 4.14. Compare to the "butterfly" artifacts of the input related to source-receiver coordinates (Sun and Innanen, 2018), the input of internal multiple prediction using CMP gathers has a similar aperture effects delineated as the cross-hyperbolic events in Figure 4.13.

The internal multiple prediction is carried on the transformed input with horizontal slowness related to CMP location and half-offset for all 160 CMP gathers via equation 4.8.

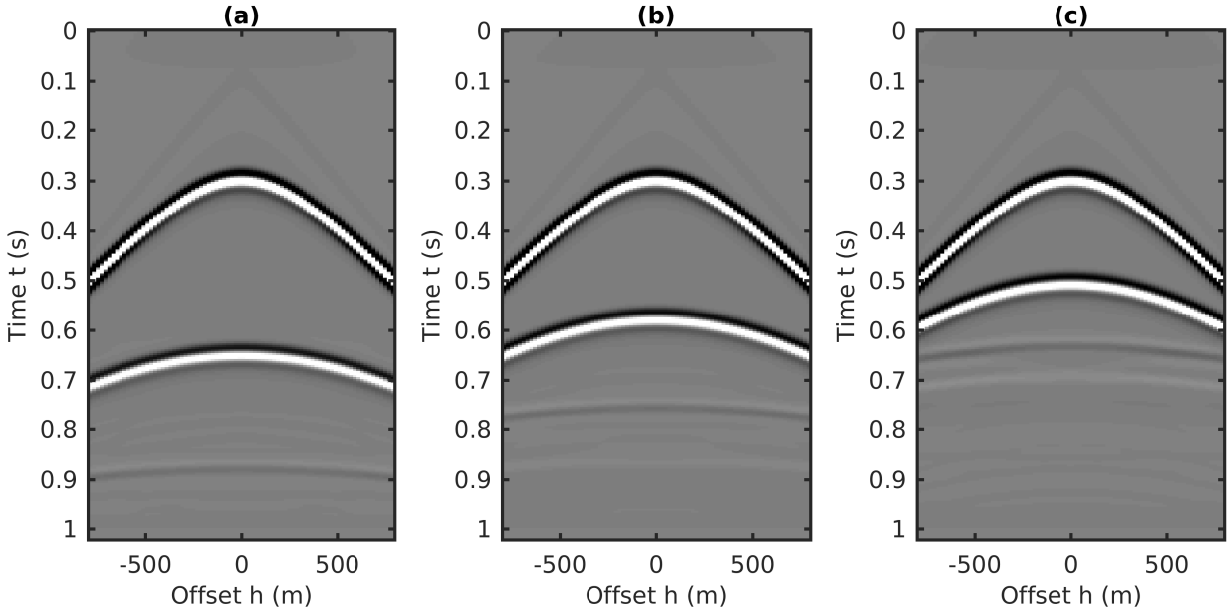

Figure 4.13: Three CMP gathers extracted from volume shown in Figure 4.12. (a) 40th CMP gather. (b) 80th CMP gather. (c) 120th CMP gather.

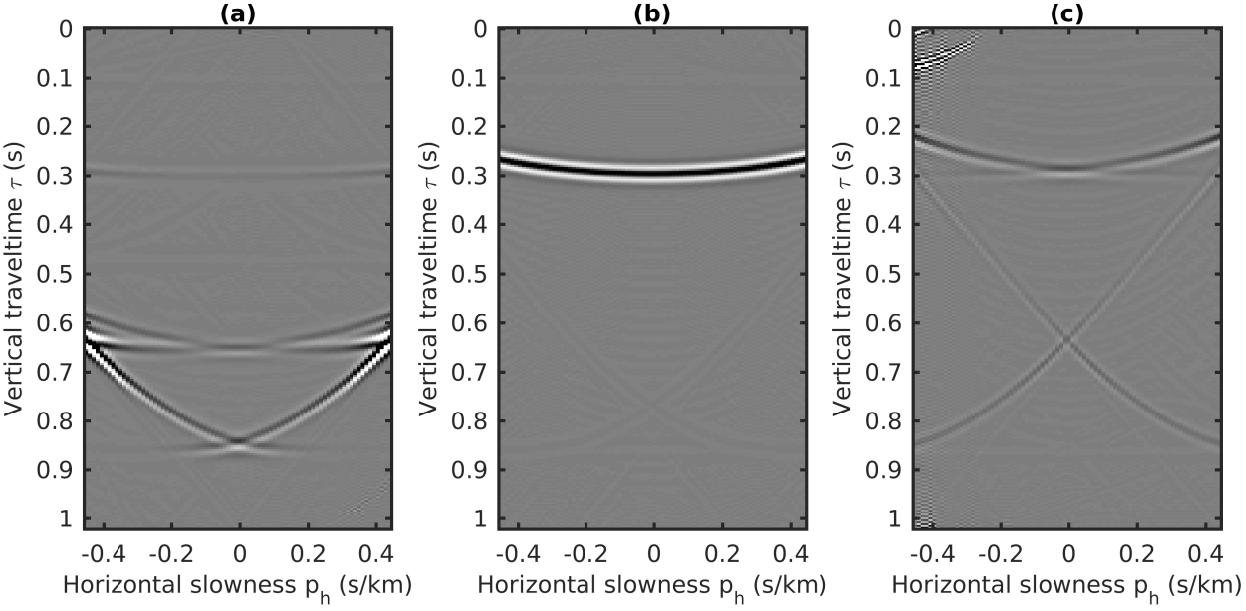

Figure 4.14: Three common p_m gathers extracted from $\tau - p_m - p_h$ transformed CMP volume. (a) $p_m = -0.2s/km$. (b) $p_m = -0s/km$. (c) $p_m = 0.2s/km$.

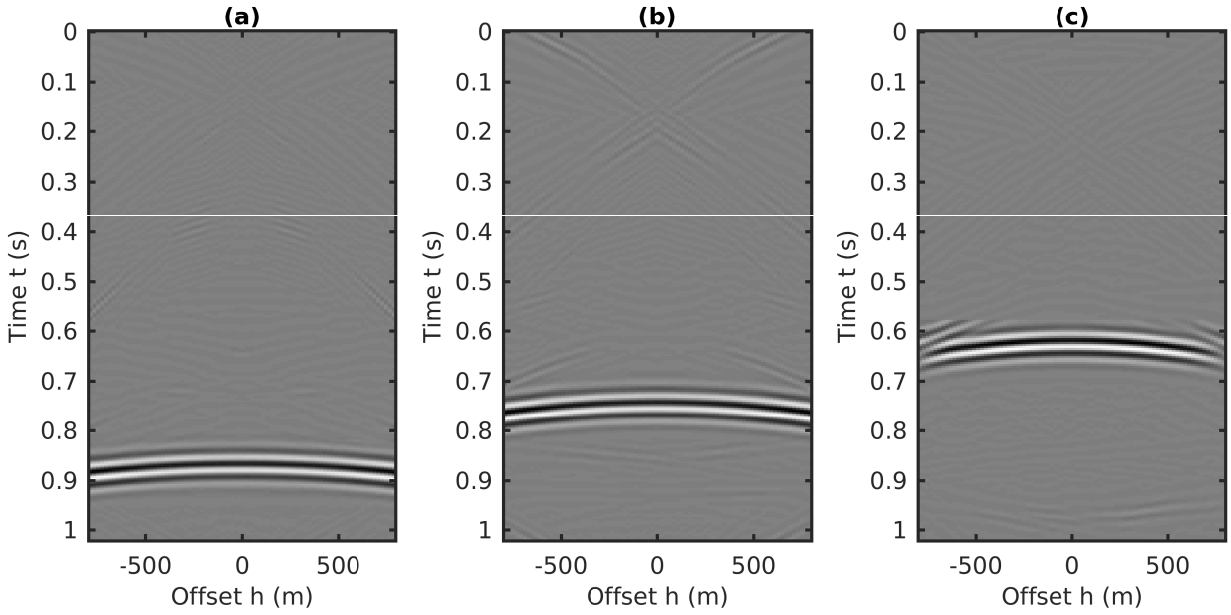

Figure 4.15: Three predicted CMP gathers, which original data are shown in Figure 4.13, using 2D prediction algorithm. (a) 40th CMP gather. (b) 80th CMP gather. (c) 120th CMP gather.

Finally, an inverse coupled plane-wave transformed is applied to achieve the prediction in CMP-offset-time coordinates. Three predicted internal multiples of CMP gathers extracted from the predicted volume (the same CMP locations as those in Figure 4.13) are plotted in Figure 4.15. Comparing Figure 4.13 and Figure 4.15 we conclude that the multidimensional prediction may also be carried out in CMP domain which capture the correct arrival times of all possible internal multiples.

To investigate the behavior of 1.5D prediction algorithm on large dipping strata and compare with 2D prediction algorithm, we also implemented internal multiple prediction using 1.5D algorithm on shot records and CMP gathers, respectively. For these CMP gathers in Figure 4.13, the predicted internal multiples carried via equation 4.3 are plotted in Figure 4.16. As expected in numerical analysis, the internal multiples in three CMP gathers are predicted at incorrect traveltimes with 1.5D prediction algorithm. Next, we extracted three shot gathers from data volume in Figure 4.11, which are at the same locations of CMP in

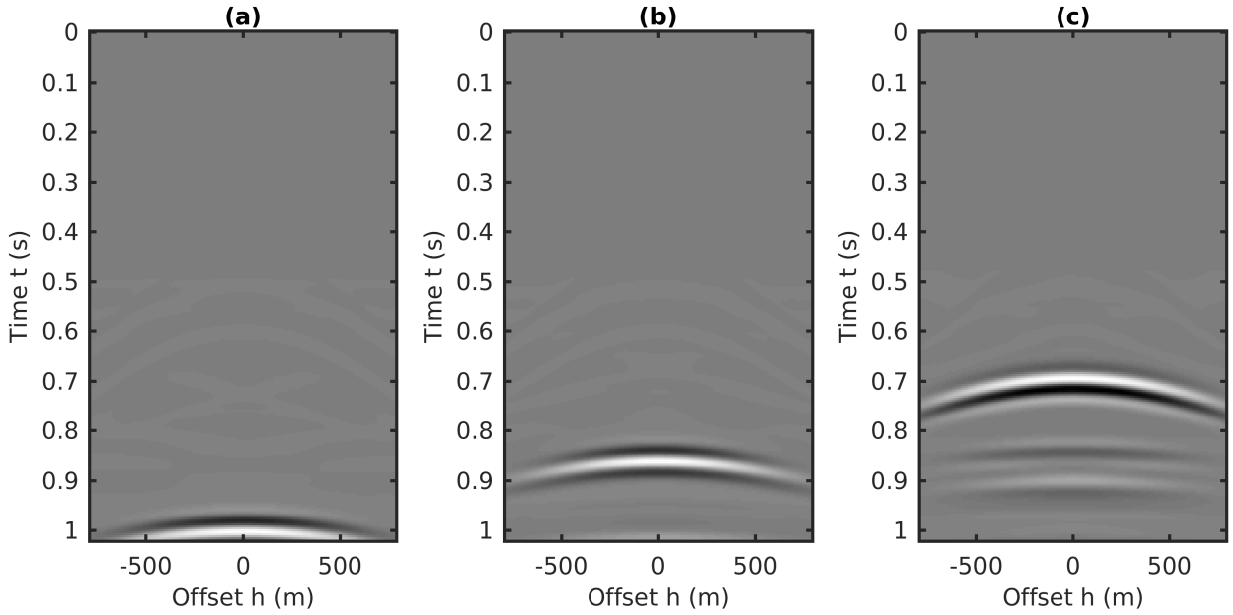

Figure 4.16: Three predicted CMP gathers, which original data are shown in Figure 4.13, using 1.5D prediction algorithm. (a) 40th CMP gather. (b) 80th CMP gather. (c) 120th CMP gather.

Figure 4.13. Extractions of three shot gathers are plotted in Figure 4.17. Using equation 4.3, prediction of internal multiples in shot gathers are illustrated in Figure 4.18. Figure 4.18 indicates that, for large dipping strata, 1.5D prediction algorithm also failed to predict the correct traveltime of internal multiple in sense of shot gather.

4.9 Conclusions

Internal multiples caused by the unknown generators can be predicted by inverse scattering series internal multiple prediction algorithm in an automatic manner, which is usually performed in source-receiver related coordinates. For dipping strata, the algorithm requires many shots for each receiver location, and this significantly enhances the difficulty of input preparation and increases the computational cost. In this chapter, I investigated the behavior of the 1.5D prediction algorithm on dipping cases both for shot and CMP gathers. The numerical analysis of prediction errors indicates that traveltime of internal multiples gener-

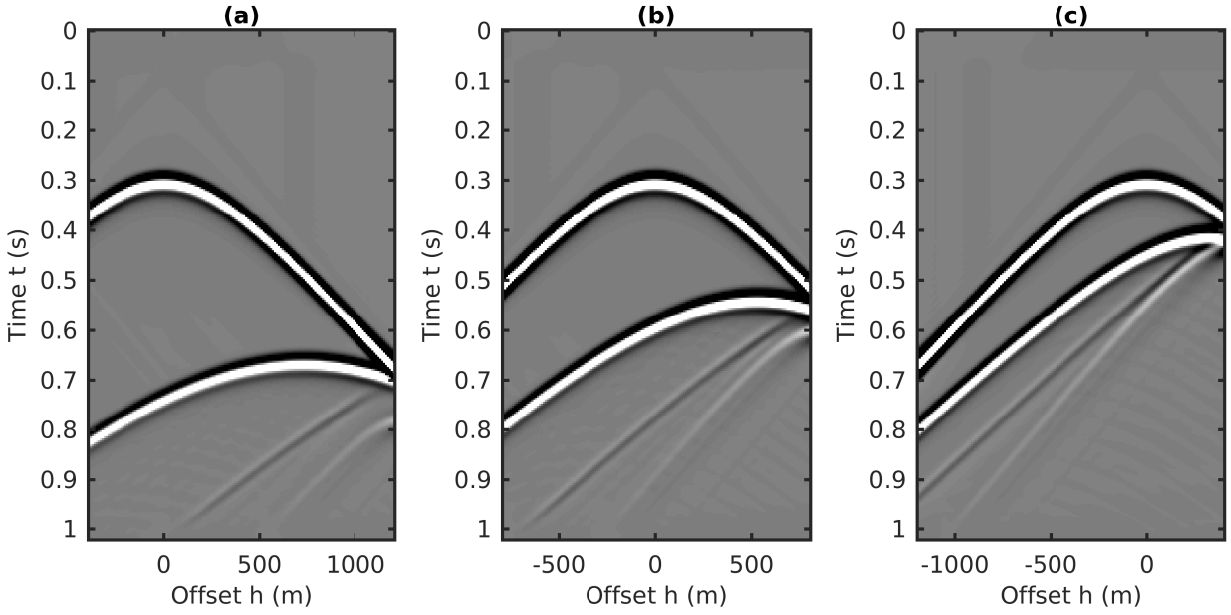

Figure 4.17: Three common shot gathers extracted from data volume in Figure 4.12, where the shot locations are at the same locations of CMP in Figure 4.13. (a) 40th shot gather. (b) 80th shot gather. (c) 120th shot gather.

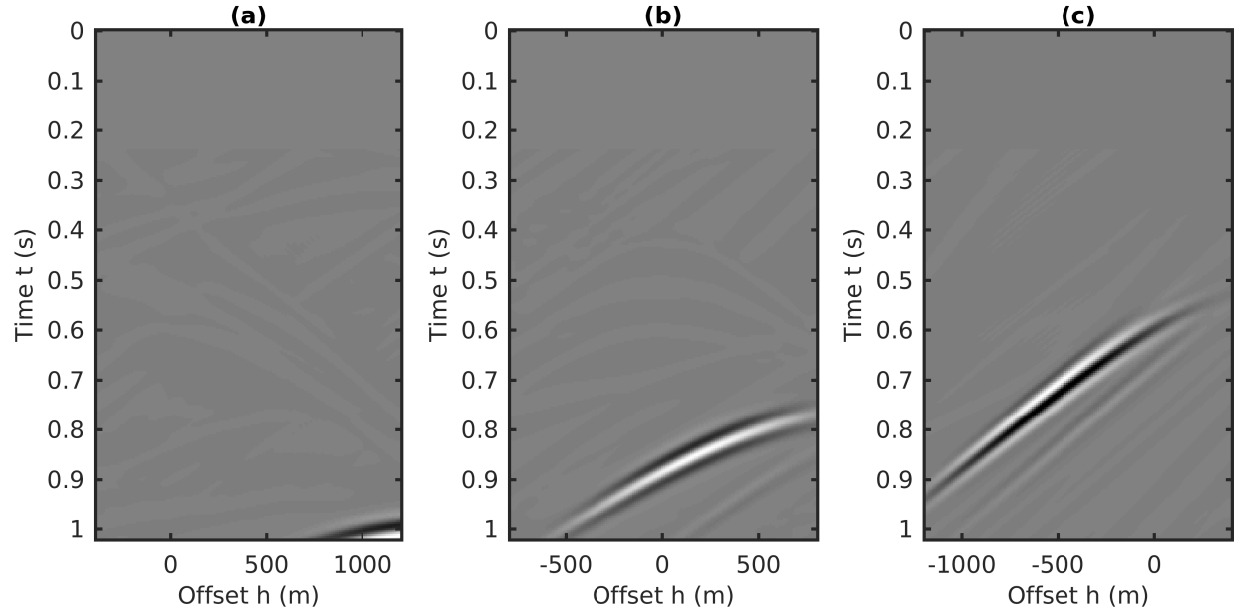

Figure 4.18: Three predicted shot gathers, which original data are shown in Figure 4.13, using 1.5D prediction algorithm. (a) 40th shot gather. (b) 80th shot gather. (c) 120th shot gather.

ated by dipping reflectors with small dipping angles, comparing to shot gather prediction, may be predicted in the CMP domain using 1.5D prediction algorithm with relatively low levels of error. This is then examined on a synthetic dataset. However, 1.5D prediction algorithm will fail to predict the correct traveltime of internal multiples on dipping strata, both in CMP domain and shot/receiver gathers, when the dipping angles of generators reach a threshold value. To carry out 2D prediction on CMP gathers effectively in complex environments, we also proposed a modification of multidimensional inverse scattering series internal multiple prediction algorithm which can be performed on CMP gathers. A simple synthetic benchmark model is created to generate synthetic data and to validate the capacity of the modified prediction algorithm in CMP domain.

Chapter 5

A plane-wave formulation of elastic multicomponent inverse scattering series internal multiple prediction

5.1 Summary

Land environments, which because of the increasing importance of unconventional reservoirs, are of particular importance in general for research in internal multiple prediction and suppression. They present several challenges to the inverse scattering series predictions, including accounting for elastic phenomena and making allowance for multicomponent data. Elastic theory for inverse series internal multiple prediction was introduced several decades ago, but no numerical analysis or practical discussion of how to prepare data for it currently exist. This chapter summarizes efforts to address this gap. I extend the 2D theory to 3D and analyze the properties of the input data as incorporated in the prediction in the existing theory. Also, motivated by earlier research suggesting it has several practical advantages, I simultaneously re-formulate the algorithm in the plane-wave domain. Analysis must then be carried out to understand the ordering of input data events in these domains. In the prediction process, data events which satisfy a certain ordering in either pseudo-depth or vertical travel-time are combined to determine the arrival time of multiples. The success of the approach relies on the ordering of events being the same as the ordering of the reflecting interfaces in true depth. In the elastic case, it is difficult to guarantee that this holds true, because the events to be combined may have undergone multiple conversions as they were created. I introduce several variants of the prediction algorithms and examine them for their tendency to create artifacts from violations of the ordering requirements. A plane-wave domain prediction, based on elastic data which have been prepared (1) using variable, "best-fit"

velocities as reference velocities, and (2) with an analytically determined vertical travel-time stretching formula, is identified as being optimal in the sense of generating artifact-free predictions with relatively small values of the search parameter ϵ. The search parameter limits the proximity of events to be combined in the prediction, and if the user is forced to select a large ϵ, important short-path multiples can be missed in the prediction. These analyses are confirmed with synthetic 1.5D examples, which are to our knowledge the first numerical (i.e., non-analytic) examples of elastic inverse scattering series internal multiple prediction to be presented.

5.2 Introduction

Internal multiple prediction based on the inverse scattering series (Araújo, 1994; Weglein et al., 1997), because it operates in the absence of a detailed velocity model and without generator picking, has been the object of significant theoretical study and practical industrial application (Fu et al., 2010; Wu et al., 2011; Sonika et al., 2012; Ras et al., 2012; de Melo et al., 2014, 2015; Ramirez et al., 2015). In the former, extensions both towards generating exact amplitude predictions, as discussed by (Ramírez and Weglein, 2005) and addressed by (Herrera and Weglein, 2013b) and (Zou and Weglein, 2013), and towards optimizing calculation domains and parameter selection (Innanen, 2017; Sun and Innanen, 2018), have been recently reported.

All practical examples reported in the literature, and all recent extensions, have been carried out within the acoustic approximation. At elastic interfaces, P-waves convert to S-waves (SH- or SV-waves), and vice versa, and the propagation histories of even simple, low-order internal multiples may involve a complex range of mode-conserved and mode-converted interactions. Acoustic prediction, applied in marine environments in which down-going and up-going waves at the measurement surface are purely compressional, can partially account for multiples whose propagation histories below the water-bottom involve S-wave

conversions (Coates et al., 1996). When sensors are embedded in solid media, however, new theory is required. A fully elastic extension of the inverse scattering internal multiple prediction algorithm, given as input multicomponent seismic data acquired during land or ocean-bottom surveys as, has been formulated (Matson, 1997) and tested with fixed-angle analytic data. But, no numerical analysis or examples of the algorithm applied to a seismic gather currently appear in the literature. There are significant challenges in numerically implementing elastic internal multiple prediction, which may partially explain this gap.

Strong motivations exist for developing stable and robust numerical implementations of elastic as opposed to acoustic algorithms. A comprehensive treatment of problematic interbed multiples on land (e.g., Luo et al., 2011; de Melo et al., 2014), for instance, demand such algorithms. Additionally, elastic imaging relies on the availability of multiple estimation based on comparable wave models: absent multiple removal false image structures may be introduced (e.g. Berkhout, 2006; Behura et al., 2014; Zuberi and Alkhalifah, 2014b; Li et al., 2016; Weglein, 2016). Internal multiples have been themselves incorporated in imaging, to provide more stratigraphic information and to illuminate shadow zones where primaries cannot reach (Liu et al., 2011; Malcolm et al., 2009, 2011; Slob et al., 2014). However, even within these approaches, the need to be able to distinguish between primary and multiple events remains, and for elastic imaging this requires elastic prediction. Motivations of this kind have already led to the extension of interferometric formulations of internal multiple prediction (Löer et al., 2016) to versions that admit elastic waves (da Costa Filho et al., 2017).

In current seismic processing technology, data-driven prediction of internal multiple energy from primary events is carried out in one of two distinct ways. The first way involves transforming internal multiples into surface-related multiples, and then predicting them with surface-related methods. This boundary method, which requires layers overlying the generator to be stripped, has been implemented in different domains: post-stack (Kelamis et al.,

2002); common-focal-point (Berkhout and Verschuur, 2005; Berkhout, 2006); and inverse-data domain (Luo et al., 2007). The second way is based on the inverse scattering series, and involves predicting internal multiples as the combination of triplets of data sub-events combined based on their relative vertical travel-times (Weglein et al., 1997; Nita and Weglein, 2009a). Which precise events are combined is dictated by vertical travel-time ordering: when three events satisfy what is referred to as *lower-higher-lower* criterion (Weglein et al., 1997), they are combined. The criterion is refined by the parameter ϵ (Coates et al., 1996; Innanen, 2017), which accounts for the finite vertical extent (in time or pseudo-depth) of the contributing sub-events.

The domain in which internal multiple predictions are calculated can have a major impact on the fidelity of the result, because the vertical extent of sub-events, which drives the selection of ϵ, can be simple in one domain and complex in another. In the standard form of the algorithm, in which calculations occur in the wavenumber / pseudo-depth domain, it has been pointed out that a constant ϵ will tend to lead to high-angle artifacts in the prediction (Innanen and Pan, 2015); this and any other non-stationarity can be mitigated by incorporating varable ϵ values. However, (Sun and Innanen, 2018) point out that sub-events in a plane-wave formulation appear to be almost entirely stationary in their vertical τ extent as the ray-parameter p varies. Empirically the plane wave domain appears to be the least susceptible to large-angle artifacts.

These factors motivate us to implement and analyze elastic inverse scattering internal multiple prediction, and to do so with a plane-wave (τ-p) formulation. In doing so I extend the theory for elastic prediction from 2D to 3D, and then present the first numerical examples of fully elastic internal multiple prediction on synthetic seismic records beyond the quasi-analytic single-trace examples of (Matson, 1997). A number of practical issues must be addressed for this to happen. Wave-mode conversions in seismic records have an effect on the ease with which the lower-higher-lower criterion can be applied, making, amongst

other things, data pre-processing and preparation more complex. How to formulate elastic prediction without the possibility of introducing artifacts from lower-higher-lower rule violations originating from converted-waves remains unknown (Sun and Innanen, 2017; Sun et al., 2018a,b). However, relatively clean and well-formed predictions are possible as we shall demonstrate, after examination of several possible approaches for multicomponent input data preparation.

5.3 Multicomponent internal multiple prediction in three dimensions

To derive elastic multiple attenuation given multicomponent data, Matson (1997) decomposed the inverse scattering series into components related to the P- and SV-wave potentials and adopting an isotropic-elastic-homogeneous background model. Here, I extend this prediction algorithm into three dimensions and include the SH mode. Let $d^{ij}(x_g, x_s, y_g, y_s, t)$ represent a 3D seismic record involving a downgoing wave-mode j from the source and an upgoing wave-mode i to the receiver, with x_g and x_s being inline receiver and source coordinates, y_g and y_s being crossline receiver and source coordinates, and t being the time. Let $D^{ij}(k^i_{x_g}, k^i_{y_g}, k^j_{x_s}, k^j_{y_s}, \omega)$ represent the data set Fourier transformed over source/receiver coordinates and time, with $k^j_{x_s}$ and $k^j_{y_s}$ being the x- and y-components of wavenumber conjugate to the source coordinate generating the jth mode, and $k^i_{x_g}$ and $k^i_{y_g}$ being the x- and y-components of wavenumber conjugate to the receiver coordinate sensing the ith mode, and with ω being the angular frequency. The 3D algorithm for elastic internal multiple prediction

is

$$
\begin{aligned}
&b_3^{ij}(k_{x_g}^i, k_{y_g}^i, k_{x_s}^j, k_{y_s}^j, \omega) \\
&= -\frac{1}{(2\pi)^4} \iiiint_{-\infty}^{+\infty} \mathrm{d}k_{x_1}^m \mathrm{d}k_{y_1}^m \mathrm{d}k_{x_2}^n \mathrm{d}k_{y_2}^n e^{\mathrm{i}\nu_1^m(\tilde{z}_s - \tilde{z}_g)} e^{-\mathrm{i}\nu_2^n(\tilde{z}_s - \tilde{z}_g)} \\
&\qquad \times \int_{-\infty}^{+\infty} \mathrm{d}\tilde{z}_1 e^{\mathrm{i}(\nu_1^m + \nu_g^i)\tilde{z}_1} b_1^{im}(k_{x_g}^i, k_{y_g}^i, k_{x_1}^m, k_{y_1}^m, \tilde{z}_1) \\
&\qquad \times \int_{-\infty}^{\tilde{z}_1 - \epsilon} \mathrm{d}\tilde{z}_2 e^{-\mathrm{i}(\nu_2^n + \nu_1^m)\tilde{z}_2} b_1^{mn}(k_{x_1}^m, k_{y_1}^m, k_{x_2}^n, k_{y_2}^n, \tilde{z}_2) \\
&\qquad \times \int_{\tilde{z}_2 + \epsilon}^{+\infty} \mathrm{d}\tilde{z}_3 e^{\mathrm{i}(\nu_s^j + \nu_2^n)\tilde{z}_2} b_1^{nj}(k_{x_2}^n, k_{y_2}^n, k_{x_s}^j, k_{y_s}^j, \tilde{z}_3),
\end{aligned}
\tag{5.1}
$$

where

$$
\nu_M^I = \sqrt{\frac{\omega^2}{(c_0^I)^2} - (k_{x_M}^I)^2 - (k_{y_M}^I)^2}
\tag{5.2}
$$

is the vertical component of wavenumber associated with the x- and y- components of wavenumber $k_{x_M}^I$ and $k_{y_M}^I$, and with the isotropic-elastic homogeneous reference velocity c_0^I of the wave-mode $I \in \{P, SH, SV\}$, and the source/receiver location $M \in \{g, s\}$. The integration variables $\tilde{z}_1, \tilde{z}_2, \tilde{z}_3$, following standard internal multiple theory, are in units of pseudo-depth. The pseudo-depth integral limits enact the lower-higher-lower relationship, i.e., $\tilde{z}_1 > \tilde{z}_2$ and $\tilde{z}_2 < \tilde{z}_3$. After an inverse Fourier transform over the source and receiver lateral wavenumbers and frequency, the left hand side of equation 5.1 becomes the $j \to i$ mode internal multiple prediction in the (x_g, y_g, x_s, y_s, t) domain. The transformed estimates are then added to the mode-decomposed seismic records to attenuate multiples; normally this also requires an adaptive subtraction step to manage amplitude mismatches.

The input b_1^{ij} is a mode-decomposed and weighted form of the measured seismic record related to the jth downgoing and ith updoing wave mode:

$$
b_1^{ij}(k_{x_g}^i, k_{y_g}^i, k_{x_s}^j, k_{y_s}^j, \tilde{z}) = -\mathrm{i}2\nu_s^j D^{ij}(k_{x_g}^i, k_{y_g}^i, k_{x_s}^j, k_{y_s}^j, \tilde{z}),
\tag{5.3}
$$

where $D^{ij}(k_{x_g}^i, k_{y_g}^i, k_{x_s}^j, k_{y_s}^j, \tilde{z})$ are the transformed data in the pseudo-depth domain. Pseudo-depth is a nonlinear scaled version of vertical traveltime related to raypath, and as such the pseudo-depth of a reflected seismic event is in general very different from the actual depth at which the reflection occurs; for the internal multiple algorithm to work properly

requires only that the *ordering* of reflections in pseudo-depth to be the same as in actual depth. Understanding the degree to which this holds outside of a purely compressional wave (acoustic) environment is one of the aims of our research.

5.4 Plane-wave domain formulation

The acoustic internal multiple prediction algorithm operates assuming that the ordering of data events in pseudo-depth and/or vertical traveltime must be the same as that of the interfaces in depth (e.g., Nita and Weglein, 2009a). Because the propagation legs of an internal multiple in a solid medium can involve a complex series of mode-conserved and mode-converted interactions, the elastic requirements are less straightforward. In order for a plane-wave domain prediction algorithm to be formulated, I must examine the pseudo-depth and/or vertical traveltime in some detail. Suppose three reflection ray-paths interact with

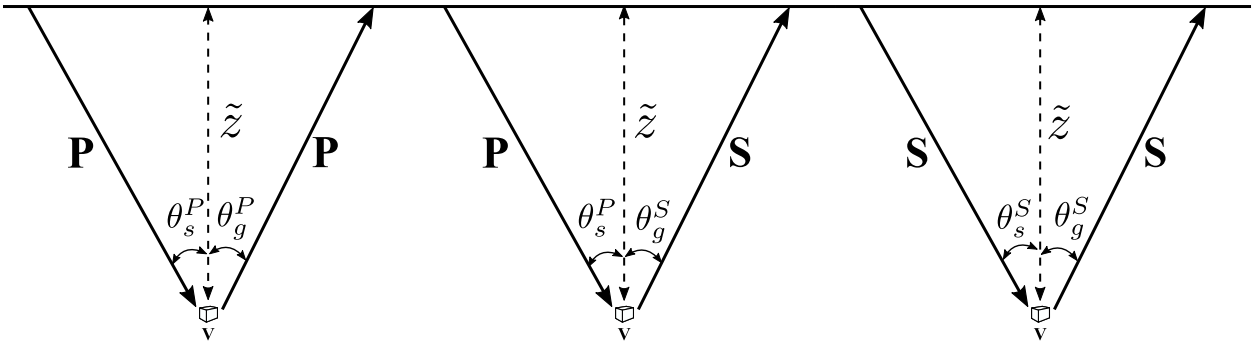

Figure 5.1: Ray-paths of PP-, PS- and SS-waves propagating in a reference medium through one perturbation only. $\tilde{z}$ is the pseudo-depth.

the same scattering point perturbing a homogeneous isotropic-elastic (reference) medium (Figure 5.1). The depths of these three primary reflection points would be assigned the same pseudo-depth (during, say, the process of input data preparation for the multiple algorithm), but different vertical traveltimes. This means integral limits for vertical traveltimes will have to be selected with some care. What we will refer to as the *pseudo*-vertical traveltimes, i.e., vertical traveltimes associated with propagation at reference medium velocities, of these

three reflections can be written in terms of pseudo-depth as

$$\tilde{\tau}^{PP} = \tilde{\tau}_s^P + \tilde{\tau}_g^P = \left(q_s^P + q_g^P\right)\tilde{z} \tag{5.4a}$$

$$\tilde{\tau}^{SP} = \tilde{\tau}_s^P + \tilde{\tau}_g^S = \left(q_s^P + q_g^S\right)\tilde{z} \tag{5.4b}$$

$$\tilde{\tau}^{SS} = \tilde{\tau}_s^S + \tilde{\tau}_g^S = \left(q_s^S + q_g^S\right)\tilde{z}, \tag{5.4c}$$

where $\tilde{\tau}_s^I$ is the pseudo-vertical traveltime of the down-going wave in the reference medium, and $\tilde{\tau}_g^I$ is the pseudo-vertical traveltime of the up-going wave in the reference medium, for the associated wave-type $I \in \{P, SH, SV\}$, $\tilde{z}$ is the pseudo-depth of the scattering perturbation point, and q_M^I is the vertical component of slowness, with the superscript indicating wave type, and the subscript indicating the source/receiver dependency:

$$q_M^I = \sqrt{\frac{1}{(c_0^I)^2} - (p_{xM}^I)^2 - (p_{yM}^I)^2}. \tag{5.5}$$

Here c_0^I represents the P- and S-wave reference medium velocities as needed, i.e., $c_0^P = \alpha$, and $c_0^S = \beta$. The quantities p_{xM}^I and p_{yM}^I are the horizontal slownesses for each wave type and source versus receiver. Balanced expressions for the pseudo-vertical traveltimes of three reflections scattered at identical pseudo-depths are therefore

$$\frac{\tilde{\tau}^{PP}}{q_s^P + q_g^P} = \frac{\tilde{\tau}^{SP}}{q_s^P + q_g^S} = \frac{\tilde{\tau}^{SS}}{q_s^S + q_g^S}. \tag{5.6}$$

By switching from wavenumber to horizontal slowness and substituting equation 5.6 into equation 5.1, I obtain the plane-wave domain multicomponent internal multiple prediction formula:

$$\begin{aligned}
&b_3^{ij}(p_{x_g}^i, p_{y_g}^i, p_{x_s}^j, p_{y_s}^j, \omega) \\
&= -\frac{1}{(2\pi)^4}\iiiint_{-\infty}^{+\infty} \mathrm{d}p_{x_1}^m \mathrm{d}p_{y_1}^m \mathrm{d}p_{x_2}^n \mathrm{d}p_{y_2}^n e^{\mathrm{i}\omega(\tilde{\tau}_{1s}^m - \tilde{\tau}_{1g}^m)} e^{-\mathrm{i}\omega(\tilde{\tau}_{2s}^n - \tilde{\tau}_{2g}^n)} \\
&\qquad \times \int_{-\infty}^{+\infty} \mathrm{d}\tilde{\tau}_1^{im} e^{\mathrm{i}\omega\tilde{\tau}_1^{im}} b_1^{im}(p_{x_g}^i, p_{y_g}^i, p_{x_1}^m, p_{y_1}^m, \tilde{\tau}_1^{im}) \\
&\qquad \times \int_{-\infty}^{\Upsilon(\tilde{\tau}_2^{mn}|\tilde{\tau}_1^{im})-\epsilon} \mathrm{d}\tilde{\tau}_2^{mn} e^{-\mathrm{i}\omega\tilde{\tau}_2^{mn}} b_1^{mn}(p_{x_1}^m, p_{y_1}^m, p_{x_2}^n, p_{y_2}^n, \tilde{\tau}_2^{mn}) \\
&\qquad \times \int_{\Upsilon(\tilde{\tau}_3^{nj}|\tilde{\tau}_2^{mn})+\epsilon}^{+\infty} \mathrm{d}\tilde{\tau}_3^{nj} e^{\mathrm{i}\omega\tilde{\tau}_3^{nj}} b_1^{nj}(p_{x_2}^n, p_{y_2}^n, p_{x_s}^j, p_{y_s}^j, \tilde{\tau}_3^{nj}),
\end{aligned} \tag{5.7}$$

where

$$\Upsilon(\tilde{\tau}_2^{mn}|\tilde{\tau}_1^{im}) = \frac{q_s^n + q_g^m}{q_s^i + q_g^m}\tilde{\tau}_1^{im}, \tag{5.8}$$

and where p_x^I and p_y^I are the x- and y- components of slowness for wave type I.

The pseudo-vertical traveltime $\tilde{\tau}$ is the vertical component of traveltime in the reference medium, which in elastic media is generally distinct from the vertical travel-time τ in the actual medium (for acoustic cases, $\tilde{\tau} \equiv \tau$). For example, two primary events, $\grave{P}\grave{P}\acute{P}\acute{P}$ and $\grave{P}\grave{S}\acute{P}\acute{P}$ (where accents represent downgoing ($\grave{X}$) and upgoing ($\acute{X}$) waves respectively), reflected at the same depth, must have different vertical travel-times τ in the actual seismic record. In contrast, the algorithm proceeds assuming the pseudo-depths of these two reflections are the same, because of the monotonicity condition between actual depth and pseudo-depth. In reference medium, it leads to the equivalent pseudo-vertical traveltimes $\tilde{\tau}$ (based on equation 5.4a) because both of two reflections are recorded in P-component.

5.5 Elastic vertical traveltime monotonicity

Preparation of the input data is critical to the proper prediction of elastic internal multiples, either in the wavenumber-pseudodepth domain (equation 5.1), hereafter k-z, or the plane-wave domain, hereafter τ-p (equation 5.7). By applying the algorithm I make the assumption that the ordering of events in the relevant domain, pseudo-depth or pseudo-vertical traveltime, is the same as the ordering in depth of the interfaces causing the primary reflections; equivalently stated, the pseudo-vertical traveltime and pseudo-depth are monotonic functions of true depth. In the elastic case I face the added complexity that, over the propagation path of a single event, velocity variations can occur in the same layer due to wave-mode conversion. This can affect prediction outcomes if care is not taken during data preparation. In this section, I introduce several possible approaches to data preparation and analyze them in the context of the various monotonicity assumptions.

5.5.1 Pre-stack elastic Stolt migration

Matson (1997) derives input for the k-z domain prediction by performing a pre-stack elastic Stolt migration with a constant reference velocity for each of the P- and SV-waves. I begin with a brief review of this approach in order to develop a clear sense of the pseudo-depths it determines. I will refer to the pre-stack Stolt migration pseudo-depths as Stolt-depths, and distinguish between these depths and the $\tilde{z}$ in equation 5.1. The pre-stack Stolt-migration scheme involves Fourier transforming the surface data, re-gridding ω to $\omega(k_z)$, and inverse Fourier transforming to depth (Stolt, 1978). Pre-stack elastic Stolt-migration formulas for P-P and P-SV images were obtained by Etgen (1988):

$$R_{PP}(k_m, z) = \int \mathrm{d}k_h \int \mathrm{d}k_z^P \left| \frac{\mathrm{d}\omega}{\mathrm{d}k_z^P} \right| P(k_m, k_h, \omega(k_z^P)) e^{ik_z^P z} \tag{5.9a}$$

$$R_{SVP}(k_m, z) = \int \mathrm{d}k_h \int \mathrm{d}k_z^{SV} \left| \frac{\mathrm{d}\omega}{\mathrm{d}k_z^{SV}} \right| P(k_m, k_h, \omega(k_z^{SV})) e^{ik_z^{SV} z}, \tag{5.9b}$$

where k_z^P is determined by the P-wave dispersion relation:

$$k_z^P = \frac{\omega}{\alpha} \left(\sqrt{1 - \frac{\alpha^2 k_s^2}{\omega^2}} + \sqrt{1 - \frac{\alpha^2 k_g^2}{\omega^2}} \right), \tag{5.10}$$

and k_z^{SV} is determined from the SV-wave dispersion relation:

$$k_z^{SV} = \frac{\omega}{\alpha} \sqrt{1 - \frac{\alpha^2 k_s^2}{\omega^2}} + \frac{\omega}{\beta} \sqrt{1 - \frac{\beta^2 k_g^2}{\omega^2}}, \tag{5.11}$$

and where k_m, k_h are the wavenumbers conjugate to the mid-point and offset coordinates, and k_s, k_g are the horizontal components of the wavenumbers conjugate to the source and receiver coordinates. They are related by

$$k_s = \frac{k_m - k_h}{2}, \tag{5.12a}$$

$$k_g = \frac{k_m + k_h}{2}. \tag{5.12b}$$

As suggested by equation 5.9, the first step of pre-stack elastic Stolt-migration is to interpolate the angular frequencies on the ω-axis onto a regular grid of vertical wavenumber k_z

values for both P- and SV-components. The re-gridding requires ω to be evaluated as a function of k_z. For PP data, $\omega(k_z^P)$ and its Jacobian expression $\left|\frac{\mathrm{d}\omega}{\mathrm{d}k_z^P}\right|$ was introduced by van Trier (1985). Etgen (1988) presented the P-SV extension, i.e., the formulas for $\omega(k_z^{SV})$ and the Jacobian $\left|\frac{\mathrm{d}\omega}{\mathrm{d}k_z^{SV}}\right|$.

5.5.2 Stolt depths and the plane-wave transform

Stolt migration can be understood as reconstructing the reference medium propagation path and reflection points which match the seismic data. For example, a wave scattering from four perturbations at various lateral x and vertical z positions, illustrated in Figure 5.2a, is interpreted in terms of the single interaction and propagation in the reference medium with constant background velocities illustrated in Figure 5.2b. The raypaths generate equal

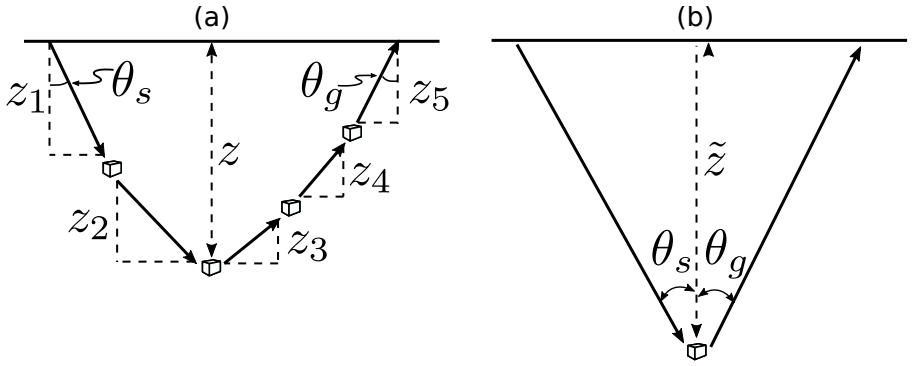

Figure 5.2: The commons and differences of wave propagation path in actual and reference medium. (a) Ray-path in actual medium with offset: x, horizontal slowness: p_s and p_g, and reflection depth: z; (b) Ray-path in the reference medium with offset: x, horizontal slowness: p_s and p_g, reflection depth: $\tilde{z}$.

vertical traveltimes, therefore I have

$$\tau^{mn} = \sum_{i=1}^{N} q_i^{w_i} z_i = (q_s^n + q_g^m)\tilde{z}_{stolt}, \tag{5.13}$$

where τ^{mn} is the actual vertical traveltime with incident wave-type n and received wave-type m, $m, n \in \{P, SH, SV\}$, $q_i^{w_i}$ is the vertical slowness for each segment of ray-path with associated wave type w_i, N is the number of raypath segments, z_i is the vertical component of each raypath segment, and $\tilde{z}_{stolt}$ is the Stolt-depth in the reference medium.

Equation 5.13 is suggestive that implementing internal multiple prediction with the input created by elastic Stolt-migration in the pseudo-depth domain (equation 5.1) will be essentially equivalent to predictions generated using equation 5.7 with input generated through the plane-wave transform (as discussed by Sun and Innanen, 2018), provided the vertical travel-time stretching described by equation 5.8 is invoked to accommodate wave conversion. However, both elastic Stolt migration and plane-wave with time-stretching approaches allow only for single wave-mode conversions at the reflection point. Both may produce inappropriate inputs ($\tilde{z} \neq \tilde{z}_{stolt}, \tilde{\tau} \neq \tau$) if wave-mode conversions occur at transmission points in the real path of the wave. This is particularly problematic in the layered medium approximation (i.e., the 1.5D case), wherein source and receiver have identical horizontal slownesses, i.e., $p_s = p_g$.

5.5.3 Data preparation based on the high-resolution Radon transform

Sub-event ordering within the input to internal multiple prediction is a more complex issue for solid media than it is in the acoustic approximation. In 1.5D, stacking velocities can be effective guides to proper input data preparation. Each event in the input data in the offset-time domain has an associated velocity v_b, with a value decided such that its arrival times best fit with

$$t^2 = t_0^2 + \frac{x^2}{v_b^2}, \tag{5.14}$$

where x is offset. The v_b for each reflection can be calculated by hyperbolic Radon transform (Trad et al., 2002):

$$m(\tau_0, v_b) = \int_{x_{min}}^{x_{max}} d\left(t = \sqrt{\tau_0^2 + x^2/v_b^2}, x\right) \mathrm{d}x, \tag{5.15}$$

where $m(\tau_0, v_b)$ are the data in Radon space, τ_0 is the two-way zero-offset travel time, i.e., the time axis in hyperbolic Radon space, $d(t, x)$ is the data in offset-time domain. High resolution Radon methods treat this transform as an inverse problem, solved with an iterative re-weighted least squares algorithm. The best-fitting velocity model as retrieved in the

hyperbolic Radon space can be transferred into input data space using elliptical Radon transform:

$$\hat{d}(\tau,p)=\int_{v_{min}}^{v_{max}} m\left(\tau_0=\frac{\tau}{\sqrt{1-p^2v_b^2}},v_b\right)\mathrm{d}v_b, \tag{5.16}$$

where p is the horizontal slowness; τ is the vertical travel time, i.e., the time axis in linear Radon space, and v_b is the best-fitting velocity for hyperbolic events. The relationship between the vertical travel-time and the pseudo-depth using the best-fitting velocity model $\tilde{z}_b$ can be written as

$$\tau^{mn}=(\tilde{q}_s^n+\tilde{q}_g^m)\tilde{z}_b, \tag{5.17}$$

with what I will refer to as the pseudo-vertical slowness on the source side being

$$\tilde{q}_s^n=\sqrt{\frac{1}{(v_b^{mn})^2}-(p_s^n)^2}, \tag{5.18}$$

and likewise the pseudo-vertical slowness on the receiver side being

$$\tilde{q}_g^m=\sqrt{\frac{1}{(v_b^{mn})^2}-(p_g^m)^2}. \tag{5.19}$$

The elastic internal multiple prediction algorithm in the plane-wave domain can be reformulated in terms of these best-fit stacking velocity τ quantities as

$$\begin{aligned} b_3^{ij}(p_g^i,p_s^j,\omega)=-\frac{1}{(2\pi)^2}\iint_{-\infty}^{+\infty}\mathrm{d}p_1^m\mathrm{d}p_2^n e^{\mathrm{i}\omega(\tau_{1s}^m-\tau_{1g}^m)}e^{-\mathrm{i}\omega(\tau_{2s}^n-\tau_{2g}^n)} \\ \times\int_{-\infty}^{+\infty}\mathrm{d}\tau_1^{im}e^{\mathrm{i}\omega\tau_1^{im}}b_1^{im}(p_g^i,p_1^m,\tau_1^{im}) \\ \times\int_{-\infty}^{\Gamma(\tau_2^{mn}|\tau_1^{im})-\epsilon}\mathrm{d}\tau_2^{mn}e^{-\mathrm{i}\omega\tau_2^{mn}}b_1^{mn}(p_1^m,p_2^n,\tau_2^{mn}) \\ \times\int_{\Gamma(\tau_3^{nj}|\tau_2^{mn})+\epsilon}^{+\infty}\mathrm{d}\tau_3^{nj}e^{\mathrm{i}\omega\tau_3^{nj}}b_1^{nj}(p_2^n,p_s^j,\tau_3^{nj}), \end{aligned} \tag{5.20}$$

with

$$\Gamma(\tau_2^{mn}|\tau_1^{im})=\frac{\tilde{q}_s^n+\tilde{q}_g^m}{\tilde{q}_s^i+\tilde{q}_g^m}\tau_1^{im}. \tag{5.21}$$

The input is $b_1^{ij}(p_g^i,p_s^j,\tau)=-i2q_sD^{ij}(p_g^i,p_s^j,\tau)$; the weight q_s is the same as that in equation 5.5. $D^{ij}(p_g^i,p_s^j,\tau)$ is the coupled plane wave transformation of the data set in its original source-receiver-time coordinate system.

5.5.4 Analysis of the altered plane-wave algorithm

I stated above that, in the layered-medium approximation, a τ-p input based on stacking velocities goes some distance towards generating input which is less sensitive to complex conversion histories within sub-events. This statement requires some justification. Consider a P-wave incident on a two-interface elastic-isotropic layered medium. The ray-paths of all primary reflections (neglecting Snell's law) are illustrated in Figure 5.3. Consider further the analytically-calculated vertical traveltimes of these events from the two interfaces, which are plotted in Figures 5.4a and 5.4d. Because of wave-mode conversion, the vertical traveltimes of primary events reflected from the same interfaces are significantly separated. Appropriate input preparation would re-map reflections from one interface into the same pseudo-depth—or, at any rate, proximal pseudo-depths, ones which are within one ϵ of each other.

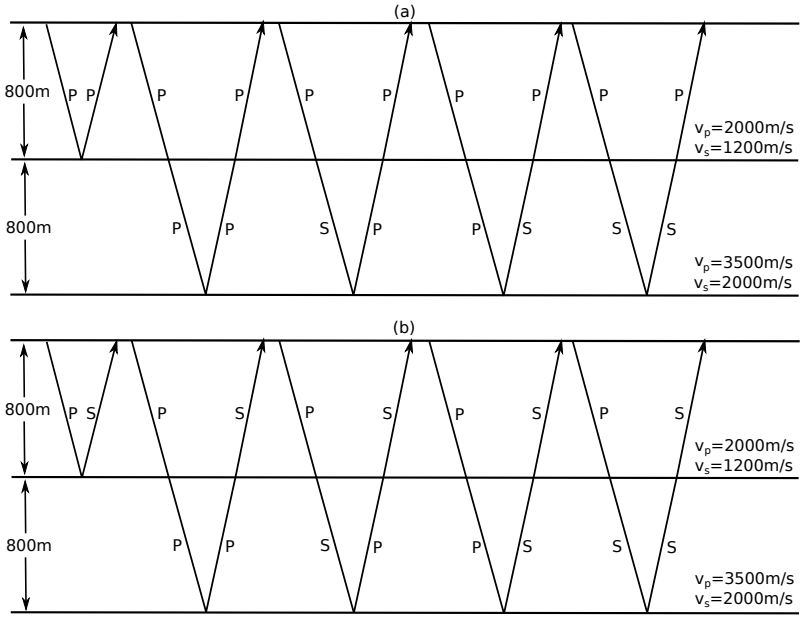

Figure 5.3: Ray paths of all primary events in multicomponent reflected by the two interfaces. (a) P-P component. (b) P-SV component.

The Stolt-depths of the reflections, obtained using equation 5.13, are plotted in Figures 5.4b and 5.4e. In Figure 5.4b the two primaries reflected by the first interface are re-mapped to the same pseudo-depth using prestack elastic Stolt-migration. However, the

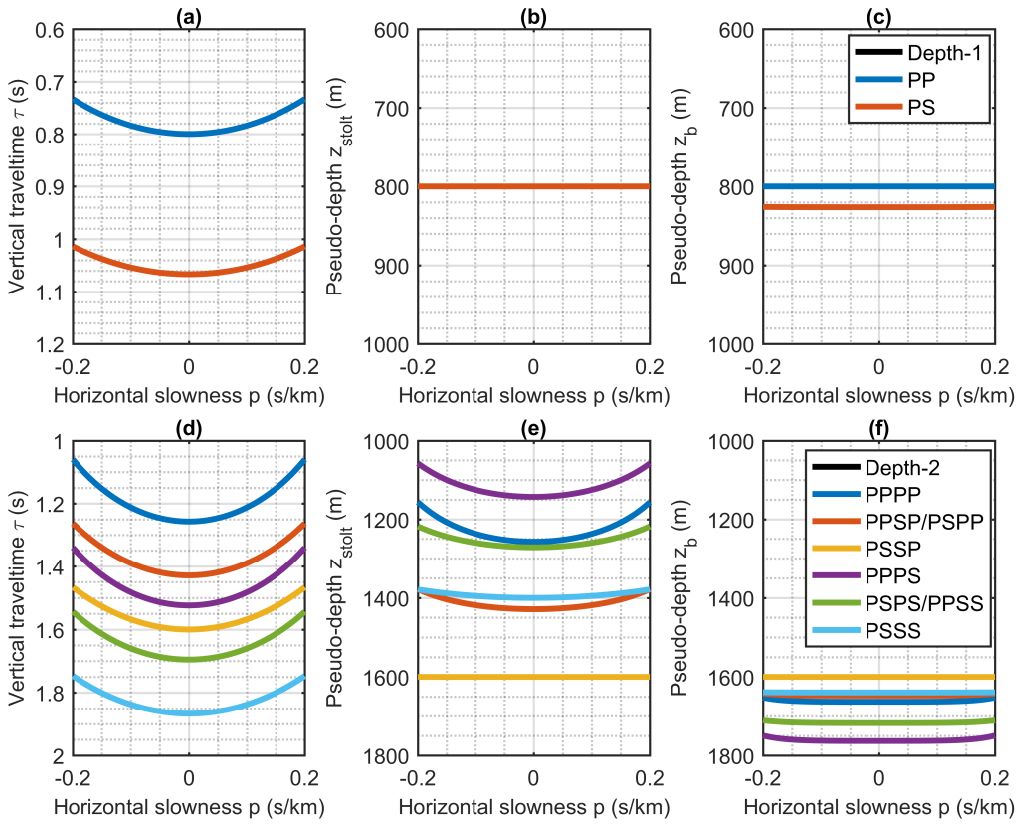

Figure 5.4: Comparison of vertical traveltimes, Stolt-depths, and pseudo-depths generated using best-fit stacking velocity. (a) The vertical travel-times of two primary reflections from the first interface. (b) Stolt-depths for the first interface primaries. (c) Best-fit pseudo-depths for the first interface primaries. (d) Vertical travel-times of primary reflections from the second interface. (e) Stolt-depths for the second interface primary events. (f) Best-fit pseudo-depths for the second interface primary events.

process spreads reflections caused by the second interface out into a wide range of pseudo-depths, separated by much more than the maximum ϵ admitted by the internal multiple prediction. The reflections $\grave{P}\grave{P}\acute{P}\acute{P}$ and $\grave{P}\grave{P}\acute{S}\acute{S}/\grave{P}\grave{S}\acute{P}\acute{S}$ are migrated into similar depths, whereas $\grave{P}\grave{P}\acute{P}\acute{S}$ has been over-migrated, and others have been under-migrated. I expect, based on this, Stolt-migrated/time-stretched inputs to create havoc within a multicomponent internal multiple prediction. For comparison I next calculate the best-fitting stacking velocity for each reflection, shown in Table 5.1; then, based on these, all reflection pseudo-depths (via equation 5.17). These are plotted in Figure 5.4c and 5.4f. These are not correct layer velocities, but are derived from basic data characteristics, and so they do not place all

Ray-path in P-P model	Best-fitting velocity v_s (m/s)
$\grave{P}\acute{P}$	2000
$\grave{P}\grave{P}\acute{P}\acute{P}$	2646
$\grave{P}\grave{P}\acute{S}\acute{P}/\grave{P}\grave{S}\acute{P}\acute{P}$	2306
$\grave{P}\grave{S}\acute{S}\acute{P}$	2000
Ray-path in P-SV model	Best-fitting velocity v_s (m/s)
$\grave{P}\acute{S}$	1549
$\grave{P}\grave{P}\acute{P}\acute{S}$	2314
$\grave{P}\grave{P}\acute{S}\acute{S}/\grave{P}\grave{S}\acute{P}\acute{S}$	2026
$\grave{P}\grave{S}\acute{S}\acute{S}$	1756

Table 5.1: The best fitting velocity for each ray-path.

of the reflections from the second interface at the same pseudo-depths. However, compared with the pre-stack elastic Stolt-migration depths, the reflections from the first interface, in Figure 5.4c, and the reflections from the second interface, in Figure 5.4f, all cluster within the bounds of a reasonably large ϵ value. Short-path internal multiples may be missed in predictions with slightly inflated ϵ values (e.g., Innanen, 2017), but the problem of multiple conversions along ray-paths should be significantly reduced.

5.6 Developing an elastic internal multiple prediction workflow

Possibly as the result of the difficulties described in the previous section, no numerical examples of multichannel inverse scattering series internal multiple predictions, on synthetic or field data, have to our knowledge been published. In this section I present and analyze a synthetic example of the prediction algorithm embodied in equation (5.20), with detailed discussion of the data preparation and required pre-processing.

5.6.1 Model parameters

A three-layer elastic model is built to create synthetic seismic records upon which elastic multiples can be predicted, and the pre-processing and prediction response issues discussed

above can be analyzed. The geological model and model parameters are plotted in Figure 5.5. From top to bottom, the P-wave velocities are $[2000, 3500, 2500]m/s$, the S-wave (meaning only SV-wave for all forthcoming numerical examples) velocities are $[1200, 2000, 1300]m/s$, and the densities are $[1.5, 2.25, 1.6]g/cm^3$. A P-wave source is located in the top and center of the model, and receivers are laid out with a 4m interval at the same depth. With four absorbing boundaries (dashed line in the model shown in Figure 5.5), the multi-component shot gather is generated using elastic finite differences *SOFI2D* (Bohlen, 2002).

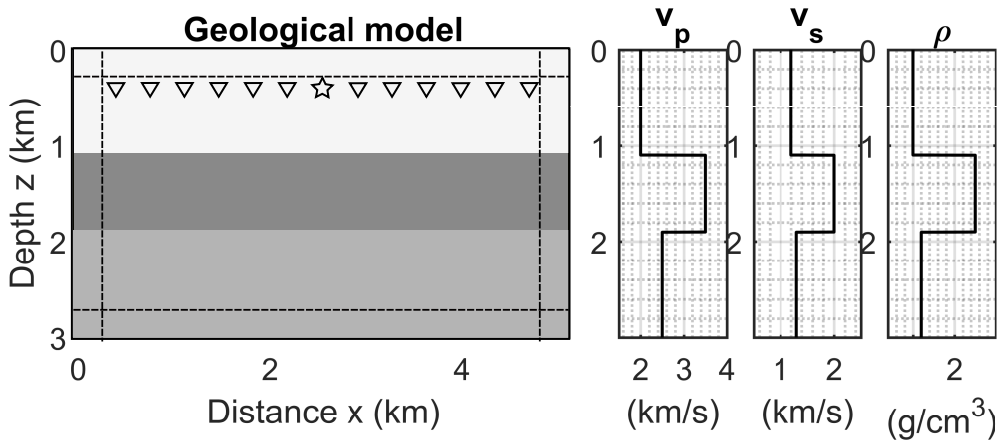

Figure 5.5: Geological model and model parameters. The left panel shows a three layers geological model, the right panels indicate model parameters for P-, S-wave velocities, and density. From top to bottom, $v_p = [2.0, 3.5, 2.5]$ in km/s, $v_s = [1.2, 2.0, 1.3]$ in km/s, $\rho = [1.5, 2.25, 1.6]$ in g/cm^3.

5.6.2 Data events

In Figure 5.6 the radial and vertical components of the single shot gather generated from the model illustrated in Figure 5.5. Prior to the main preprocessing, the data are transformed into their P- and S-wave components by calculating their divergence and curl (Dougherty and Stephen, 1988; Bohlen, 2002; Morse and Feshbach, 1953). The decomposed P- and S-wave components of the data are illustrated in Figure 5.7, with all reflection events labelled. The amplitude polarity is symmetric across zero offset in the P-wave record, and is reversed in the S-wave record. In Figure 5.7, both for P- and S-wave components, solid lines and

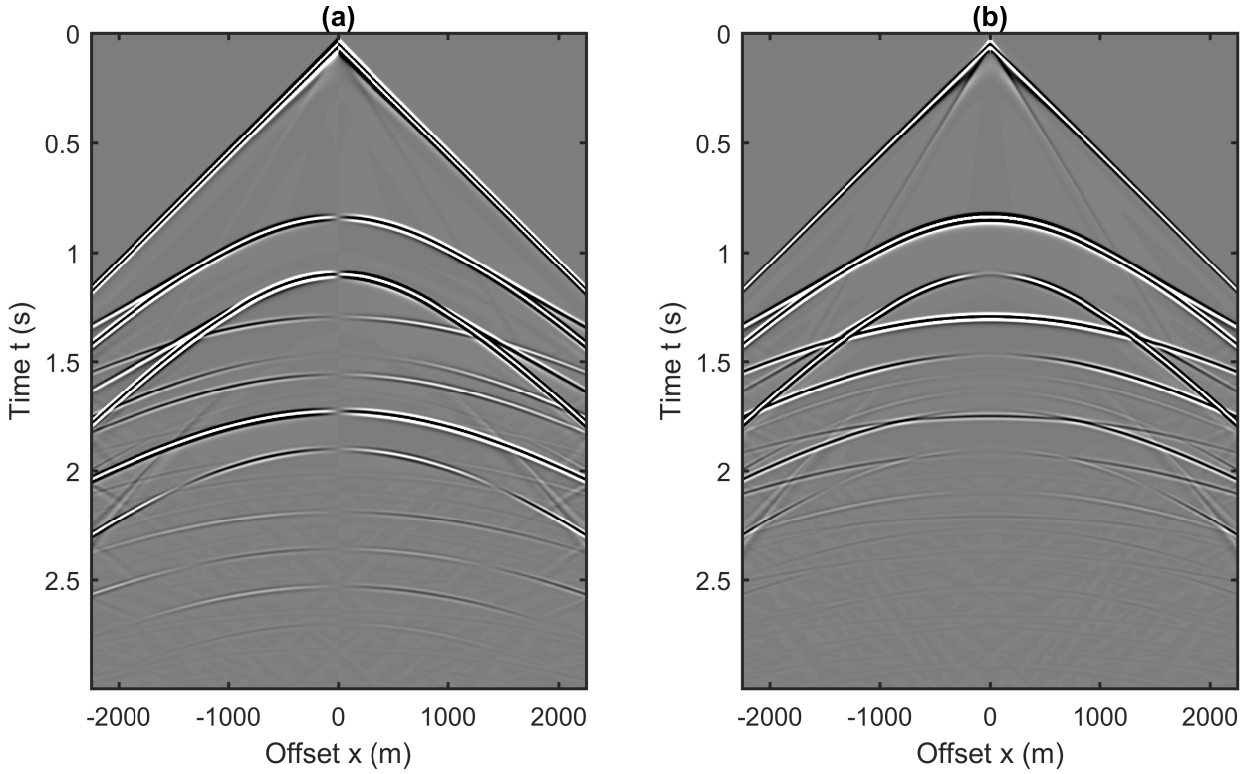

Figure 5.6: The multicomponent seismic records generated using model shown in Figure 5.5. (a) the radial component of the recorded data, (b) the vertical component of the recorded data.

the label Pr are used to indicate primaries, and the label IM is used to indicate internal multiples (dashed lines indicating first order multiples, dash-dotted lines indicating second order multiples, and dotted lines indicating third order multiples). Details of labels for all reflection events are provided in Table 5.2.

In Table 5.2, the superscript delineates wave-type. For primaries (Pr), the first subscript number represents the corresponding reflector. The second subscript is related to the number of S-wave ray-path segments in the event. It equals to the number of S-wave ray-path segments plus one in the P-wave mode, and equals to the number of S-wave ray-path segments directly in the S-wave mode. For instance, Pr_{22}^{P} is the P-wave component of the primary event that is reflected by the second reflector, and that is associated with two possible travel-paths: $\grave{P}\grave{P}\acute{S}\acute{P}$ and $\grave{P}\grave{S}\acute{P}\acute{P}$, both of which involve a single S-wave propagation leg, and both

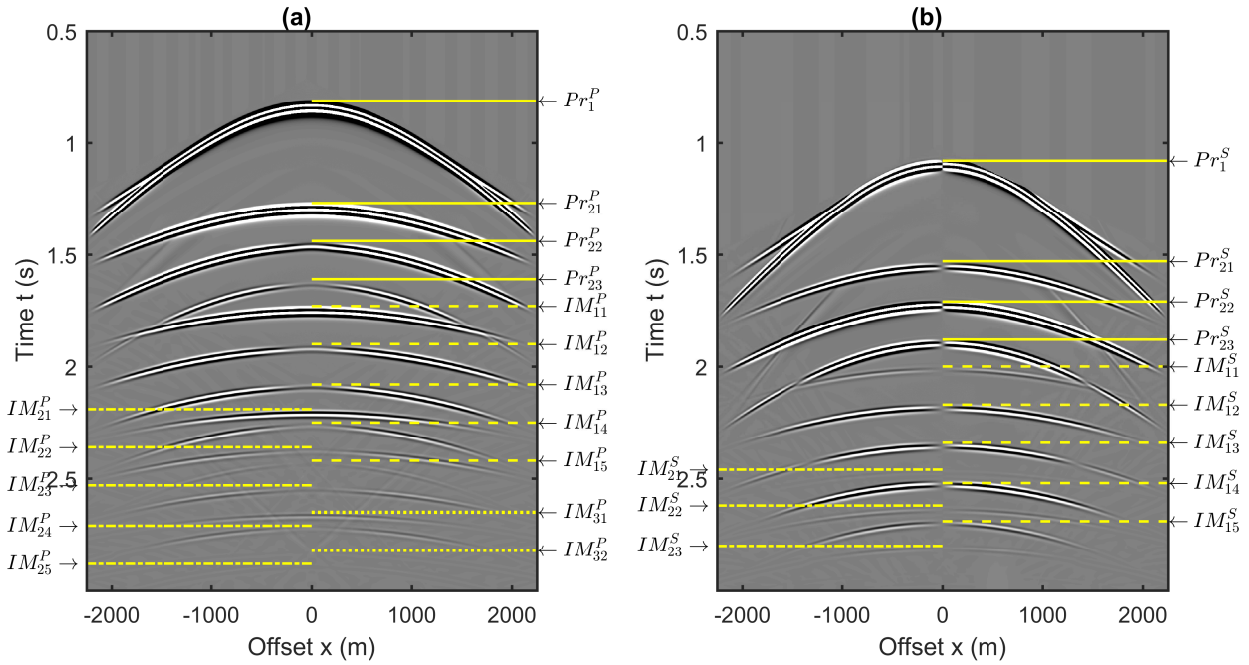

Figure 5.7: Synthetic displacement data in Figure 5.6 transformed to P- and S- components. Pr denotes primary events, which are indicated by solid lines. IM represent the internal multiples. All primaries are indicated in red solid lines. First-order internal multiples are labelled with magenta dashed-dotted lines. Second-order multiples are labelled with cyan dashed-dotted lines. Third-order multiples are labelled with yellow dashed-dotted lines. Further event details are provided in Table 5.2. (a) P-wave component of the recorded data. (b) S-wave component of the recorded data.

of which are recorded at the same time. For internal multiples (IM), the first subscript number is the order of the event, and the second number of subscript is selected using same system used for primaries. For example, IM_{22}^S includes all second order internal multiples received as S-wave components, which involve S-wave travel-paths:

$$\grave{P}\grave{P}\acute{P}\grave{P}\acute{P}\grave{P}\acute{S}\acute{S}, \quad \grave{P}\grave{P}\acute{P}\grave{P}\acute{P}\grave{S}\acute{P}\acute{S},$$

$$\grave{P}\grave{P}\acute{P}\grave{P}\acute{S}\grave{P}\acute{P}\acute{S}, \quad \grave{P}\grave{P}\acute{P}\grave{S}\acute{P}\grave{P}\acute{P}\acute{S},$$

$$\grave{P}\grave{P}\acute{S}\grave{P}\acute{P}\grave{P}\acute{P}\acute{S}, \quad \grave{P}\grave{S}\acute{P}\grave{P}\acute{P}\grave{P}\acute{P}\acute{S}.$$

5.6.3 Preparation of input data for prediction

In this section we will set out the two procedures necessary to prepare input data for the two prediction methods discussed in the previous section.

Pseudo-depth domain input via elastic Stolt migration

The inputs for the elastic prediction method described by Matson (1997) are pre-stack elastic Stolt-migrations, generated using two constant background velocities for P- and S-waves. The re-gridding of angular frequency and the calculation of the Jacobian of the coordinate transform are the key elements of the creation of the input. In Figure 5.8, the re-gridding from angular frequency to vertical wavenumber k_z in terms of the wavenumber k_x and the horizontal slowness p are illustrated, for the P-P and P-S components, i.e., $\omega(k_z^P)$ and $\omega(k_z^S)$, respectively. In Figure 5.9 the migrated images, generated (with reference P- and S-wave velocities matching those of the top layer) using wavenumber and horizontal slowness variables for P-P and P-S components, are plotted. The input for internal multiple prediction in the pseudo-depth domain are obtained by multiplying these data by the weight factor $-2i\nu_s^P$ (see Weglein et al., 1997, for a discussion of this factor in the context of acoustic prediction).

Let us compare Figures 5.9a-b with 5.9c-d, i.e., inputs generated in the wavenumber domain versus those generated in the slowness domain. The P-P panel in the wavenumber domain exhibits a marked distribution or smearing of the events along the Stolt-depth axis especially as $|k_x|$ increases; the P-S panel in addition to this exhibits strong aliasing. Whereas, in the p domain both P-P and P-S map data events to forms which are compact along the Stolt-depth axis across the full p range. However, issues remain: I observe hyperbolic aliasing events in the P-P component and elliptical aliasing events in the P-S component, which, though not as severe as the artifacts in the wavenumber domain, will nonetheless have an impact on prediction.

Continuing, the final migrated image traces for the P-P and P-S components are plotted

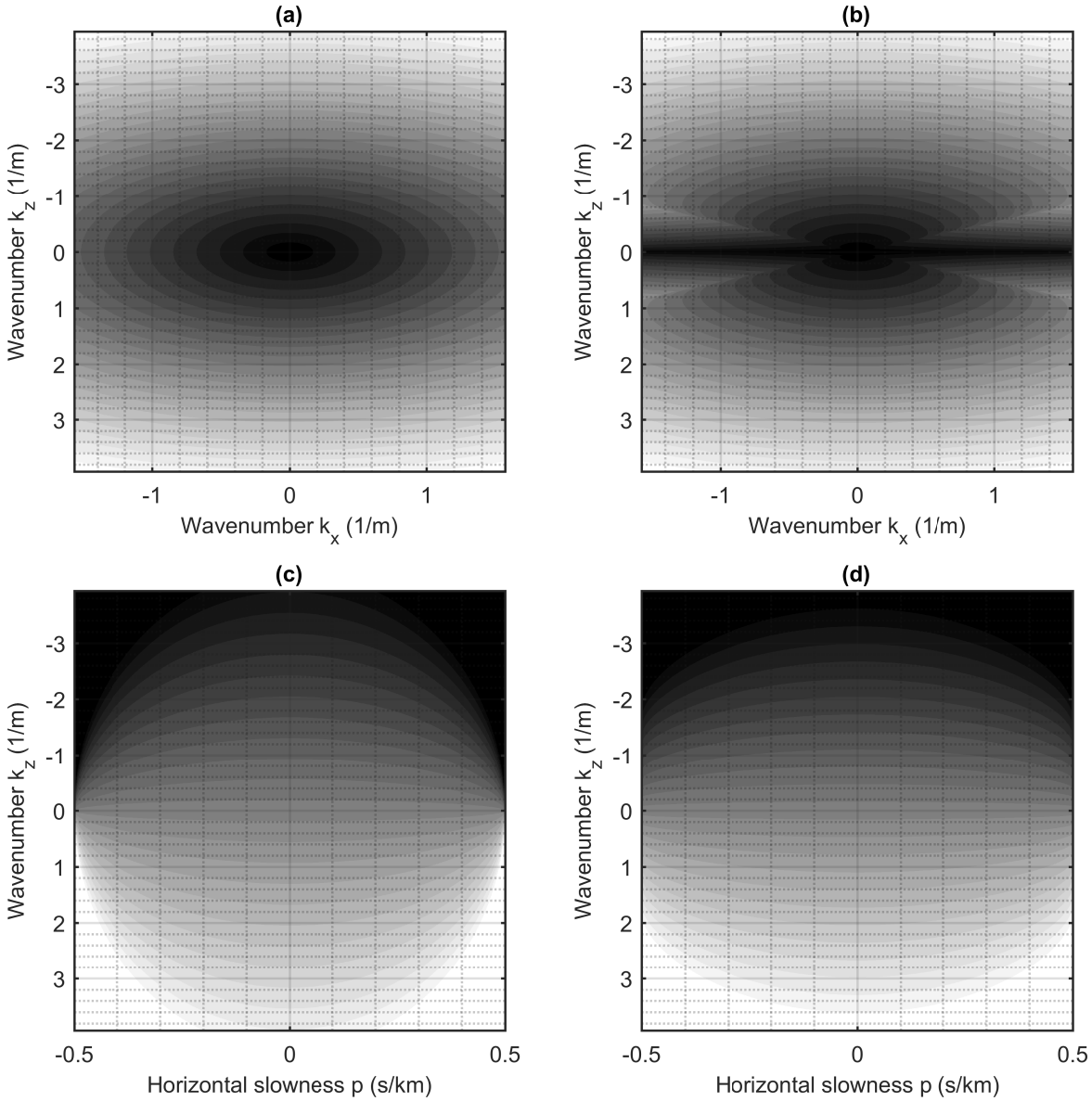

Figure 5.8: Re-gridding from angular frequency to vertical wavenumber $\omega(k_z)$: (a) $\omega(k_x, k_z^P)$. (b) $\omega(k_x, k_z^S)$. (c) $\omega(p, k_z^P)$. (d) $\omega(p, k_z^S)$..

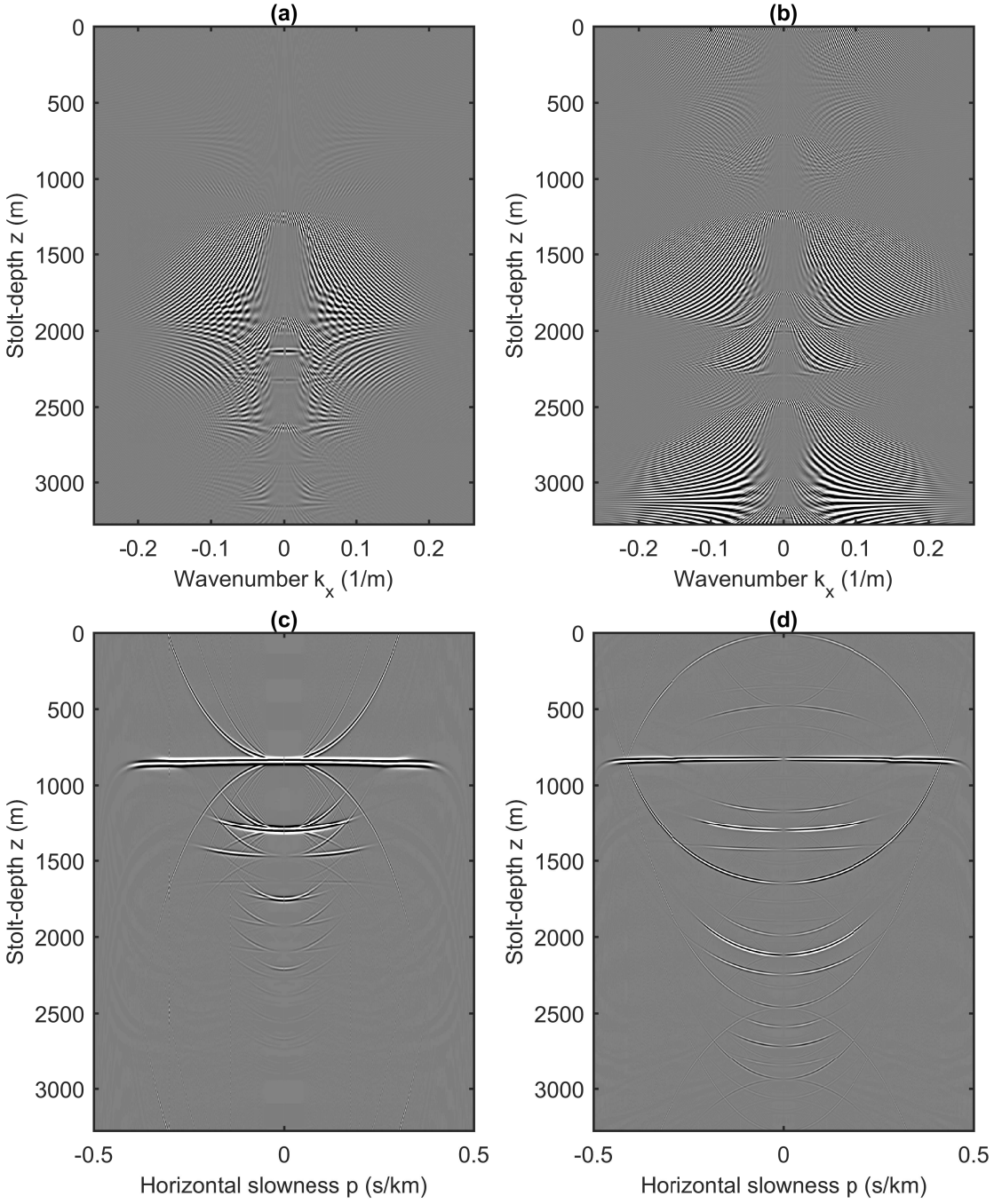

Figure 5.9: The pre-processed data inputs, ready for pseudo-depth domain prediction, generated using pre-stack elastic Stolt migration with two constant background velocities. (a) The P-P migrated image $R(k_x, z)$ in the wavenumber domain. (b) The P-S migrated image $R(k_x, z)$ in wavenumber domain. (c) The P-P migrated image $R(p, z)$ in the horizontal slowness domain. (b) The P-S migrated image $R(p, z)$ in the horizontal slowness domain.

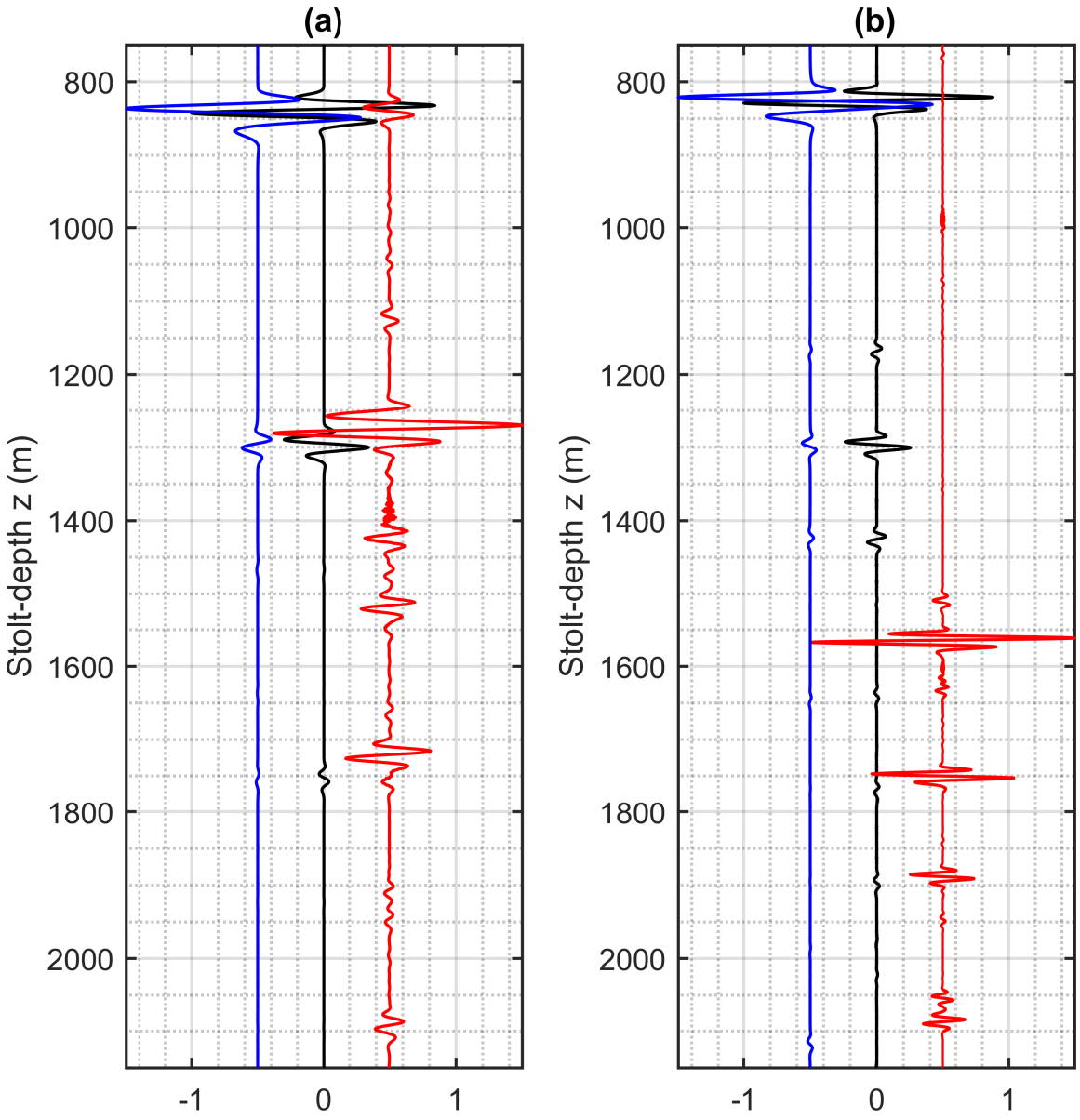

Figure 5.10: Comparisons of elastic Stolt-migrated traces and zero-offset trace. Black indicates zero-offset trace, red represents migrated traces with wavenumber, blue delineates migrated traces using horizontal slowness (a) for P-P reflection. (b) for P-S reflection.

in Figure 5.10, those generated from the k_x domain input and from the p domain input. The zero-offset traces are plotted against $\tilde{z}_{stolt} = \tau/(q_s^P + q_g^S)$ for comparison. The elastic Stolt-migrated traces generated using the horizontal slowness match almost exactly with vertical travel-time results in equation 5.13; the migrated traces derived from the wavenumber generates significant issues, in particular in the P-S component. Implementing multicomponent internal multiple prediction in the plane-wave domain with vertical travel-time stretching is identical to implementation of prediction algorithm in the pseudo-depth domain, but with fewer artifacts. However, both of these two approaches, for reasons described above, will require impractically large ϵ values.

Plane-wave domain input via Radon transform

In the plane-wave domain, inverse series internal multiple predictions can be implemented by exchanging the standard integral limits with the appropriate weighted time quantity; for instance, with the vertical-traveltime stretching condition (equation 5.8) or the best-fitting condition (equation 5.21). Let us next compare inputs derived in this domain to the standard domains discussed in the previous section.

In Figure 5.11, the traditional plane-wave transformations of the P-P and P-S components of the data are plotted. Best-fitting velocity models are next determined. Following (Trad et al., 2002), a high-resolution hyperbolic Radon transform is performed for each data component. To locate the maxima which imply best-fitting velocities, in particular for the larger vertical travel-times, I apply a gain filter along the time-axis proportional to t^α. A non-uniform velocity interval Δv would tend to enhance the sparseness of the Radon panel, however, this non-uniformity is empirically found to introduce scatter in the best-fitting velocity picking. Hence, a small uniform interval ($\Delta v = 20m/s$) was chosen for the velocity grid used in the hyperbolic Radon transform. The Radon panel with the best-fit velocity picks are plotted in Figure 5.12; I find that there is no need to obtain a best-fitting velocity for every reflection, particularly at large vertical travel-times, where changing the details

of wave mode conversions produces less distinct outcomes. In Figure 5.13, the best-fitting velocity models for the synthetic P-P and P-S components are plotted.

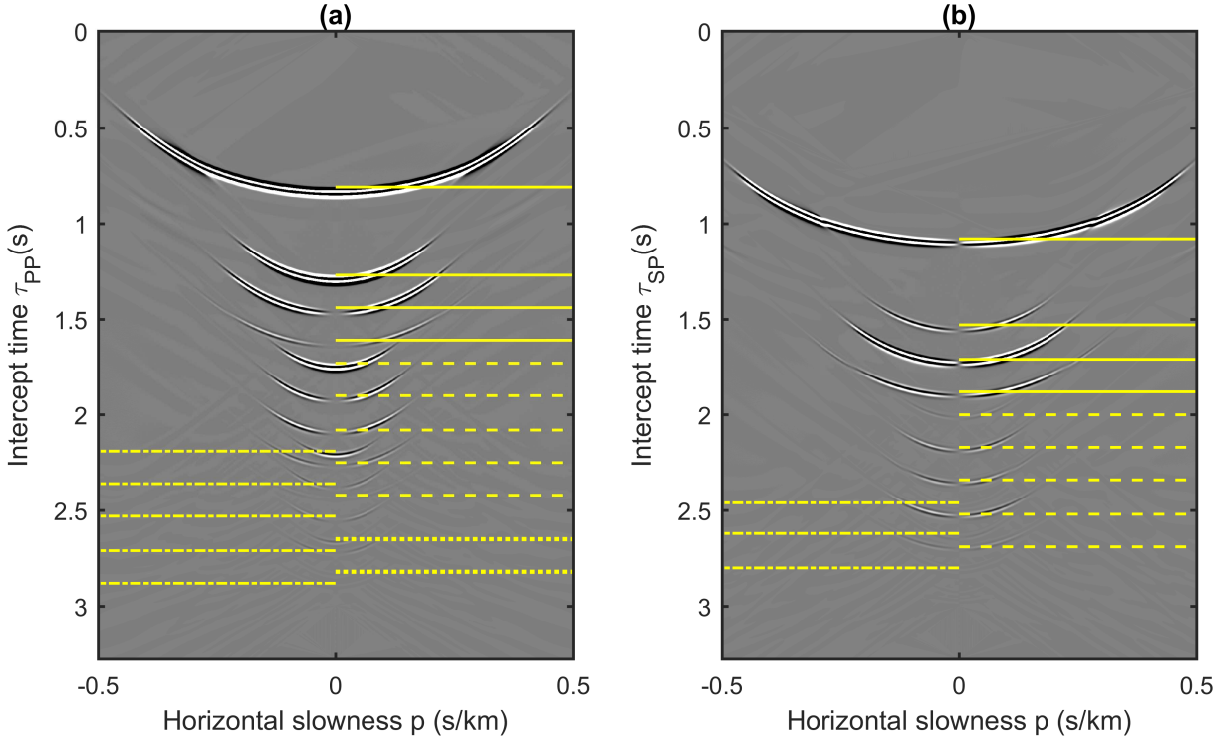

Figure 5.11: Linear Radon transform of the data plotted in Figure 5.7. (a) P-wave component in the linear Radon space. (b) S-wave component in the linear Radon space.

5.6.4 Numerical predictions of elastic internal multiples

Because all of the inputs I have examined in the pseudo-depth domain exhibit significant aliasing, all numerical predictions of multicomponent internal multiples in this section are computed in the plane-wave domain. Here I examine and compare elastic internal multiple predictions generated using both vertical travel-time stretching (i.e., equation 5.8) and best-fit velocities (i.e., equation 5.21).

Predictions with vertical travel-time stretching

Analysis of vertical travel-time stretching was suggestive that large values of the search parameter ϵ would be needed (which put the prediction in jeopardy of missing important

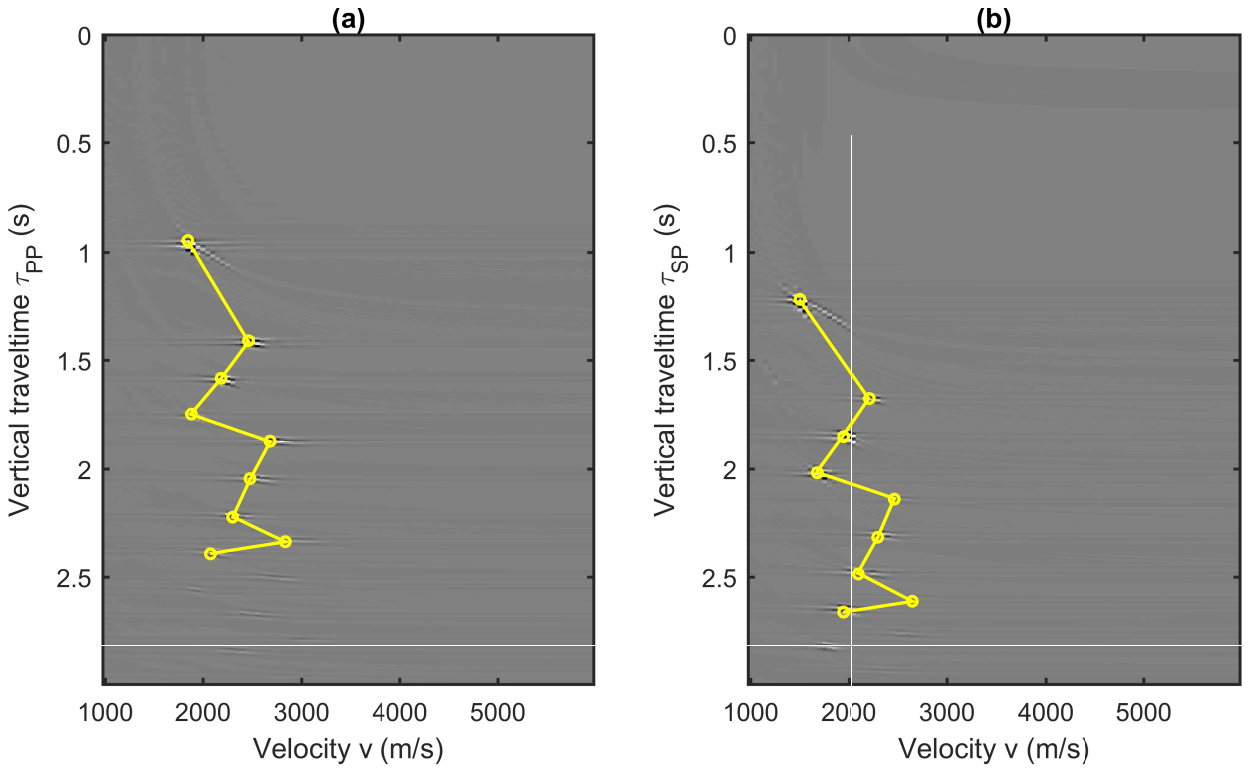

Figure 5.12: Hyperbolic Radon transforms of the data plotted in Figure 5.7, with best-fitting velocity picks overlain. Yellow circles indicate the maxima picked for each reflection. (a) The P-P component in the hyperbolic Radon space. (b) The P-S component in the hyperbolic Radon space.

multiple events). Therefore, $\epsilon = 200$ms was selected, which is twice the dominant period of the source wavelet ($96ms$). In Figure 5.15 the predicted results for the P-P and P-S components are plotted, using the same event labeling as Figure 5.7. I observe that most of the elastic internal multiples are correctly predicted in this panel, but, several undesired events or artifacts appear also. For instance, predictions at the arrival times of two primary reflections are present at near-offsets in the P-P component prediction, and one primary appeared in prediction of P-S component. These artifacts correspond to event combinations satisfying the lower-higher-lower condition incorrectly, because the vertical time-stretching method was unable to organize primaries such that their actual depths increase monotonically with their pseudo-vertical traveltimes. This is exemplified in Figure 5.16, in which the ray-path combinations causing one of the artifacts in Figure 5.15 are illustrated.

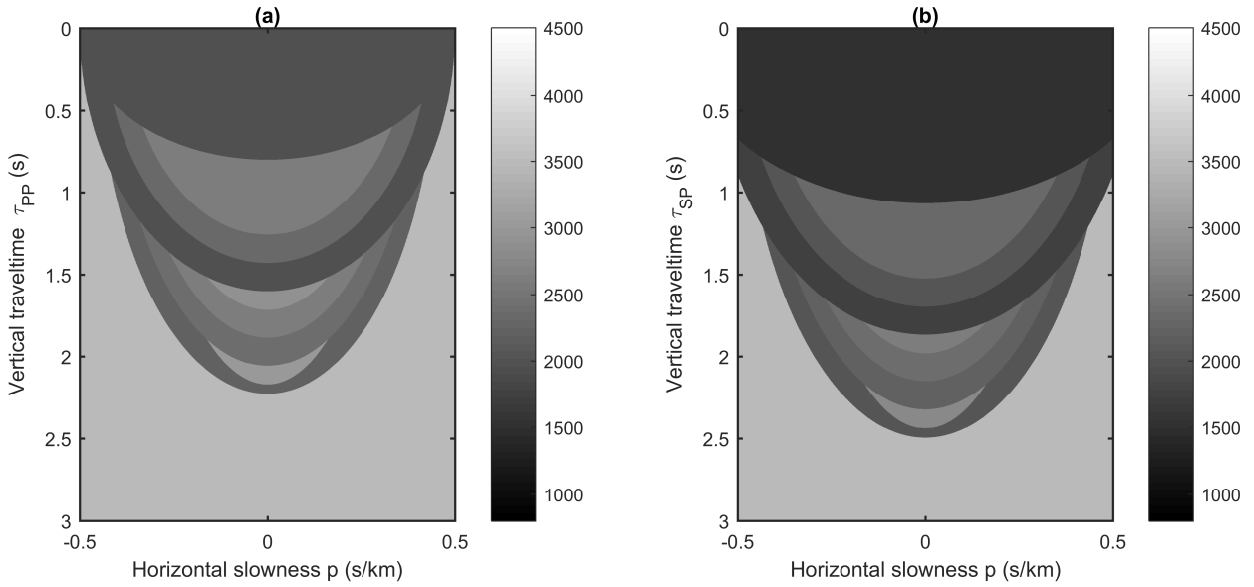

Figure 5.13: Best-fitting velocity models in the linear Radon space picked from Figure 5.12. (a) P-wave component velocity. (b) S-wave component velocity.

Prediction with best-fit reference velocities

A relatively large ϵ is also expected to be necessary for multicomponent internal multiple prediction using velocities derived from the best-fit approach. Hence, I again employed $\epsilon = 200$ms in this case. The P-P and P-S component predictions are plotted in Figure 5.17. Unlike the prediction with vertical traveltime-stretching method, however, using this same value for ϵ, no artifacts correlated with primary events appear in either the P-P and P-S component predictions, and all elastic internal multiples at different orders are predicted at their correct traveltimes. I conclude that prediction using best-fit reference velocities produces much better results than with either vertical-traveltime-stretching or prestack elastic Stolt-migration. However, this still took place in the context of large search parameter values, which increase the danger of missing prediction of the shorter-path internal multiples.

Mixed stretching / best-fit velocities

A combination of vertical travel-time stretching and best-fit reference velocities when combined appear to optimize the elastic predictions. By mixing the two, I find I am able

to produce the predictions plotted in Figure 5.18 using a much smaller search parameter ($\epsilon = 96$ms) in both the P-P and P-S panels. Once again, no artifacts are introduced, and in this case a more inclusive search for sub-events is permitted.

5.7 Conclusion

Accurate onshore internal multiple prediction and removal in the absence of clearly identifiable generators and velocity models is an increasingly high priority problem in seismic data processing especially in unconventional reservoir characterization where sophisticated quantitative interpretation is apt to be applied. The inverse scattering series internal multiple attenuation approach in principle addresses these needs. A full practical solution of this problem using the inverse series approach requires that (1) multicomponent acquisition, and (2) the possibility of events undergoing one or more elastic conversions, both be admitted. Elastic theory for internal multiple prediction was set out in the 1990s and examined with analytic data, but no numerical examples or analysis of the methodology, on even simple synthetics, have ever appeared in the literature. Here I extend the theory from 2D to 3D, implement it numerically, and examine the challenges of its numerical implementation, which are significant.

The algorithm formulation is in the plane-wave domain, which requires the relative ordering of reflected seismic events in true depth, pseudo-depth, and pseudo vertical-traveltime to be considered. It appears that all possible elastic internal multiples can be estimated by appropriate nonlinear calculations on weighted, P- and S- decomposed seismic records, with no subsurface information provided. However, the bar for input preparation, in which all data events must appear at vertical travel-times or pseudo-depths that are monotonic functions of actual reflection depths, is exceedingly high. Multiple wave-mode conversions within events which are treated with linear elastic pre-processing (which allow for single mode conversions only) greatly increase the chance of input events violating the lower-higher-lower

relationship, and introducing artifacts.

I propose and examine several possible methods for multicomponent input preparation, such as pre-stack elastic Stolt-migration, vertical travel-time stretching, and incorporation of best-fit stacking velocities. Their effectiveness, and search parameter dependencies are analyzed, leading to several conclusions: (1) neither pre-stack elastic Stolt-migration nor vertical travel-time stretching appropriately honour the requirement for monotonicity; (2) input prepared with best-fit reference velocities is closer to obeying the monotonicity requirements, but in practice must be allowed a relatively large searching parameter, and this suppresses prediction of all shorter-path multiples. A combination of vertical travel-time stretching and best-fit reference velocities allows the search parameter to be chosen with a size comparable to those used in acoustic prediction, while correctly predicting all orders of multiple. These expectations are borne out with synthetic elastic data examples, which are the first elastic inverse series predictions to be presented.

Label-P	Primaries in P-mode	Label-S	Primaries S-mode
Pr_1^P	$\grave{P}\acute{P}$	Pr_1^S	$\grave{P}\acute{S}$
Pr_{21}^P	$\grave{P}\grave{P}\acute{P}\acute{P}$	Pr_{21}^S	$\grave{P}\grave{P}\acute{P}\acute{S}$
Pr_{22}^P	$\grave{P}\acute{P}\acute{S}\acute{P}$ & $\grave{P}\grave{S}\acute{P}\acute{P}$	Pr_{22}^S	$\grave{P}\acute{P}\acute{S}\acute{S}$ & $\grave{P}\grave{S}\acute{P}\acute{S}$
Pr_{23}^P	$\grave{P}\grave{S}\acute{S}\acute{P}$	Pr_{23}^S	$\grave{P}\grave{S}\acute{S}\acute{S}$
Label-P	1st-order IMs in P-mode	Label-S	1st-order IMs in S-mode
IM_{11}^P	$\grave{P}\grave{P}\acute{P}\grave{P}\acute{P}\acute{P}$	IM_{11}^S	$\grave{P}\grave{P}\acute{P}\grave{P}\acute{P}\acute{S}$
IM_{12}^P	$\grave{P}\grave{P}\acute{P}\grave{P}\acute{S}\acute{P}$	IM_{12}^S	$\grave{P}\grave{P}\acute{P}\grave{P}\acute{S}\acute{S}$
IM_{13}^P	$\grave{P}\grave{P}\acute{P}\grave{S}\acute{S}\acute{P}$	IM_{13}^S	$\grave{P}\grave{P}\acute{P}\grave{S}\acute{S}\acute{S}$
IM_{14}^P	$\grave{P}\grave{P}\acute{S}\grave{S}\acute{S}\acute{P}$	IM_{14}^S	$\grave{P}\grave{P}\acute{S}\grave{S}\acute{S}\acute{S}$
IM_{15}^P	$\grave{P}\grave{S}\acute{S}\grave{S}\acute{S}\acute{P}$	IM_{15}^S	$\grave{P}\grave{S}\acute{S}\grave{S}\acute{S}\acute{S}$
Label-P	2nd-order IMs in P-mode	Label-S	2nd-order IMs in S-mode
IM_{21}^P	$\grave{P}\grave{P}\acute{P}\grave{P}\acute{P}\grave{P}\acute{P}\acute{P}$	IM_{21}^S	$\grave{P}\grave{P}\acute{P}\grave{P}\acute{P}\grave{P}\acute{P}\acute{S}$
IM_{22}^P	$\grave{P}\grave{P}\acute{P}\grave{P}\acute{P}\grave{P}\acute{S}\acute{P}$	IM_{22}^S	$\grave{P}\grave{P}\acute{P}\grave{P}\acute{P}\grave{P}\acute{S}\acute{S}$
IM_{23}^P	$\grave{P}\grave{P}\acute{P}\grave{P}\acute{P}\grave{S}\acute{S}\acute{P}$	IM_{23}^S	$\grave{P}\grave{P}\acute{P}\grave{P}\acute{P}\grave{S}\acute{S}\acute{S}$
IM_{24}^P	$\grave{P}\grave{P}\acute{P}\grave{P}\acute{S}\grave{S}\acute{S}\acute{P}$		
IM_{25}^P	$\grave{P}\grave{P}\acute{P}\grave{S}\acute{S}\grave{S}\acute{S}\acute{P}$		
Label-P	3rd-order IMs in P-mode		
IM_{31}^P	$\grave{P}\grave{P}\acute{P}\grave{P}\acute{P}\grave{P}\acute{P}\grave{P}\acute{P}\acute{P}$		
IM_{32}^P	$\grave{P}\grave{P}\acute{P}\grave{P}\acute{P}\grave{P}\acute{P}\grave{S}\acute{S}\acute{P}$		

Table 5.2: The meaning of symbols used in Figure 5.7. Pr labels primary events and IM labels internal multiples. The superscript represents the wave mode at the receiver. In the primary subscripts, the first number labels the related reflector, and the second number is the number of S-wave legs between the fist and last path plus one. In the internal multiple subscripts, the first number labels the multiple order, and the second number again represents the number of S-wave legs of the event.

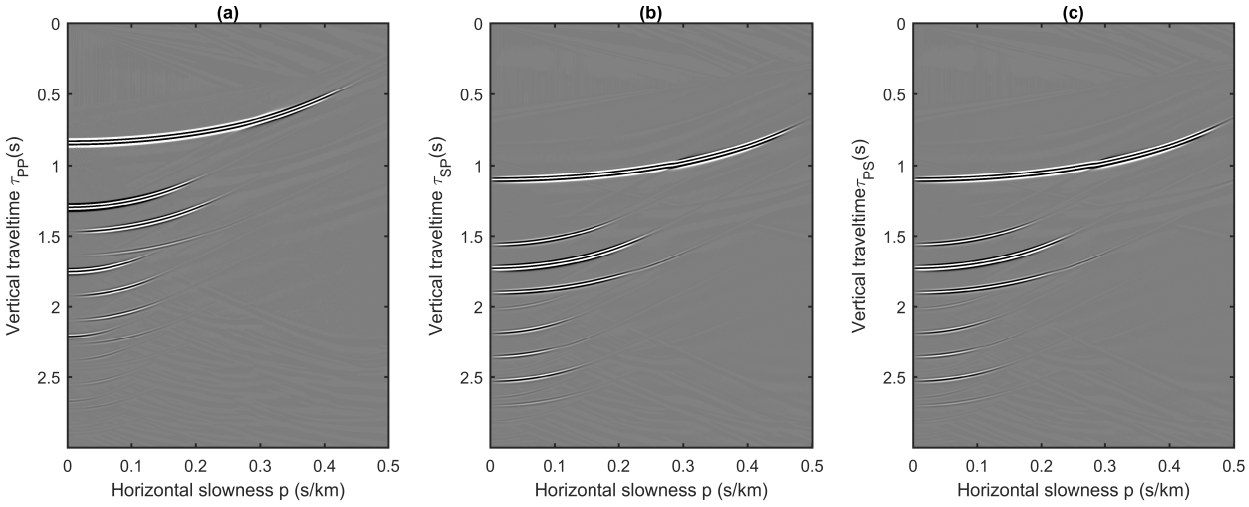

Figure 5.14: Three inputs of elastic internal multiples prediction using plane wave domain ISS algorithm for a P-wave source in positive p range. (a) The input $b_1^{\acute{P}\grave{P}}$, (b) the input $b_1^{\acute{S}\grave{P}}$, (c) the input $b_1^{\acute{P}\grave{S}}$.

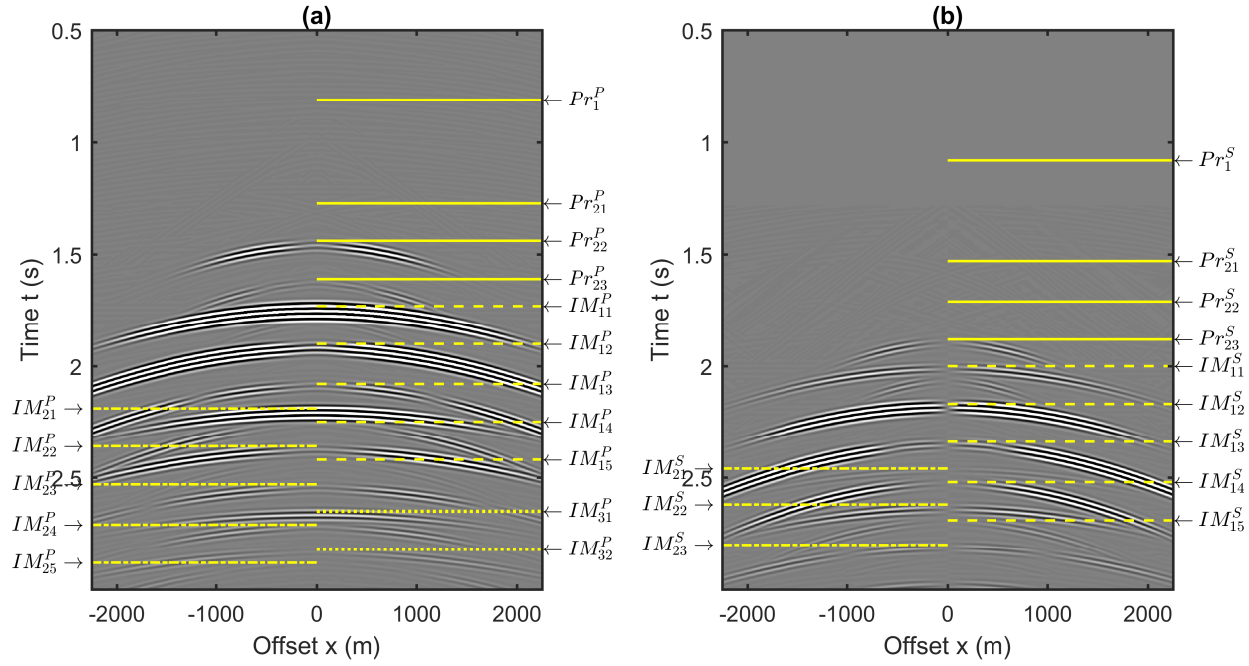

Figure 5.15: Plane wave domain multicomponent internal multiple prediction using the vertical traveltime-stretching condition with $\epsilon = 200$ms. (a) P-wave component; (b) S-wave component.

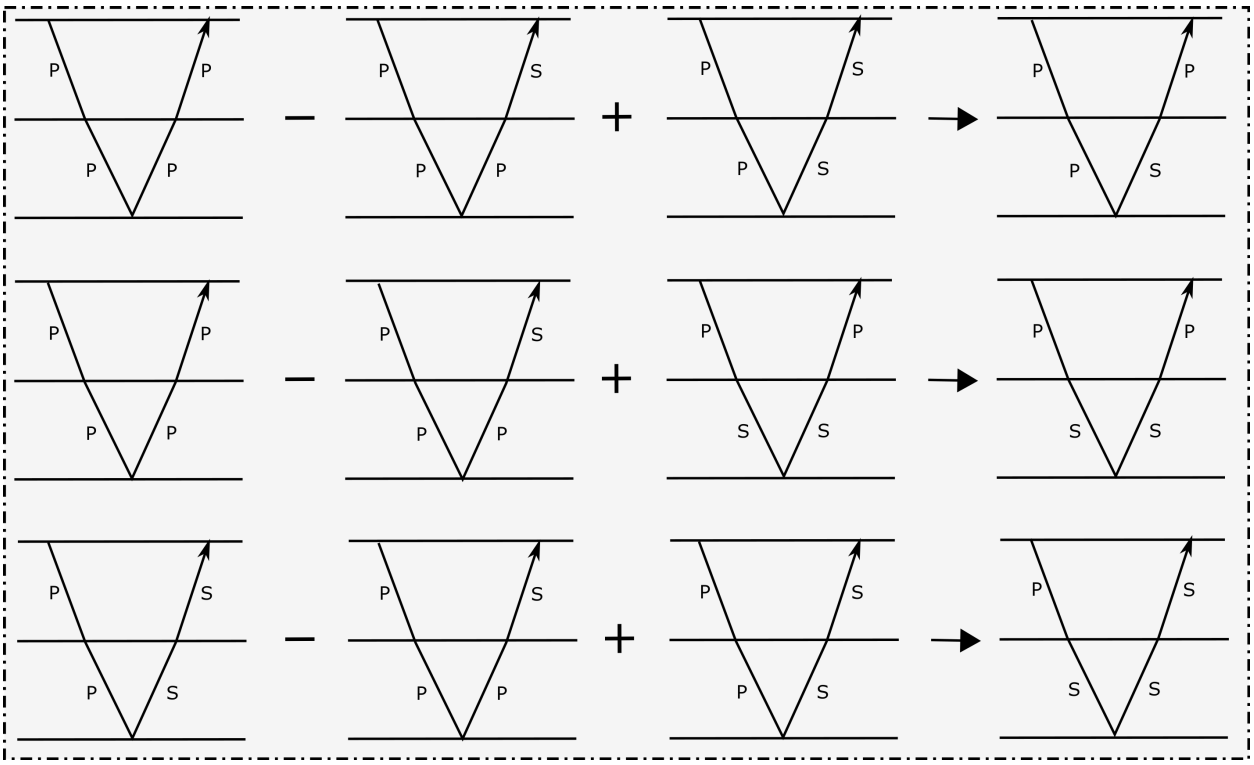

Figure 5.16: Examples of false sub-event combinations leading to artifacts in Figure 5.15. The first row is one false combination for generating $\grave{P}\acute{P}\acute{S}\acute{P}$. The second row is one false combination for reconstructing $\grave{P}\grave{S}\acute{S}\acute{P}$. The 3rd row is one false combination for predicting $\grave{P}\grave{S}\acute{S}\acute{S}$.

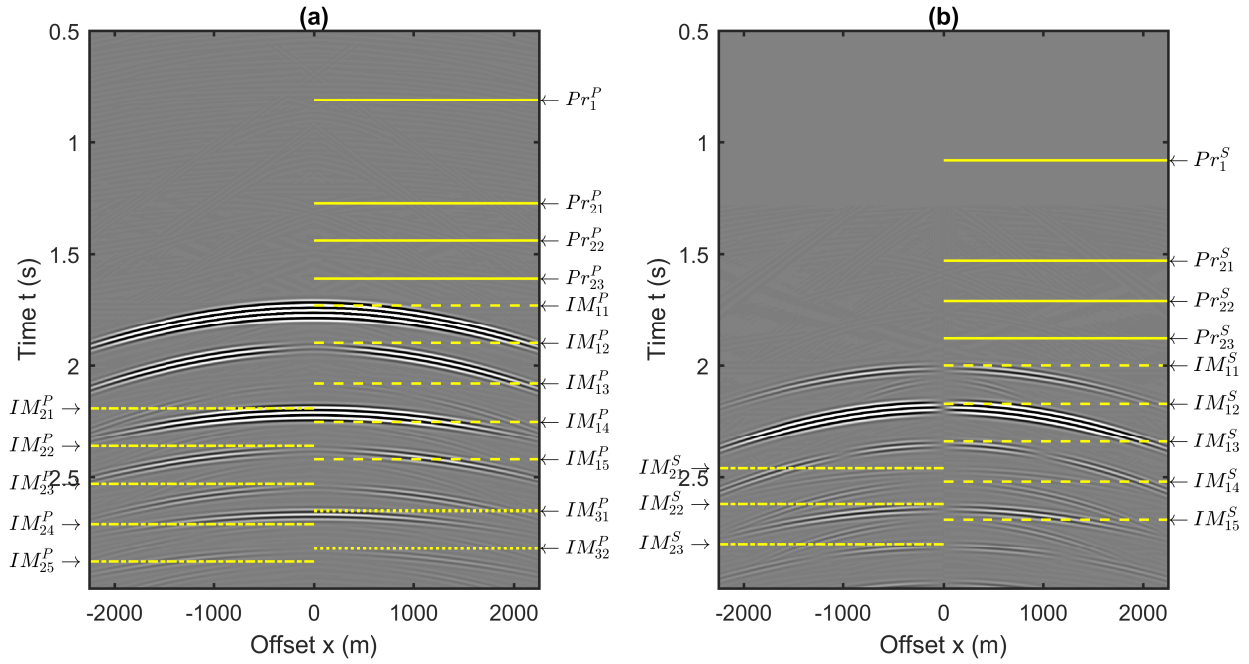

Figure 5.17: Plane wave domain multicomponent internal multiple prediction using the best-fit reference velocities, with $\epsilon = 200$ms. (a) P-wave component prediction; (b) S-wave component prediction.

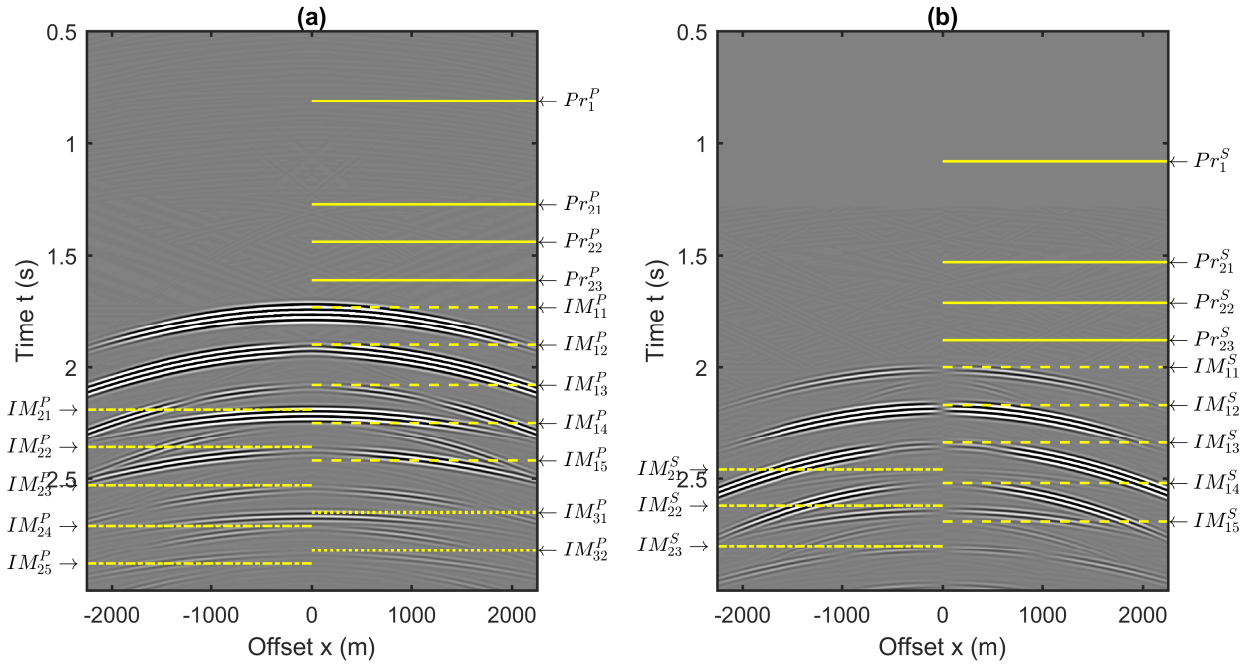

Figure 5.18: Plane wave domain multicomponent internal multiple prediction using a mixed vertical travel-time stretching and best-fit reference velocity approach, with $\epsilon = 96$ms. (a) P-wave component prediction; (b) S-wave component prediction.

Chapter 6

Conclusions and future study

Prediction of internal multiples in complex media, caused by unknown generators, is an increasingly high-priority problem, because of the growing roles of quantitative amplitude analysis and inversion in complex reservoir environments. Inverse scattering series internal multiple prediction algorithm is a powerful tool and data-driven method to predict internal multiples in such environments. However, implementation of the algorithm encounters great challenges, such as optimizing and formulating algorithms in a range of domains, selection of ad hoc parameters, suppression of various (e.g., high-angle) artifacts, and computational costs. In this thesis, to address these issues, I present an implementation of the inverse scattering series internal multiple prediction algorithm in the coupled plane-wave domain. Comparing prediction inputs obtained from a range of calculation domains, the analysis shows that the horizontal-slowness-related inputs allow a relatively stationary optimum ϵ value by concentrating the amplitude distribution of each sub-event, which gives traceable parameter selection and successfully eliminate the high-angle artifacts in the prediction. Moreover, the input in the coupled plane-wave domain appears as a highly sparse matrix which significantly reduces its computational expense.

Based on the plane-wave inverse scattering series prediction algorithm, the input of multidimensional internal multiple prediction can be obtained by the couple plane-wave transformed dataset which requires shots occupying each receiver's location. The high-resolution Radon transform, as a proven well-established interpolation method, reduces this dependency. To accommodate internal multiple prediction in common-midpoint (CMP) domain, I proposed a modified version of the algorithm appropriate for this domain. Numerical analysis indicates that, in contrast to the shot/receiver gather prediction, the CMP domain internal

multiples prediction algorithm is relatively dip-angle independent. Therefore, for dipping strata with small dipping angles, multidimensional (dipping-reflector related) internal multiples can be predicted using the simplified 1.5D algorithm with what are likely acceptable error levels. Beyond that, the symmetry of CMP gathers also supports practical numerical features, such as taper windows for elimination of aperture artifacts, which are not available in the shot/receiver gather algorithms.

To further support the use of inverse scattering series methods in onshore internal multiple prediction, I extend elastic inverse scattering series internal multiple prediction algorithm from 2D to 3D, accommodating multicomponent acquisition and the possibility that reflected events undergo more than one elastic wave-mode conversion during their propagation histories. The linear pre-processing for elastic prediction in the presence of multiple wave-mode conversions greatly increases the chance of input events violating the "lower-higher-lower" event ordering rules of the inverse series approach, thereby introducing artifacts. Its implementation was numerically examined and analyzed along with the investigation of the ordering rules, which are based on elastic monotonicity conditions amongst actual depths, pseudo-depths, and pseudo-vertical traveltimes. Several possible approaches are proposed and analyzed to produce elastic prediction input which honours the same relative ordering of events as those produced in actual depth. Numerical examples on a synthetic benchmark dataset indicates all possible elastic internal multiples are estimated with best-fit reference velocities, but that a relatively large search parameter is required. A combination of vertical traveltime stretching and best-fit reference velocities allows the search parameter to be chosen with a size comparable to those used in acoustic prediction, while correctly predicting all orders of multiple.

The inverse scattering series internal multiple algorithm still needs to be examined more closely in the context of field seismic records, even though many challenges of its implementation have been solved and optimized in this thesis. Full waveform inversion (FWI)

and least-squares reverse time migration (RTM) are powerful and promising techniques to achieve high-resolution estimation of subsurface properties and images by minimizing the residuals between measured data and modeled data. Understanding the behaviour of primaries and multiples in reduction of residuals may provide valuable information of optimum direction; so, even in methods in which in principle multiples should not be removed from data, accurate predictions and the ability to discriminate is likely very important. Furthermore, the separate calculation of FWI sensitives involving direct events (standard FWI) and primary events (within the relatively recent advances in reflection FWI) could potentially be augmented with sensitivity calculations associated with multiples in isolation; such future endeavours based on careful prediction may lead to high-resolution delineation of reservoir target zones.

Appendix A

Diagonalization and rotation of elastic wave operator, Green function, and scattering potential

A.1 Elastic wave operator and scattering potential

Start with the stress-strain relation for an isotropic elastic medium,

$$\sigma_{ij} = \lambda \mathcal{D} \delta_{ij} + 2\mu e_{ij} \tag{A.1}$$

where, $i, j = 1, 2, 3$, λ and μ are knowns as *Lamé constants*, $\mathcal{D} = \sum_{k=1}^{3} e_{kk} = \nabla \cdot \mathbf{u}$ is the dilatation.

Euler's equation of motion will reduce to *Cauchy's equation of motion* if the infinitesimal theory of elasticity is considered,

$$\frac{\partial \vec{\boldsymbol{\sigma}}}{\partial \vec{\mathbf{r}}} + \boldsymbol{\mathcal{F}} + \rho\omega^2 \mathbf{u} = 0 \tag{A.2}$$

Considering stress-strain relation, the first term in the equation of motion can be expanded as, in vector notation,

$$\frac{\partial \vec{\boldsymbol{\sigma}}}{\partial \vec{\mathbf{r}}} = (\lambda + \mu)\nabla(\nabla \cdot \vec{\mathbf{u}}) + (\nabla\lambda)\nabla \cdot \vec{\mathbf{u}} + \mu\nabla^2 \vec{\mathbf{u}} + (\nabla\vec{\mathbf{u}} + \vec{\mathbf{u}}\nabla) \cdot (\nabla\mu) \tag{A.3}$$

Reword the *Cauchy's equation of motion* by substituting the expansion (equation A.3) and leaving out the body forces,

$$(\lambda + \mu)\nabla(\nabla \cdot \vec{\mathbf{u}}) + (\nabla\lambda)\nabla \cdot \vec{\mathbf{u}} + \mu\nabla^2 \vec{\mathbf{u}} + (\nabla\vec{\mathbf{u}} + \vec{\mathbf{u}}\nabla) \cdot (\nabla\mu) + \rho\omega^2 \mathbf{u} = 0 \tag{A.4}$$

Based on Eq. (A.4), the wave equation in frequency domain for an elastic isotropic medium can be derived and expressed in terms of propagating operator,

$$\boldsymbol{\mathfrak{L}}(\mathbf{r}, \omega)\mathbf{u}(\mathbf{r}, \omega) = 0 \tag{A.5}$$

where,

$$\begin{aligned}
\mathfrak{L}_{ii} &= \partial_i[(\lambda+\mu)\partial_i] + \sum_k \partial_k(\mu\partial_k) + \rho\omega^2, \\
\mathfrak{L}_{ij} &= \partial_i(\lambda\partial_j) + \partial_j(\mu\partial_i), \quad i,j,k = x,y,z \; and \; j \neq i. \\
\mathbf{u} &= [u_x, u_y, u_z]^T.
\end{aligned} \tag{A.6}$$

By adding a delta function as source term, Green's function obeys a similar form, in frequency domain, it can be expressed as,

$$\boldsymbol{\mathfrak{L}}(\mathbf{r},\omega)\boldsymbol{\mathcal{G}}(\mathbf{r},\mathbf{r}_s,\omega) = -\delta(\mathbf{r}-\mathbf{r}_s) \tag{A.7}$$

Consider an elastic isotropic homogeneous medium as the background medium (which means, λ and μ do not vary with space locations), therefore, wave equation (Eq. A.7) can be simplified as,

$$\boldsymbol{\mathfrak{L}}_0(\mathbf{r},\omega)\boldsymbol{\mathcal{G}}_0(\mathbf{r},\mathbf{r}_s,\omega) = -\delta(\mathbf{r}-\mathbf{r}_s) \tag{A.8}$$

where,

$$\begin{aligned}
\mathfrak{L}_{0ii} &= (\lambda_0+\mu_0)\partial_i\partial_i + \mu_0\sum_k \partial_k\partial_k + \rho_0\omega^2, \\
\mathfrak{L}_{0ij} &= \lambda_0\partial_i\partial_j + \mu_0\partial_j\partial_i, \quad i,j,k = x,y,z \; and \; j \neq i.
\end{aligned} \tag{A.9}$$

with $\gamma = \lambda + 2\mu = \rho\alpha^2$ and $\mu = \rho\beta^2$ (α and β denote the P- and S-wave velocities in background medium), perturbations can be defined as,

$$\begin{aligned}
a_\rho &= \frac{\rho-\rho_0}{\rho} = \frac{\rho}{\rho_0} - 1 \approx \frac{\triangle\rho}{\rho} \\
a_\gamma &= \frac{\gamma-\gamma_0}{\rho} = \frac{\gamma}{\gamma_0} - 1 \approx \frac{\triangle\gamma}{\gamma} \\
a_\mu &= \frac{\mu-\mu_0}{\mu} = \frac{\mu}{\mu_0} - 1 \approx \frac{\triangle\mu}{\mu}
\end{aligned} \tag{A.10}$$

An elastic isotropic scattering potential is the difference of wave operator in real and reference mediums, which can be expressed as,

$$\boldsymbol{\mathcal{V}} = \mathfrak{L} - \mathfrak{L}_0 = \begin{pmatrix} \mathcal{V}_{xx} & \mathcal{V}_{xy} & \mathcal{V}_{xz} \\ \mathcal{V}_{yx} & \mathcal{V}_{yy} & \mathcal{V}_{yz} \\ \mathcal{V}_{zx} & \mathcal{V}_{zy} & \mathcal{V}_{zz} \end{pmatrix} \tag{A.11}$$

where,

$$\begin{aligned}\mathcal{V}_{ii} &= \rho_0\big[\omega^2 a_\rho + \alpha_0^2\partial_i(a_\gamma\partial_i) + \beta_0^2\sum_{j\neq i}\partial_j(a_\mu\partial_j)\big], \quad i,j = x,y,z;\\ \mathcal{V}_{ij} &= \rho_0\big[\alpha_0^2\partial_i(a_\gamma\partial_j) - 2\beta_0^2\partial_i(a_\mu\partial_j) + \beta_0^2\partial_j(a_\mu\partial_i)\big], \quad j\neq i.\end{aligned} \tag{A.12}$$

A.2 Diagonalization of wave operator and Green Function

In background (elastic, isotropic, and homogeneous) medium, with body force $\boldsymbol{\mathcal{F}}$ included, Eq.(A.4) can be simplified as,

$$(\lambda+\mu)\nabla(\nabla\cdot\vec{\mathbf{u}}) + \mu\nabla^2\vec{\mathbf{u}} + \boldsymbol{\mathcal{F}} + \rho\omega^2\mathbf{u} = 0 \tag{A.13}$$

Helmholtz's theorem states that any well-defined vector can be decomposed as the sum of a curl-free component and a divergence-free component. Therefore, we can rewrite the particle displacement $\mathbf{u}$ and the body force $\boldsymbol{\mathcal{F}}$ as,

$$\begin{aligned}\mathbf{u} &= \nabla\boldsymbol{\phi} + \nabla\times\boldsymbol{\psi}\\ \boldsymbol{\mathcal{F}} &= \nabla\boldsymbol{\Phi} + \nabla\times\boldsymbol{\Psi}\end{aligned} \tag{A.14}$$

where, $\boldsymbol{\phi}$ and $\boldsymbol{\Phi}$ are scalar potentials, $\boldsymbol{\psi}$ and $\boldsymbol{\Psi}$ are vector potentials.

Substitute decompositions of displacement and body force into equation (A.13) and do the math, we have,

$$\nabla[(\lambda+2\mu)\nabla^2\boldsymbol{\phi} + \boldsymbol{\Phi} + \rho\omega^2\boldsymbol{\phi}] + \nabla\times[\mu\nabla^2\boldsymbol{\psi} + \boldsymbol{\Psi} + \rho\omega^2\boldsymbol{\psi}] = 0 \tag{A.15}$$

P- or S-wave equation can be obtained, by taking a divergence or a curl of equation (A.15), respectively. Therefore, if we define a partial derivatives matrix $\boldsymbol{\Pi}$ (following the notation demonstrated by Stolt and Weglein (2012)), including a divergence and a curl, which is expressed as,

$$\boldsymbol{\Pi} = \begin{pmatrix}\nabla\cdot\\ \nabla\times\end{pmatrix} = \begin{pmatrix}\partial_x & \partial_y & \partial_z\\ 0 & -\partial_z & \partial_y\\ \partial_z & 0 & -\partial_x\\ -\partial_y & \partial_x & 0\end{pmatrix} \tag{A.16}$$

Then P- and S-wave components can also be separated by acting the derivatives matrix on the particle displacement,

$$\begin{pmatrix} \boldsymbol{\varphi}_P \\ \boldsymbol{\varphi}_S \end{pmatrix} = \boldsymbol{\Pi}\mathbf{u} = \begin{pmatrix} \nabla \cdot \mathbf{u} \\ \nabla \times \mathbf{u} \end{pmatrix} = \begin{pmatrix} \partial_x u_x + \partial_y u_y + \partial_z u_z \\ \partial_y u_z - \partial_z u_y \\ \partial_z u_x - \partial_x u_z \\ \partial_x u_y - \partial_y u_x \end{pmatrix} = \begin{pmatrix} \nabla \cdot \mathbf{u} \\ (\nabla \times \mathbf{u})_x \\ (\nabla \times \mathbf{u})_y \\ (\nabla \times \mathbf{u})_z \end{pmatrix} \tag{A.17}$$

Beyond that, the inverse of diagonal matrix can be calculated by its transpose by pre-multiplied an inverse Laplacian operator (See in Appendix B). In equation, it's shown as,

$$\boldsymbol{\Pi}^{-1} = \nabla^{-2}\boldsymbol{\Pi}^T \tag{A.18}$$

Stolt and Weglein (2012) also indicated that the wave operator can be diagonalized into P- and S-wave operators by pre-multiplying the partial derivatives matrix and post-multiplying its inverse. Formally,

$$\mathfrak{L}_{0D} = \boldsymbol{\Pi}\mathfrak{L}_0\boldsymbol{\Pi}^{-1} = \begin{pmatrix} \mathfrak{L}_{0P} & 0 & 0 & 0 \\ 0 & \mathfrak{L}_{0S} & 0 & 0 \\ 0 & 0 & \mathfrak{L}_{0S} & 0 \\ 0 & 0 & 0 & \mathfrak{L}_{0S} \end{pmatrix} \tag{A.19}$$

where, $\mathfrak{L}_P$ and $\mathfrak{L}_S$ are P- and S-wave operators, written as,

$$\begin{aligned} \mathfrak{L}_{0P} &= (\lambda + 2\mu)\nabla^2 + \rho\omega^2 \\ \mathfrak{L}_{0S} &= \mu\nabla^2 + \rho\omega^2 \end{aligned} \tag{A.20}$$

With the diagonalized wave operator $\mathfrak{L}_{0D}$, the wave equation for an isotropic elastic medium becomes,

$$\mathfrak{L}_{0D}\boldsymbol{\Pi}\mathbf{u} = \begin{pmatrix} \mathfrak{L}_P\boldsymbol{\varphi}_P \\ \mathfrak{L}_S\boldsymbol{\varphi}_S \end{pmatrix} = 0 \tag{A.21}$$

Similar equations included diagonalized Green's function for real and reference medium can be expressed as,

$$\boldsymbol{\mathfrak{L}}_D(\mathbf{r},\omega)\boldsymbol{\mathcal{G}}_D(\mathbf{r},\mathbf{r}_s,\omega) = -\delta(\mathbf{r}-\mathbf{r}_s) \tag{A.22a}$$

$$\boldsymbol{\mathfrak{L}}_{0D}(\mathbf{r},\omega)\boldsymbol{\mathcal{G}}_{0D}(\mathbf{r},\mathbf{r}_s,\omega) = -\delta(\mathbf{r}-\mathbf{r}_s) \tag{A.22b}$$

where,

$$\boldsymbol{\mathcal{G}}_D = \boldsymbol{\Pi}\boldsymbol{\mathcal{G}}\boldsymbol{\Pi}^{-1} = \begin{pmatrix} \mathcal{G}_{PP} & \mathcal{G}_{PS_x} & \mathcal{G}_{PS_y} & \mathcal{G}_{PS_z} \\ \mathcal{G}_{S_xP} & \mathcal{G}_{S_xS_x} & \mathcal{G}_{S_xS_y} & \mathcal{G}_{S_xS_z} \\ \mathcal{G}_{S_yP} & \mathcal{G}_{S_yS_x} & \mathcal{G}_{S_yS_y} & \mathcal{G}_{S_yS_z} \\ \mathcal{G}_{S_zP} & \mathcal{G}_{S_zS_x} & \mathcal{G}_{S_zS_y} & \mathcal{G}_{S_zS_z} \end{pmatrix} \tag{A.23a}$$

$$\boldsymbol{\mathcal{G}}_{0D} = \boldsymbol{\Pi}\boldsymbol{\mathcal{G}}_0\boldsymbol{\Pi}^{-1} = \begin{pmatrix} \mathcal{G}_{0P} & 0 & 0 & 0 \\ 0 & \mathcal{G}_{0S_x} & 0 & 0 \\ 0 & 0 & \mathcal{G}_{0S_y} & 0 \\ 0 & 0 & 0 & \mathcal{G}_{0S_z} \end{pmatrix} \tag{A.23b}$$

Equations A.23 indicate that,the Green's function can be rewritten into 4×4 matrix with respect to P- and S-wave components, by applying the transformation $\boldsymbol{\Pi}\boldsymbol{\mathcal{G}}\boldsymbol{\Pi}^{-1}$, which also works for the propagating operator (euqation A.19). For inhomogeneous isotropic elastic (real) medium, the diagonal elements of $\boldsymbol{\mathcal{G}}_D$ correspond to Green's functions of PP and $x-, y-, z-$ components of SS waves, and off-diagonal terms relate to Green's functions of converted waves from one to another. For homogeneous isotropic elastic (reference) medium, the upper left diagonal term of $\boldsymbol{\mathcal{G}}_{0D}$ is the Green's function for PP-wave, and other diagonal terms correspond to $x-, y-, z-$ components of Green's function for SS wave, and off-diagonal terms are zeros.

A.3 Rotation of wave operator, Green Function, and elastic scattering potential

One of the disadvantage of the diagonal matrix $\mathbf{\Pi}$ is that it maps a 3D vector into a 4D space with only three independent dimensions present. It does separate P-wave successfully from S-wave components, but it does not work for SV- and SH-waves. To decompose the elastic scattering potential into P-, SH-, SV-modes, Stolt and Weglein (2012) introduced rotation matrices by rotating S-wave components to a local system in which the third (longitudinal) S-wave component is zero. Before the rotation, we have to rewrite the diagonal matrix in terms of P- and S-wave wavenumbers, which is expressed as,

$$\mathbf{\Pi} \rightarrow \mathbf{\Pi}_r = \mathrm{i} \begin{pmatrix} k_{Prx} & k_{Pry} & k_{Prz} \\ 0 & -k_{Srz} & k_{Sry} \\ k_{Srz} & 0 & -k_{Srx} \\ -k_{Sry} & k_{Srx} & 0 \end{pmatrix} = \mathrm{i} \begin{pmatrix} \boldsymbol{k}_{Pr}\boldsymbol{\cdot}^T \\ \boldsymbol{k}_{Sr}\times \end{pmatrix} \tag{A.24}$$

and

$$\begin{aligned} \mathbf{\Pi}^{-1} \rightarrow (\mathbf{\Pi}^{-1})_i &= \frac{-\mathrm{i}}{\omega^2} \begin{pmatrix} \alpha_0^2 k_{Pix} & 0 & \beta_0^2 k_{Siz} & -\beta_0^2 k_{Siy} \\ \alpha_0^2 k_{Piy} & -\beta_0^2 k_{Siz} & 0 & \beta_0^2 k_{Six} \\ \alpha_0^2 k_{Piz} & \beta_0^2 k_{Siy} & -\beta_0^2 k_{Six} & 0 \end{pmatrix} \\ &= \frac{-\mathrm{i}}{\omega^2} \begin{bmatrix} \alpha_0^2 \boldsymbol{k}_{Pi}\boldsymbol{\cdot} & \beta_0^2 (\boldsymbol{k}_{Si}\times)^T \end{bmatrix} \end{aligned} \tag{A.25}$$

where,

$$\begin{aligned} k_{Pr} = k_{Pi} &= \frac{\omega}{\alpha_0} \\ k_{Sr} = k_{Si} &= \frac{\omega}{\beta_0} \end{aligned} \tag{A.26}$$

Correspondingly, 4×4 rotation matrices can be defined for incident and reflected waves,

$$\boldsymbol{E}_i = \begin{pmatrix} 1 & 0 & 0 & 0 \\ 0 & e_{SVix} & e_{SViy} & e_{SViz} \\ 0 & -e_{SHx} & -e_{SHy} & -e_{SHz} \end{pmatrix} = \begin{pmatrix} 1 & \mathbf{0}^T \\ 0 & \hat{\boldsymbol{e}}_{SVi}^T \\ 0 & -\hat{\boldsymbol{e}}_{SH}^T \end{pmatrix} \tag{A.27}$$

and

$$\boldsymbol{E}_r = \begin{pmatrix} 1 & 0 & 0 & 0 \\ 0 & e_{SVrx} & e_{SVry} & e_{SVrz} \\ 0 & -e_{SHx} & -e_{SHy} & -e_{SHz} \end{pmatrix} = \begin{pmatrix} 1 & \mathbf{0}^T \\ 0 & \hat{\boldsymbol{e}}_{SVr}^T \\ 0 & -\hat{\boldsymbol{e}}_{SH}^T \end{pmatrix} \tag{A.28}$$

also, we have,

$$\boldsymbol{E}\boldsymbol{E}^T = \begin{pmatrix} 1 & 0 & 0 \\ 0 & 1 & 0 \\ 0 & 0 & 1 \end{pmatrix} \tag{A.29}$$

and

$$\boldsymbol{E}^T \boldsymbol{E}\boldsymbol{\Pi} = \boldsymbol{\Pi} \tag{A.30}$$

which states that the inverse of $\boldsymbol{E}$ equals to its transpose.

After applied the rotation matrix, the $x-, y-, z-$ components of S-wave are decomposed into SH- and SV-modes. Invoking the orthogonality relations, the combined diagonal and rotation matrices for incident wave,

$$(\boldsymbol{\Pi}^{-1})_i \boldsymbol{E}_i^{-1} = -\mathrm{i} \begin{bmatrix} \dfrac{\alpha_0^2}{\omega^2}\boldsymbol{k}_{Pi} & \dfrac{\beta_0}{\omega}\hat{\boldsymbol{e}}_{SH} & \dfrac{\beta_0}{\omega}\hat{\boldsymbol{e}}_{SVi} \end{bmatrix} \tag{A.31}$$

for reflected wave,

$$\boldsymbol{E}_r \boldsymbol{\Pi}_r = \mathrm{i} \begin{bmatrix} \boldsymbol{k}_{Pr}^T \\ \dfrac{\omega}{\beta_0}\hat{\boldsymbol{e}}_{SH}^T \\ \dfrac{\omega}{\beta_0}\hat{\boldsymbol{e}}_{SVr}^T \end{bmatrix} \tag{A.32}$$

Therefore, we have,

$$\boldsymbol{E}_r \boldsymbol{\Pi}_r (\boldsymbol{\Pi}^{-1})_i \boldsymbol{E}_i^{-1} = \mathbf{I} \tag{A.33}$$

where, $\mathbf{I}$ is an identity matrix.

In conclusion, the wave equation containing Green's function in P-, SH-, SV-modes can be expressed as,

$$\boldsymbol{\mathcal{L}}(\mathbf{r}, \omega)\, \boldsymbol{G}(\mathbf{r}, \mathbf{r}_s, \omega) = -\delta(\mathbf{r} - \mathbf{r}_s) \tag{A.34a}$$

$$\boldsymbol{\mathcal{L}}_0(\mathbf{r}, \omega)\, \boldsymbol{G}_0(\mathbf{r}, \mathbf{r}_s, \omega) = -\delta(\mathbf{r} - \mathbf{r}_s) \tag{A.34b}$$

where,

$$\boldsymbol{\mathcal{L}} = \boldsymbol{E}_r \boldsymbol{\mathfrak{L}}_D \boldsymbol{E}_i^{-1} = \boldsymbol{E}_r \boldsymbol{\Pi}_r \boldsymbol{\mathfrak{L}} (\boldsymbol{\Pi}^{-1})_i \boldsymbol{E}_i^{-1} \tag{A.35a}$$

$$\boldsymbol{\mathcal{L}}_0 = \boldsymbol{E}_r \boldsymbol{\mathfrak{L}}_{0D} \boldsymbol{E}_i^{-1} = \boldsymbol{E}_r \boldsymbol{\Pi}_r \boldsymbol{\mathfrak{L}}_0 (\boldsymbol{\Pi}^{-1})_i \boldsymbol{E}_i^{-1} \tag{A.35b}$$

and

$$\mathbf{G} = \boldsymbol{E}_r \boldsymbol{\mathcal{G}}_D \boldsymbol{E}_i^{-1} = \boldsymbol{E}_r \boldsymbol{\Pi}_r \boldsymbol{\mathcal{G}} (\boldsymbol{\Pi}^{-1})_i \boldsymbol{E}_i^{-1} = \begin{pmatrix} \mathbf{G}_{PP} & \mathbf{G}_{PSH} & \mathbf{G}_{PSV} \\ \mathbf{G}_{SHP} & \mathbf{G}_{SHSH} & \mathbf{G}_{SHSV} \\ \mathbf{G}_{SVP} & \mathbf{G}_{SVSH} & \mathbf{G}_{SVSV} \end{pmatrix} \tag{A.36a}$$

$$\mathbf{G}_0 = \boldsymbol{E}_r \boldsymbol{\mathcal{G}}_{0D} \boldsymbol{E}_i^{-1} = \boldsymbol{E}_r \boldsymbol{\Pi}_r \boldsymbol{\mathcal{G}}_0 (\boldsymbol{\Pi}^{-1})_i \boldsymbol{E}_i^{-1} = \begin{pmatrix} \mathbf{G}_{0P} & 0 & 0 \\ 0 & \mathbf{G}_{0S} & 0 \\ 0 & 0 & \mathbf{G}_{0S} \end{pmatrix} \tag{A.36b}$$

Also, for the scattering potential, a similar form can be achieved,

$$\mathbf{V} = \boldsymbol{E}_r \boldsymbol{\Pi}_r \boldsymbol{\mathcal{V}} (\boldsymbol{\Pi}^{-1})_i \boldsymbol{E}_i^{-1} = \begin{pmatrix} \mathbf{V}_{PP} & \mathbf{V}_{PSH} & \mathbf{V}_{PSV} \\ \mathbf{V}_{SHP} & \mathbf{V}_{SHSH} & \mathbf{V}_{SHSV} \\ \mathbf{V}_{SVP} & \mathbf{V}_{SVSH} & \mathbf{V}_{SVSV} \end{pmatrix} \tag{A.37}$$

Appendix B

Derivation of diagonalization operators and its properties

Define a partial derivative matrix,

$$\mathbf{\Pi} = \begin{pmatrix} \nabla\cdot \\ \nabla\times \end{pmatrix} = \begin{pmatrix} \partial_x & \partial_y & \partial_z \\ 0 & -\partial_z & \partial_y \\ \partial_z & 0 & -\partial_x \\ -\partial_y & \partial_x & 0 \end{pmatrix} \tag{B.1}$$

By pre-multiplying its transpose, produces the Laplacian ∇^2 times a 3D unit operator,

$$\mathbf{\Pi}^T\mathbf{\Pi} = \begin{pmatrix} \nabla^T\cdot & -\nabla\times \end{pmatrix} \begin{pmatrix} \nabla\cdot \\ \nabla\times \end{pmatrix} = [\nabla(\nabla\cdot) - \nabla\times(\nabla\times)]\mathbf{I} = \begin{pmatrix} \nabla^2 & 0 & 0 \\ 0 & \nabla^2 & 0 \\ 0 & 0 & \nabla^2 \end{pmatrix} \tag{B.2}$$

If $\mathbf{\Pi}$ is post-multiplied by its transpose,

$$\begin{aligned} \mathbf{\Pi}\,\mathbf{\Pi}^T &= \begin{pmatrix} \nabla\cdot \\ \nabla\times \end{pmatrix} \begin{pmatrix} \nabla^T\cdot & -\nabla\times \end{pmatrix} = \begin{pmatrix} \nabla^2 & \mathbf{0} \\ \mathbf{0} & -\nabla\times(\nabla\times) \end{pmatrix} \\ &= \begin{pmatrix} \nabla^2 & 0 & 0 & 0 \\ 0 & \partial_y^2+\partial_z^2 & -\partial_y\partial_x & -\partial_z\partial_x \\ 0 & -\partial_x\partial_y & \partial_x^2+\partial_z^2 & -\partial_z\partial_y \\ 0 & -\partial_x\partial_z & -\partial_y\partial_z & \partial_x^2+\partial_y^2 \end{pmatrix} \end{aligned} \tag{B.3}$$

Operating on the P- and S-wave components vector, we have,

$$\begin{aligned}\mathbf{\Pi}\ \mathbf{\Pi}^T \begin{pmatrix} \boldsymbol{\varphi}_P \\ \boldsymbol{\varphi}_S \end{pmatrix} &= \begin{pmatrix} \nabla^2 & \mathbf{0} \\ \mathbf{0} & -\nabla \times (\nabla \times) \end{pmatrix} \begin{pmatrix} \boldsymbol{\varphi}_P \\ \boldsymbol{\varphi}_S \end{pmatrix} \\ &= \begin{pmatrix} \nabla^2 \boldsymbol{\varphi}_P \\ \nabla^2 \boldsymbol{\varphi}_S - \nabla(\nabla \cdot \boldsymbol{\varphi}_S) \end{pmatrix}\end{aligned} \tag{B.4}$$

Here, $\boldsymbol{\varphi}_S = \nabla \times \mathbf{u}$, which means $\nabla(\nabla \cdot \boldsymbol{\varphi}_S) = 0$. Therefore, under this condition, the equation (B.4) can be written as,

$$\mathbf{\Pi}\ \mathbf{\Pi}^T \begin{pmatrix} \boldsymbol{\varphi}_P \\ \boldsymbol{\varphi}_S \end{pmatrix} = \nabla^2 \begin{pmatrix} \boldsymbol{\varphi}_P \\ \boldsymbol{\varphi}_S \end{pmatrix} \tag{B.5}$$

This implies that, under some assumptions, the inverse of partial derivative matrix can be written as the multiplication of its transpose with the inverse of the Laplacian,

$$\mathbf{\Pi}^{-1} = \nabla^{-2} \mathbf{\Pi}^T \tag{B.6}$$

Define P- and S-wave operators, $\mathfrak{L}_P$ and $\mathfrak{L}_S$ satisfy,

$$\begin{aligned}\mathfrak{L}_{0P} &= (\lambda + 2\mu)\nabla^2 + \rho\omega^2 \\ \mathfrak{L}_{0S} &= \mu\nabla^2 + \rho\omega^2\end{aligned} \tag{B.7}$$

Using P- and S-wave operators, the wave operator for a homogeneous isotropic elastic medium $\mathbf{\mathfrak{L}}_0(\mathbf{x}, \omega)$, which means derivatives of λ and μ can be neglected, can be rewritten as,

$$\mathbf{\mathfrak{L}}_0 = \begin{pmatrix} (\lambda+\mu)\partial_x^2 + \mathbf{\mathfrak{L}}_{0S} & (\lambda+\mu)\partial_y\partial_x & (\lambda+\mu)\partial_z\partial_x \\ (\lambda+\mu)\partial_x\partial_y & (\lambda+\mu)\partial_y^2 + \mathbf{\mathfrak{L}}_{0S} & (\lambda+\mu)\partial_z\partial_y \\ (\lambda+\mu)\partial_x\partial_z & (\lambda+\mu)\partial_y\partial_z & (\lambda+\mu)\partial_z^2 + \mathbf{\mathfrak{L}}_{0S} \end{pmatrix} \tag{B.8}$$

Therefore, we have,

$$\mathbf{\Pi\mathfrak{L}}_0 = \begin{pmatrix} \partial_x \mathbf{\mathfrak{L}}_{0P} & \partial_y \mathbf{\mathfrak{L}}_{0P} & \partial_z \mathbf{\mathfrak{L}}_{0P} \\ 0 & -\partial_z \mathbf{\mathfrak{L}}_{0S} & \partial_y \mathbf{\mathfrak{L}}_{0P} \\ \partial_z \mathbf{\mathfrak{L}}_{0S} & 0 & -\partial_z \mathbf{\mathfrak{L}}_{0S} \\ -\partial_y \mathbf{\mathfrak{L}}_{0S} & \partial_x \mathbf{\mathfrak{L}}_{0S} & 0 \end{pmatrix} \tag{B.9}$$

It is worth to note that, the right hand side of equation (B.9) can be considered as the multiplication of the diagonalized matrix and the operator $\mathbf{\Pi}$ as follow,

$$\begin{pmatrix} \partial_x \mathfrak{L}_{0P} & \partial_y \mathfrak{L}_{0P} & \partial_z \mathfrak{L}_{0P} \\ 0 & -\partial_z \mathfrak{L}_{0S} & \partial_y \mathfrak{L}_{0P} \\ \partial_z \mathfrak{L}_{0S} & 0 & -\partial_z \mathfrak{L}_{0S} \\ -\partial_y \mathfrak{L}_{0S} & \partial_x \mathfrak{L}_{0S} & 0 \end{pmatrix} = \mathfrak{L}_{0D} \mathbf{\Pi} \tag{B.10}$$

where,

$$\mathfrak{L}_{0D} = \begin{pmatrix} \mathfrak{L}_{0P} & 0 & 0 & 0 \\ 0 & \mathfrak{L}_{0S} & 0 & 0 \\ 0 & 0 & \mathfrak{L}_{0S} & 0 \\ 0 & 0 & 0 & \mathfrak{L}_{0S} \end{pmatrix} \tag{B.11}$$

Combine equation (B.9) and equation (B.10), which indicates the wave operator $\mathfrak{L}_0$ can be diagonalizable into P- and S-wave operators,

$$\mathfrak{L}_{0D} = \mathbf{\Pi} \mathfrak{L}_0 \mathbf{\Pi}^{-1} \tag{B.12}$$

Therefore, by pre-multiplying a partial derivative matrix, wave equation for an elastic isotropic homogeneous medium (equation A.5) is rewritten as,

$$\mathbf{\Pi} \mathfrak{L}_0 (\mathbf{\Pi}^{-1} \mathbf{\Pi}) \mathbf{u} = 0 \tag{B.13}$$

Replacing the displacement into the P- and S-wave components, the above equation can be expressed as,

$$\mathfrak{L}_{0D} \begin{pmatrix} \boldsymbol{\varphi}_P \\ \boldsymbol{\varphi}_S \end{pmatrix} = 0 \tag{B.14}$$

where, $\mathbf{\Pi u} = \begin{pmatrix} \boldsymbol{\varphi}_P \\ \boldsymbol{\varphi}_S \end{pmatrix}$.

One should note that the above transformation does not diagonalize the wave equation (Stolt and Weglein, 2012). However, the interpretation of the elements in separated P- and

S- wave components is still reasonable, where off-diagonal terms in $\mathfrak{L}_{0D}$ denote wave mode conversion from one to another.

Appendix C

3D Multicomponent (elastic) inverse scattering series internal multiple prediction algorithm

C.1 Elastic inverse scattering series decomposition

For an isotropic elastic medium, the wave field can be expressed as a background field adding perturbations. Considering the homogeneous isotropic elastic medium as the background, the Born series for an isotropic elastic medium can be written as,

$$\boldsymbol{\mathcal{G}} = \boldsymbol{\mathcal{G}}_0 + \boldsymbol{\mathcal{G}}_0\boldsymbol{\mathcal{V}}\boldsymbol{\mathcal{G}}_0 + \boldsymbol{\mathcal{G}}_0\boldsymbol{\mathcal{V}}\boldsymbol{\mathcal{G}}_0\boldsymbol{\mathcal{V}}\boldsymbol{\mathcal{G}}_0 + \boldsymbol{\mathcal{G}}_0\boldsymbol{\mathcal{V}}\boldsymbol{\mathcal{G}}_0\boldsymbol{\mathcal{V}}\boldsymbol{\mathcal{G}}_0\boldsymbol{\mathcal{V}}\boldsymbol{\mathcal{G}}_0 + ... \tag{C.1}$$

As discussed above, the Green's Function can be devised into a 3×3 matrix corresponded to P-, SV-, and SH-wave modes with pre- or post-multiplied diagonal matrix $\mathbf{\Pi}$ and rotation matrix $\boldsymbol{E}$. Therefore, replacing the Green's function $\boldsymbol{\mathcal{G}}$ and $\boldsymbol{\mathcal{G}}_0$ in Eq. (C.1), Born series can be rewritten into P-, SH-, and SV-modes,

$$\begin{aligned}(\mathbf{\Pi}^{-1})_i\boldsymbol{E}_i^{-1}\mathbf{G}\boldsymbol{E}_r\mathbf{\Pi}_r = {} & (\mathbf{\Pi}^{-1})_i\boldsymbol{E}_i^{-1}\mathbf{G}_0\boldsymbol{E}_r\mathbf{\Pi}_r + (\mathbf{\Pi}^{-1})_i\boldsymbol{E}_i^{-1}\mathbf{G}_0\boldsymbol{E}_r\mathbf{\Pi}_r\boldsymbol{\mathcal{V}}(\mathbf{\Pi}^{-1})_i\boldsymbol{E}_i^{-1}\mathbf{G}_0\boldsymbol{E}_r\mathbf{\Pi}_r \\ & + (\mathbf{\Pi}^{-1})_i\boldsymbol{E}_i^{-1}\mathbf{G}_0\boldsymbol{E}_r\mathbf{\Pi}_r\boldsymbol{\mathcal{V}}(\mathbf{\Pi}^{-1})_i\boldsymbol{E}_i^{-1}\mathbf{G}_0\boldsymbol{E}_r\mathbf{\Pi}_r\boldsymbol{\mathcal{V}}(\mathbf{\Pi}^{-1})_i\boldsymbol{E}_i^{-1}\mathbf{G}_0\boldsymbol{E}_r\mathbf{\Pi}_r \\ & + ...\end{aligned} \tag{C.2}$$

Combining the relationship between diagonal matrix $\mathbf{\Pi}$ and rotation matrix $\boldsymbol{E}$ (Eq. A.33), pre-multiplying $\boldsymbol{E}_r\mathbf{\Pi}_r$ and post-multiplied by $(\mathbf{\Pi}^{-1})_i\boldsymbol{E}_i^{-1}$, applying equation A.37 to transform the elastic scattering potential into P-, SH-, SV-wave modes, equation C.2 can be simplified as,

$$\mathbf{G} = \mathbf{G}_0 + \mathbf{G}_0\mathbf{V}\mathbf{G}_0 + \mathbf{G}_0\mathbf{V}\mathbf{G}_0\mathbf{V}\mathbf{G}_0 + \mathbf{G}_0\mathbf{V}\mathbf{G}_0\mathbf{V}\mathbf{G}_0\mathbf{V}\mathbf{G}_0 + ... \tag{C.3}$$

Recall the wave equation for inhomogeneous isotropic elastic medium, containing source term, which can be expressed as,

$$\mathfrak{L}(\mathbf{r},\omega)\mathbf{u}(\mathbf{r},\omega) = \mathbf{f} \tag{C.4}$$

The displacement field will be decomposed into P-, SH-, SV-wave modes by pre-multiplying $\boldsymbol{E}_r\boldsymbol{\Pi}_r$,

$$\begin{bmatrix} \boldsymbol{\varphi}_P \\ \boldsymbol{\varphi}_{SH} \\ \boldsymbol{\varphi}_{SV} \end{bmatrix} = \boldsymbol{E}_r\boldsymbol{\Pi}_r\mathbf{u} = \boldsymbol{E}_r\boldsymbol{\Pi}_r\boldsymbol{\mathcal{G}}\mathbf{f} = \mathbf{G}\boldsymbol{E}_r\boldsymbol{\Pi}_r\mathbf{f} = \mathbf{G}\mathbf{F} \tag{C.5}$$

where, $\mathbf{F} = \boldsymbol{E}_r\boldsymbol{\Pi}_r\mathbf{f} = [1,0,0]^T$ if the incidence is a spike of P-wave only.

Incorporating equation C.5 and equation C.3, the separated scattering wavefield can be rewritten as, in terms of background and perturbations,

$$\boldsymbol{D}\mathbf{F} = (\mathbf{G}-\mathbf{G}_0)\mathbf{F} = \mathbf{G}_0\mathbf{V}\mathbf{G}_0\mathbf{F} + \mathbf{G}_0\mathbf{V}\mathbf{G}_0\mathbf{V}\mathbf{G}_0\mathbf{F} + \mathbf{G}_0\mathbf{V}\mathbf{G}_0\mathbf{V}\mathbf{G}_0\mathbf{V}\mathbf{G}_0\mathbf{F} + ... \tag{C.6}$$

with its matrix form,

$$\begin{aligned}
&\begin{bmatrix} \boldsymbol{D}_{PP} & \boldsymbol{D}_{PSH} & \boldsymbol{D}_{PSV} \\ \boldsymbol{D}_{SHP} & \boldsymbol{D}_{SHSH} & \boldsymbol{D}_{SHSV} \\ \boldsymbol{D}_{SVP} & \boldsymbol{D}_{SVSH} & \boldsymbol{D}_{SVSV} \end{bmatrix}\mathbf{F} \\
&= \begin{bmatrix} \mathbf{G}_{0P} & 0 & 0 \\ 0 & \mathbf{G}_{0S} & 0 \\ 0 & 0 & \mathbf{G}_{0S} \end{bmatrix}\begin{bmatrix} \mathbf{V}_{PP} & \mathbf{V}_{PSH} & \mathbf{V}_{PSV} \\ \mathbf{V}_{SHP} & \mathbf{V}_{SHSH} & \mathbf{V}_{SHSV} \\ \mathbf{V}_{SVP} & \mathbf{V}_{SVSH} & \mathbf{V}_{SVSV} \end{bmatrix}\begin{bmatrix} \mathbf{G}_{0P} & 0 & 0 \\ 0 & \mathbf{G}_{0S} & 0 \\ 0 & 0 & \mathbf{G}_{0S} \end{bmatrix}\mathbf{F} \\
&+ \begin{bmatrix} \mathbf{G}_{0P} & 0 & 0 \\ 0 & \mathbf{G}_{0S} & 0 \\ 0 & 0 & \mathbf{G}_{0S} \end{bmatrix}\begin{bmatrix} \mathbf{V}_{PP} & \mathbf{V}_{PSH} & \mathbf{V}_{PSV} \\ \mathbf{V}_{SHP} & \mathbf{V}_{SHSH} & \mathbf{V}_{SHSV} \\ \mathbf{V}_{SVP} & \mathbf{V}_{SVSH} & \mathbf{V}_{SVSV} \end{bmatrix}\begin{bmatrix} \mathbf{G}_{0P} & 0 & 0 \\ 0 & \mathbf{G}_{0S} & 0 \\ 0 & 0 & \mathbf{G}_{0S} \end{bmatrix} \\
&\begin{bmatrix} \mathbf{V}_{PP} & \mathbf{V}_{PSH} & \mathbf{V}_{PSV} \\ \mathbf{V}_{SHP} & \mathbf{V}_{SHSH} & \mathbf{V}_{SHSV} \\ \mathbf{V}_{SVP} & \mathbf{V}_{SVSH} & \mathbf{V}_{SVSV} \end{bmatrix}\begin{bmatrix} \mathbf{G}_{0P} & 0 & 0 \\ 0 & \mathbf{G}_{0S} & 0 \\ 0 & 0 & \mathbf{G}_{0S} \end{bmatrix}\mathbf{F} + ...
\end{aligned} \tag{C.7}$$

In an effort to avoid confusion and awkward phrasing, we rewrite the equation C.7 using subscripts,

$$D^{ij} = G_0^i V_{ij} G_{0j} + G_0^i V_{ik} G_0^k V_{kj} G_{0j} + G_0^i V_{ik} G_0^k V_{kl} G_0^l V_{lj} G_{0j} + ... \tag{C.8}$$

where, the subscripts denote P-, SH-, SV- components for wave propagation or scattering. D^{ij} is an specified element of decomposed measured data related to i, j. And i is the wave mode for reflected wave or on receiver coordinate. j is the mode for incident wave, which means $j = P$ if the incidence is P-wave only. The wave propagation through perturbation mode for an elastic medium is shown in Figure. C.1.

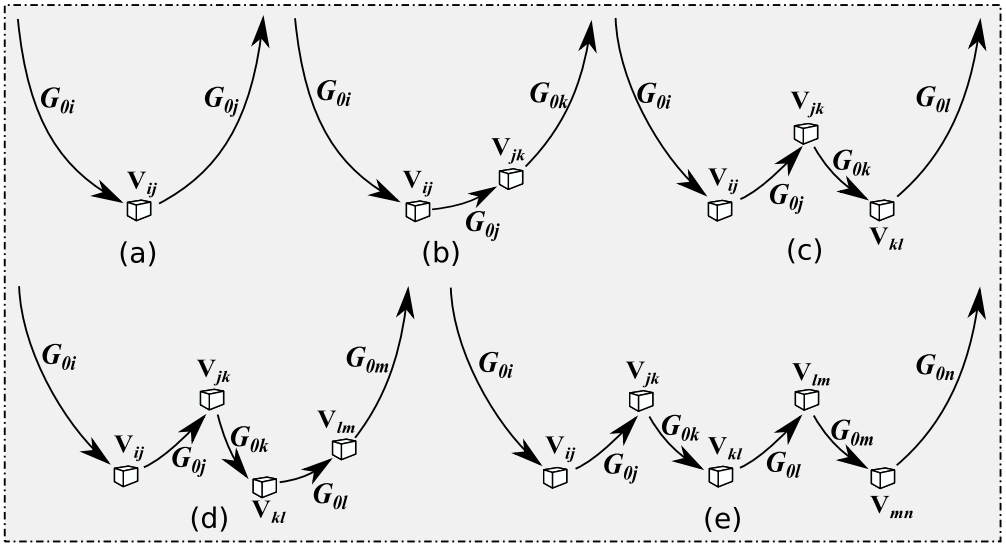

Figure C.1: Wave propagation in perturbation mode. The subscripts (i, j, k, l, m, n) denote the wave mode, $\in \{P, SH, SV\}$.

Similar with acoustic inverse scattering, the scattering potential can be expanded into series by orders,

$$V = V^{(1)} + V^{(2)} + V^{(3)} + ... \tag{C.9}$$

Substitute this expansion (Eq. C.9) into subscripted Born series (Eq. C.8), and equate

like orders, we have,

$$D^{ij} = G_0^i V_1^{ij} G_{0j}, \tag{C.10a}$$

$$0 = G_0^i V_2^{ij} G_{0j} + G_0^i V_1^{ik} G_0^k V_1^{kj} G_{0j}, \tag{C.10b}$$

$$0 = G_0^i V_3^{ij} G_{0j} + G_0^i V_2^{ik} G_0^k V_1^{kj} G_{0j} + G_0^i V_1^{ik} G_0^k V_2^{kj} G_{0j} + G_0^i V_1^{ik} G_0^k V_1^{kl} G_0^l V_1^{lj} G_{0j}, \tag{C.10c}$$

$$\vdots$$

C.2 Elastic internal multiple prediction algorithm

Based on Eq. (C.10a), the first-order of elastic scattering potential can be delineated by the decomposed measured data D^{ij} and Green's function for pure P- or S-waves. Recall 3D Green's function for pure P- or S-wave,

$$G_0^i(k_{x_1}^i, k_{y_1}^i, z_1, x_2, y_2, z_2, \omega) = \frac{e^{-\mathrm{i}(k_{x_1}^i x_2 + k_{y_1}^i y_2)} e^{\mathrm{i}\nu_1^i |z_1 - z_2|}}{\mathrm{i}2\nu_1^i} \tag{C.11a}$$

$$G_0^i(x_1, y_1, z_1, k_{x_2}^i, k_{y_2}^i, z_2, \omega) = \frac{e^{\mathrm{i}(k_{x_2}^i x_1 + k_{y_2}^i y_1)} e^{\mathrm{i}\nu_2^i |z_2 - z_1|}}{\mathrm{i}2\nu_2^i} \tag{C.11b}$$

with

$$\nu_1^i = \sqrt{\frac{\omega^2}{(c_0^i)^2} - (k_{x_1}^i)^2 - (k_{y_1}^i)^2}$$

where, $k_{x_1}^i$ and $k_{y_1}^i$ are x and y components of wavenumber, ν_1^i is the vertical component of wavenumber. The subscript 1 means the side of location, i.e., $k_{x_1}^i$ is the x component of wavenumber corresponding to location (x_1, y_1, z_1). c_0^i is the velocity depending on the wave mode i, and $i \in \{P, SH, SV\}$.

Therefore, take an inverse Fourier transform over k_x and k_y, the space-frequency domain 3D Green's function from one location (x_2, y_2, z_2) to another (x_1, y_1, z_1) can be written as,

$$G_0^i(x_1, y_1, z_1, x_2, y_2, z_2, \omega) = \frac{1}{(2\pi)^2} \iint_{-\infty}^{+\infty} \frac{e^{\mathrm{i}k_{x_2}^i (x_1 - x_2)} e^{\mathrm{i}k_{y_2}^i (y_1 - y_2)} e^{\mathrm{i}\nu_2^i |z_1 - z_2|}}{\mathrm{i}2\nu_2^i} \mathrm{d}k_{x_2}^i \mathrm{d}k_{y_2}^i \tag{C.12}$$

Further analysis of Eq. (C.12) indicates that Green's function can be considered as a

superposition of weighted plane wave solution, as follow,

$$\begin{aligned} &G_0^i(x_g, y_g, z_g, x_s, y_s, z_s, \omega) \\ &= \frac{1}{(2\pi)^2} \iint_{-\infty}^{+\infty} \frac{e^{-\mathrm{i}(k_{x_s}^i x_s + k_{y_s}^i y_s)}}{\mathrm{i}2\nu_s^i} \phi_0^i(x_g, y_g, z_g, k_{x_s}^i, k_{y_s}^i, z_s, \omega) \mathrm{d}k_{x_s}^i \mathrm{d}k_{y_s}^i \end{aligned} \tag{C.13}$$

where,

$$\phi_0^i(x_g, y_g, z_g, k_{x_s}^i, k_{y_s}^i . z_s, \omega) = e^{\mathrm{i}(k_{x_s}^i x_g + k_{y_s}^i y_g + \nu_s^i |z_g - z_s|)} \tag{C.14}$$

Then we have, $\phi_0^i(x_g, y_g, z_g, k_{x_s}^i, k_{y_s}^i . z_s, \omega) = \mathrm{i}2\nu_s^i G_0^i(x_g, z_g, k_{x_s}^i, k_{y_s}^i, z_s, \omega)$. Substitute this change into the inverse scattering series using reversion (Eq.C.10),

$$b_1^{ij} = G_0^i V_1^{ij} \phi_0^j, \tag{C.15a}$$

$$0 = G_0^i V_2^{ij} \phi_0^j + G_0^i V_1^{ik} G_0^k V_1^{kj} \phi_0^j, \tag{C.15b}$$

$$0 = G_0^i V_3^{ij} \phi_0^j + G_0^i V_2^{ik} G_0^k V_1^{kj} \phi_0^j + G_0^i V_1^{ik} G_0^k V_2^{kj} \phi_0^j + G_0^i V_1^{ik} G_0^k V_1^{kl} G_0^l V_1^{lj} \phi_0^j, \tag{C.15c}$$

$$\vdots$$

where, b_1^{ij} is the weighted decomposed measured data, and can be calculated by $b_1^{ij}(k_{x_g}^i, k_{y_g}^i, k_{x_s}^j, k_{y_s}^j, \omega) = \mathrm{i}2\nu_s^j D^{ij}(k_{x_g}^i, k_{y_g}^i, k_{x_s}^j, k_{y_s}^j, \omega)$ and ν_s^j depends on the mode of wave which is determined by j, and $j \in \{P, SH, SV\}$.

Substitute Green's function into equation C.15a, the first-order of elastic scattering potential V_{ij} can be expressed in terms of the weighted decomposed measured data b_1^{ij}. Expand equation C.15a, we have,

$$\begin{aligned} &b_1^{ij}(k_{x_g}^i, k_{y_g}^i, z_g, k_{x_s}^j, k_{y_s}^j, z_s, \omega) \\ &= \iiint_{-\infty}^{+\infty} \mathrm{d}x_1 \mathrm{d}y_1 \mathrm{d}z_1 G_0^i(k_{x_g}^i, k_{y_g}^i, z_g, x_1, y_1, z_1, \omega) V_1^{ij}(x_1, y_1, z_1) \\ &\qquad \times \phi_0^j(x_1, y_1, z_1, k_{x_s}^j, k_{y_s}^j, z_s, \omega) \\ &= \iiint_{-\infty}^{+\infty} \mathrm{d}x_1 \mathrm{d}y_1 \mathrm{d}z_1 \frac{e^{-\mathrm{i}(k_{x_g}^i x_1 + k_{y_g}^i y_1)} e^{\mathrm{i}\nu_g^i |z_g - z_1|}}{\mathrm{i}2\nu_g^i} V_1^{ij}(x_1, y_1, z_1) e^{\mathrm{i}(k_{x_s}^j x_1 + k_{y_s}^j y_1)} e^{\mathrm{i}\nu_s^j |z_1 - z_s|} \\ &= \frac{e^{-\mathrm{i}\nu_g^i z_g} e^{-\mathrm{i}\nu_s^j z_s}}{\mathrm{i}2\nu_g^i} \iiint_{-\infty}^{+\infty} \mathrm{d}x_1 \mathrm{d}y_1 \mathrm{d}z_1 e^{\mathrm{i}(k_{x_s}^j - k_{x_g}^i)x_1} e^{\mathrm{i}(k_{y_s}^j - k_{y_g}^i)y_1} e^{\mathrm{i}(\nu_s^j + \nu_g^i)z_1} V_1^{ij}(x_1, y_1, z_1) \\ &= \frac{e^{-\mathrm{i}\nu_g^i z_g} e^{-\mathrm{i}\nu_s^j z_s}}{\mathrm{i}2\nu_g^i} \hat{V}_1^{ij}(k_{x_s}^j - k_{x_g}^i, k_{y_s}^j - k_{y_g}^i, \nu_s^j + \nu_g^i | z_1) \end{aligned} \tag{C.16}$$

Therefore,

$$\begin{aligned}\hat{V}_1^{ij}(k_{x_s}^j - k_{x_g}^i, k_{y_s}^j - k_{y_g}^i, \nu_s^j + \nu_g^i | z_1) \\ = \mathrm{i}2\nu_g^i e^{\mathrm{i}(\nu_g^i z_g + \nu_s^j z_s)} b_1^{ij}(k_{x_g}^i, k_{y_g}^i, z_g, k_{x_s}^j, k_{y_s}^j, z_s, \omega)\end{aligned} \tag{C.17}$$

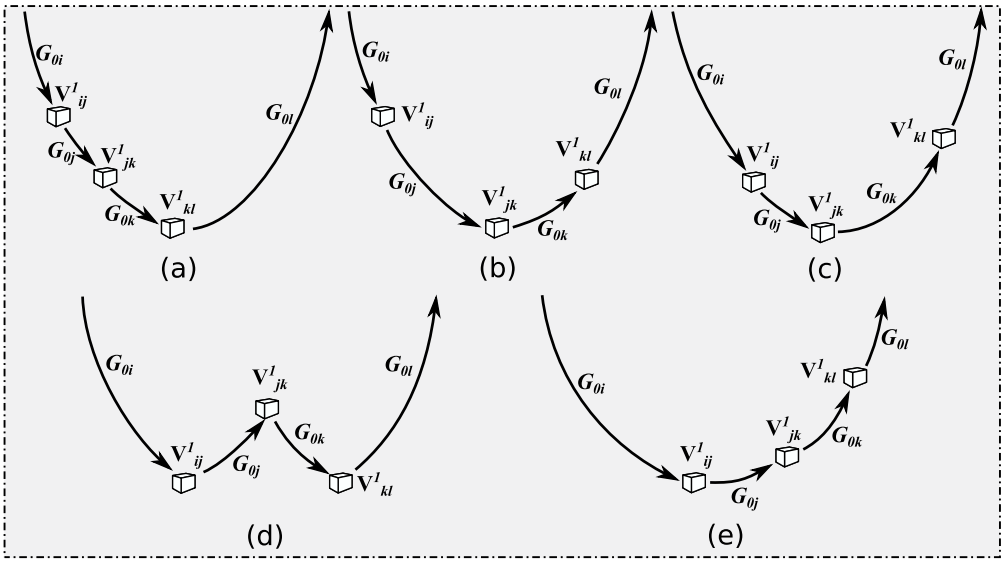

Figure C.2: Contributions of $G_0^i V_{33}^{ij} \phi_0^j$ depending on variant depth (z_1, z_2, z_3) relations between perturbations. (a) case of $z_1 < z_2 < z_3$, (b) case of $z_1 < z_3 < z_2$, (c) case of $z_3 < z_1 < z_2$, (d) case of $z2 < z_1$ and $z_2 < z_3$, (e) case of $z_3 < z_2 < z_1$.

The 1st-order internal multiple can be generated at least 3 perturbations which satisfy lower-higher-lower relationship in pseudo-depth (depth in reference medium). By analyzing 3rd order in inverse scattering series (Eq.C.15c), we have,

$$\begin{aligned}G_0^i V_3^{ij} \phi_0^j &= -(G_0^i V_2^{ik} G_0^k V_1^{kj} \phi_0^j + G_0^i V_1^{ik} G_0^k V_2^{kj} \phi_0^j + G_0^i V_1^{ik} G_0^k V_1^{kl} G_0^l V_1^{lj} \phi_0^j) \\ &= G_0^i V_{31}^{ij} \phi_0^j + G_0^i V_{32}^{ij} \phi_0^j + G_0^i V_{33}^{ij} \phi_0^j\end{aligned} \tag{C.18}$$

The first two terms in 3rd-order have no contribution to internal multiple (they only contribute to primary energy, see analysis discussed by Araújo (1994)). The 3rd term $G_0^i V_{33}^{ij} \phi_0^j$ represents several different wave propagations through three perturbations depending on the variant depth relations between perturbations (Figure C.2).

Consider all possible wave propagations involved by $G_0^i V_1^{ik} G_0^k V_1^{kl} G_0^l V_1^{lj} \phi_0^j$, only one certain wave path, with perturbations satisfying lower-higher-lower relationship in pseudo-depth, has

contribution to 1st-order internal multiples, shown in Figure C.2d, can be expressed as,

$$
\begin{aligned}
&W_{33}^{ij}(k_{x_g}^i, k_{y_g}^i, z_g, k_{x_s}^j, k_{y_s}^j, z_s, \omega) \\
&= -\iiint_{-\infty}^{+\infty} \mathrm{d}x_1\mathrm{d}y_1\mathrm{d}z_1\, G_0^i(k_{x_g}^i, k_{y_g}^i, z_g, x_1, y_1, z_1, \omega)\, V_1^{ik}(x_1, y_1, z_1) \\
&\quad \times \iiint_{-\infty}^{z_1} \mathrm{d}x_2\mathrm{d}y_2\mathrm{d}z_2\, G_0^k(x_1, y_1, z_1, x_2, y_2, z_2, \omega)\, V_1^{kl}(x_2, y_2, z_2) \\
&\quad \times \iiint_{z_2}^{+\infty} \mathrm{d}x_3\mathrm{d}y_3\mathrm{d}z_3\, G_0^l(x_2, y_2, z_2, x_3, y_3, z_3, \omega) \\
&\quad \times V_1^{lj}(x_3, y_3, z_3)\phi_0^j(x_3, y_3, z_3, k_{x_s}^j, k_{y_s}^j, z_s, \omega) \\
&= -\frac{1}{(2\pi)^4} \iiiint_{-\infty}^{+\infty} \mathrm{d}k_{x_1}^k \mathrm{d}k_{y_1}^k \mathrm{d}k_{x_2}^l \mathrm{d}k_{y_2}^l \frac{e^{-\mathrm{i}(\nu_s^j z_s + \nu_g^i z_g)}}{(\mathrm{i}2\nu_g^i)(\mathrm{i}2\nu_1^k)(\mathrm{i}2\nu_2^l)} \\
&\quad \times \iiint_{-\infty}^{+\infty} \mathrm{d}x_1\mathrm{d}y_1\mathrm{d}z_1 e^{\mathrm{i}(k_{x_1}^k - k_{x_g}^i)x_1} e^{\mathrm{i}(k_{y_1}^k - k_{y_g}^i)y_1} e^{\mathrm{i}(\nu_1^k + \nu_g^i)z_1}\, V_1^{ik}(x_1, y_1, z_1) \\
&\quad \times \iiint_{-\infty}^{z_1} \mathrm{d}x_2\mathrm{d}y_2\mathrm{d}z_2 e^{\mathrm{i}(k_{x_2}^l - k_{x_1}^k)x_2} e^{\mathrm{i}(k_{y_2}^l - k_{y_1}^k)y_2} e^{-\mathrm{i}(\nu_2^l + \nu_1^k)z_2}\, V_1^{kl}(x_2, y_2, z_2) \\
&\quad \times \iiint_{z_2}^{+\infty} \mathrm{d}x_3\mathrm{d}y_3\mathrm{d}z_3 e^{\mathrm{i}(k_{x_s}^j - k_{x_2}^l)x_3} e^{\mathrm{i}(k_{y_s}^j - k_{y_2}^l)y_3} e^{\mathrm{i}(\nu_s^j + \nu_2^l)z_3}\, V_1^{lj}(x_3, y_3, z_3) \\
&= -\frac{1}{(2\pi)^4} \iiiint_{-\infty}^{+\infty} \mathrm{d}k_{x_1}^k \mathrm{d}k_{y_1}^k \mathrm{d}k_{x_2}^l \mathrm{d}k_{y_2}^l \frac{e^{-\mathrm{i}(\nu_s^j z_s + \nu_g^i z_g)}}{(\mathrm{i}2\nu_g^i)(\mathrm{i}2\nu_1^k)(\mathrm{i}2\nu_2^l)} \\
&\qquad\qquad \times \hat{V}_1^{jk}(k_{x_1}^k - k_{x_g}^i, k_{y_1}^k - k_{y_g}^i, \nu_1^k + \nu_g^i | z_1) \\
&\qquad\qquad \times \hat{V}_1^{kl}(k_{x_2}^l - k_{x_1}^k, k_{y_2}^l - k_{y_1}^k, -\nu_2^l - \nu_1^k | z_2 < z_1) \\
&\qquad\qquad \times \hat{V}_1^{lj}(k_{x_s}^j - k_{x_2}^l, k_{y_s}^j - k_{y_2}^l, \nu_s^j + \nu_2^l | z_3 > z_2)
\end{aligned}
\tag{C.19}
$$

Replacing the elastic scattering potential by the weighted decomposed measured data based on their relations discussed above in equation C.17, the contributed calculation of elastic internal multiple with three perturbations (Eq.C.19) can be reword as a function of

weighted data, shown as,

$$
\begin{aligned}
&W_{33}^{ij}(k_{x_g}^i, k_{y_g}^i, z_g, k_{x_s}^j, k_{y_s}^j, z_s, \omega) \\
&= -\frac{1}{(2\pi)^4} \iiiint_{-\infty}^{+\infty} \mathrm{d}k_{x_1}^k \mathrm{d}k_{y_1}^k \mathrm{d}k_{x_2}^l \mathrm{d}k_{y_2}^l e^{\mathrm{i}\nu_1^k(z_s - z_g)} e^{-\mathrm{i}\nu_2^l(z_s - z_g)} \\
&\qquad \times b_1^{ik}(k_{x_g}^i, k_{y_g}^i, k_{x_1}^k, k_{y_1}^k, \nu_1^k + \nu_g^i | z_1) \\
&\qquad \times b_1^{kl}(k_{x_1}^k, k_{y_1}^k, k_{x_2}^l, k_{y_2}^l, -\nu_2^l - \nu_1^k | z_2 < z_1) \\
&\qquad \times b_1^{lj}(k_{x_2}^l, k_{y_2}^l, k_{x_s}^j, k_{y_s}^j, \nu_s^j + \nu_2^l | z_3 > z_2)
\end{aligned}
\tag{C.20}
$$

An inverse Fourier transform is performed to transfer the weighted data b_1^{ij} into pseudo-depth domain. Then, the 1st-leading-order elastic internal multiples prediction algorithm can be obtained, and is written as,

$$
\begin{aligned}
&b_3^{ij}(k_{x_g}^i, k_{y_g}^i, k_{x_s}^j, k_{y_s}^j, \omega) \\
&= -\frac{1}{(2\pi)^4} \iiiint_{-\infty}^{+\infty} \mathrm{d}k_{x_1}^k \mathrm{d}k_{y_1}^k \mathrm{d}k_{x_2}^l \mathrm{d}k_{y_2}^l e^{\mathrm{i}\nu_1^k(z_s - z_g)} e^{-\mathrm{i}\nu_2^l(z_s - z_g)} \\
&\qquad \times \int_{-\infty}^{+\infty} \mathrm{d}z_1 e^{\mathrm{i}(\nu_1^k + \nu_g^i)z_1} b_1^{ik}(k_{x_g}^i, k_{y_g}^i, k_{x_1}^k, k_{y_1}^k, z_1) \\
&\qquad \times \int_{-\infty}^{z_1} \mathrm{d}z_2 e^{-\mathrm{i}(\nu_2^l + \nu_1^k)z_2} b_1^{kl}(k_{x_1}^k, k_{y_1}^k, k_{x_2}^l, k_{y_2}^l, z_2) \\
&\qquad \times \int_{z_2}^{+\infty} \mathrm{d}z_3 e^{\mathrm{i}(\nu_s^j + \nu_2^l)z_2} b_1^{lj}(k_{x_2}^l, k_{y_2}^l, k_{x_s}^j, k_{y_s}^j, z_3)
\end{aligned}
\tag{C.21}
$$

To reconstruct 2nd-order internal multiples, at least five perturbations have to be involved to calculate the contributions for 2nd-order internal multiples. Simply expand equation C.20 into five perturbation mode, 2nd-order internal multiples prediction can be expressed as, in

vertical wavenumber domain,

$$
\begin{aligned}
&b_5^{ij}(k_{x_g}^i, k_{y_g}^i, k_{x_s}^j, k_{y_s}^j, \omega) \\
&= -\frac{1}{(2\pi)^8} \iiiint_{-\infty}^{+\infty} \mathrm{d}k_{x_1}^k \mathrm{d}k_{y_1}^k \mathrm{d}k_{x_2}^l \mathrm{d}k_{y_2}^l e^{\mathrm{i}\nu_1^k(z_s-z_g)} e^{-\mathrm{i}\nu_2^l(z_s-z_g)} \\
&\quad \times \iiiint_{-\infty}^{+\infty} \mathrm{d}k_{x_3}^m \mathrm{d}k_{y_3}^m \mathrm{d}k_{x_4}^n \mathrm{d}k_{y_4}^n e^{\mathrm{i}\nu_3^m(z_s-z_g)} e^{-\mathrm{i}\nu_4^n(z_s-z_g)} \\
&\quad \times b_1^{ik}(k_{x_g}^i, k_{y_g}^i, k_{x_1}^k, k_{y_1}^k, \nu_1^k + \nu_g^i | z_1) \\
&\quad \times b_1^{kl}(k_{x_1}^k, k_{y_1}^k, k_{x_2}^l, k_{y_2}^l, -\nu_2^l - \nu_1^k | z_2 < z_1) \\
&\quad \times b_1^{lm}(k_{x_2}^l, k_{y_2}^l, k_{x_3}^m, k_{y_3}^m, \nu_3^m + \nu_2^l | z_3 > z_2) \\
&\quad \times b_1^{mn}(k_{x_3}^m, k_{y_3}^m, k_{x_4}^n, k_{y_4}^n, -\nu_4^n - \nu_3^m | z_4 < z_3) \\
&\quad \times b_1^{nj}(k_{x_4}^n, k_{y_4}^n, k_{x_s}^j, k_{y_s}^j, \nu_s^j + \nu_4^n | z_5 > z_4)
\end{aligned}
\tag{C.22}
$$

Rewrite equation C.20 and equation C.22 as,

$$
\begin{aligned}
&b_3^{ij}(k_{x_g}^i, k_{y_g}^i, k_{x_s}^j, k_{y_s}^j, \omega) \\
&= -\frac{1}{(2\pi)^4} \iint_{-\infty}^{+\infty} \mathrm{d}k_{x_1}^k \mathrm{d}k_{y_1}^k e^{\mathrm{i}\nu_1^k(z_s-z_g)} b_1^{ik}(k_{x_g}^i, k_{y_g}^i, k_{x_1}^k, k_{y_1}^k, \nu_1^k + \nu_g^i | z_1) \\
&\qquad \times A_3^{kj}(k_{x_1}^k, k_{y_1}^k, k_{x_s}^j, k_{y_s}^j, \nu_1^k + \nu_s^j | z_1)
\end{aligned}
\tag{C.23a}
$$

$$
\begin{aligned}
&b_5^{ij}(k_{x_g}^i, k_{y_g}^i, k_{x_s}^j, k_{y_s}^j, \omega) \\
&= -\frac{1}{(2\pi)^8} \iint_{-\infty}^{+\infty} \mathrm{d}k_{x_1}^k \mathrm{d}k_{y_1}^k e^{\mathrm{i}\nu_1^k(z_s-z_g)} b_1^{ik}(k_{x_g}^i, k_{y_g}^i, k_{x_1}^k, k_{y_1}^k, \nu_1^k + \nu_g^i | z_1) \\
&\qquad \times A_5^{kj}(k_{x_1}^k, k_{y_1}^k, k_{x_s}^j, k_{y_s}^j, \nu_1^k + \nu_s^j | z_1)
\end{aligned}
\tag{C.23b}
$$

where,

$$
\begin{aligned}
&A_3^{kj}(k_{x_1}^k, k_{y_1}^k, k_{x_s}^j, k_{y_s}^j, \nu_1^k + \nu_s^j | z_1) \\
&= \iint_{-\infty}^{+\infty} \mathrm{d}k_{x_2}^l \mathrm{d}k_{y_2}^l e^{-\mathrm{i}\nu_2^l (z_s - z_g)} b_1^{kl}(k_{x_1}^k, k_{y_1}^k, k_{x_2}^l, k_{y_2}^l, -\nu_2^l - \nu_1^k | z_2 < z_1) \\
&\qquad \times b_1^{lj}(k_{x_2}^l, k_{y_2}^l, k_{x_s}^j, k_{y_s}^j, \nu_s^j + \nu_2^l | z_3 > z_2)
\end{aligned} \tag{C.24a}
$$

$$
\begin{aligned}
&A_5^{kj}(k_{x_1}^k, k_{y_1}^k, k_{x_s}^j, k_{y_s}^j, \nu_1^k + \nu_s^j | z_1) \\
&= \iint_{-\infty}^{+\infty} \mathrm{d}k_{x_2}^l \mathrm{d}k_{y_2}^l e^{-\mathrm{i}\nu_2^l (z_s - z_g)} b_1^{kl}(k_1^k, k_2^l, -\nu_2^l - \nu_1^k | z_2 < z_1) \\
&\times \iint_{-\infty}^{+\infty} \mathrm{d}k_{x_3}^m \mathrm{d}k_{y_3}^m e^{\mathrm{i}\nu_3^m (z_s - z_g)} b_1^{lm}(k_{x_2}^l, k_{y_2}^l, k_{x_3}^m, k_{y_3}^m, \nu_3^m + \nu_2^l | z_3 > z_2) \\
&\times \iint_{-\infty}^{+\infty} \mathrm{d}k_{x_4}^n \mathrm{d}k_{y_4}^n e^{-\mathrm{i}\nu_4^n (z_s - z_g)} b_1^{mn}(k_{x_3}^m, k_{y_3}^m, k_{x_4}^n, k_{y_4}^n, \nu_4^n + \nu_3^m | z_4 < z_3) \\
&\qquad \times b_1^{nj}(k_{x_4}^n, k_{y_4}^n, k_{x_s}^j, k_{y_s}^j, \nu_s^j + \nu_4^n | z_5 > z_4)
\end{aligned} \tag{C.24b}
$$

Analogously, nth-leading-order elastic internal multiples prediction algorithm can be expressed as, in vertical wavenumber domain,

$$
\begin{aligned}
&b_{2n+1}^{ij}(k_{x_g}^i, k_{y_g}^i, k_{x_s}^j, k_{y_s}^j, \omega) \\
&= -\frac{1}{(2\pi)^{2n}} \iint_{-\infty}^{+\infty} \mathrm{d}k_{x_1}^k \mathrm{d}k_{y_1}^k e^{\mathrm{i}\nu_1^k (z_s - z_g)} b_1^{ik}(k_{x_g}^i, k_{y_g}^i, k_{x_1}^k, k_{y_1}^k, \nu_1^k + \nu_g^i | z_1) \\
&\qquad \times A_{2n+1}^{kj}(k_{x_1}^k, k_{y_1}^k, k_{x_s}^j, k_{y_s}^j, \nu_1^k + \nu_s^j | z_1)
\end{aligned} \tag{C.25}
$$

where,

$$
\begin{aligned}
&A_{2n+1}^{kj}(k_{x_1}^k, k_{y_1}^k, k_{x_s}^j, k_{y_s}^j, \nu_1^k + \nu_s^j | z_1) \\
&= \iint_{-\infty}^{+\infty} \mathrm{d}k_{x_2}^l \mathrm{d}k_{y_2}^l e^{-\mathrm{i}\nu_2^l (z_s - z_g)} b_1^{kl}(k_{x_1}^k, k_{y_1}^k, k_{x_2}^l, k_{y_2}^l, -\nu_2^l - \nu_1^k | z_2 < z_1) \\
&\times \iint_{-\infty}^{+\infty} \mathrm{d}k_{x_3}^m \mathrm{d}k_{y_3}^m e^{\mathrm{i}\nu_3^m (z_s - z_g)} b_1^{lm}(k_{x_2}^l, k_{y_2}^l, k_{x_3}^m, k_{y_3}^m, \nu_3^m + \nu_2^l | z_3 > z_2) \\
&\qquad \times A_{2n-1}^{mj}(k_{x_3}^m, k_{y_3}^m, k_{x_s}^j, k_{y_s}^j, \nu_3^m + \nu_s^j | z_3)
\end{aligned} \tag{C.26}
$$

Again, take an inverse Fourier transform to perform the input data into pseudo-depth domain, nth-leading-order elastic internal multiples prediction algorithm can be written as,

in pseudo-depth domain,

$$
\begin{aligned}
b_{2n+1}^{ij}(k_{x_g}^i, k_{y_g}^i, k_{x_s}^j, k_{y_s}^j, \omega) = & -\frac{1}{(2\pi)^{2n}} \iint_{-\infty}^{+\infty} \mathrm{d}k_{x_1}^k \mathrm{d}k_{y_1}^k \, e^{\mathrm{i}\nu_1^k (z_s - z_g)} \\
& \times \int_{-\infty}^{+\infty} \mathrm{d}z_1 e^{\mathrm{i}(\nu_1^k + \nu_g^i) z_1} \, b_1^{ik}(k_{x_g}^i, k_{y_g}^i, k_{x_1}^k, k_{y_1}^k, z_1) \\
& \times A_{2n+1}^{kj}(k_{x_1}^k, k_{y_1}^k, k_{x_s}^j, k_{y_s}^j, z_1)
\end{aligned} \tag{C.27}
$$

where,

$$
\begin{aligned}
A_3^{kj}(k_{x_1}^k, k_{y_1}^k, k_{x_s}^j, k_{y_s}^j, z_1) = & \iint_{-\infty}^{+\infty} \mathrm{d}k_{x_2}^l \mathrm{d}k_{y_2}^l e^{-\mathrm{i}\nu_2^l (z_s - z_g)} \\
& \times \int_{-\infty}^{z1} \mathrm{d}z_2 e^{-\mathrm{i}(\nu_2^l + \nu_1^k) z_2} \, b_1^{kl}(k_{x_1}^k, k_{y_1}^k, k_{x_2}^l, k_{y_2}^l, z_2) \\
& \times \int_{z_2}^{+\infty} \mathrm{d}z_3 e^{\mathrm{i}(\nu_s^j + \nu_2^l) z_2} \, b_1^{lj}(k_{x_2}^l, k_{y_2}^l, k_{x_s}^j, k_{y_s}^j, z_3)
\end{aligned} \tag{C.28a}
$$

$$
\begin{aligned}
A_{2n+1}^{kj}(k_{x_1}^k, k_{y_1}^k, k_{x_s}^j, k_{y_s}^j, z_1) = & \iint_{-\infty}^{+\infty} \mathrm{d}k_{x_2}^l \mathrm{d}k_{y_2}^l e^{-\mathrm{i}\nu_2^l (z_s - z_g)} \\
& \times \int_{-\infty}^{z1} \mathrm{d}z_2 e^{-\mathrm{i}(\nu_2^l + \nu_1^k) z_2} \, b_1^{kl}(k_{x_1}^k, k_{y_1}^k, k_{x_2}^l, k_{y_2}^l, z_2) \\
& \times \int_{-\infty}^{+\infty} \mathrm{d}k_{x_3}^m \mathrm{d}k_{y_3}^m e^{\mathrm{i}\nu_3^m (z_s - z_g)} \\
& \times \int_{z_2}^{+\infty} \mathrm{d}z_3 e^{\mathrm{i}(\nu_3^m + \nu_2^l) z_3} \, b_1^{lm}(k_{x_2}^l, k_{y_2}^l, k_{x_3}^m, k_{y_3}^m, z_3) \\
& \times A_{2n-1}^{mj}(k_{x_3}^m, k_{y_3}^m, k_{x_s}^j, k_{y_s}^j, z_3)
\end{aligned} \tag{C.28b}
$$

Here, the letter subscripts denote the modes of wave $\{P, SH, SV\}$, and the number subscripts describe the locations.

Bibliography

Abma, R., and Kabir, N., 2006, 3d interpolation of irregular data with a pocs algorithm: Geophysics, **71**, No. 6, E91–E97.

Araújo, F. V., 1994, Linear and non-linear methods derived from scattering theory: backscattered tomography and internal multiple attenuation: Ph.D. thesis, Universidade Federal da Bahia.

Behura, J., Wapenaar, K., and Snieder, R., 2014, Autofocus imaging: Image reconstruction based on inverse scattering theory: Geophysics, **79**, No. 3, A19–A26.

Berkhout, A., 2006, Seismic processing in the inverse data space: Geophysics, **71**, No. 4, A29–A33.

Berkhout, A., and Verschuur, D., 2005, Removal of internal multiples with the common-focus-point (cfp) approach: Part 1explanation of the theory: Geophysics, **70**, No. 3, V45–V60.

Bohlen, T., 2002, Parallel 3-d viscoelastic finite difference seismic modelling: Computers & Geosciences, **28**, No. 8, 887–899.

Coates, R., Weglein, A. et al., 1996, Internal multiple attenuation using inverse scattering: Results from prestack 1 & 2d acoustic and elastic synthetics: SEG Expanded Abstracts.

da Costa Filho, C. A., Meles, G. A., and Curtis, A., 2017, Elastic internal multiple analysis and attenuation using Marchenko and interferometric methods: Geophysics, **82**, No. 2, Q1–Q12.

de Melo, F., Idris, M., Wu, J., and Kostov, C., 2014, Cascaded internal multiple attenuation with inverse scattering series: Western Canada case study: SEG Expanded Abstracts.

de Melo, F., Kostov, C., and Wu, J., 2015, Internal multiple attenuation on radial gathers with inverse scattering series prediction: EAGE Expanded Abstracts.

Diebold, J. B., and Stoffa, P. L., 1981, The traveltime equation, tau-p mapping, and inversion of common midpoint data: Geophysics, **46**, No. 3, 238–254.

Dougherty, M. E., and Stephen, R. A., 1988, Seismic energy partitioning and scattering in laterally heterogeneous ocean crust, *in* Scattering and Attenuations of Seismic Waves, Part I, Springer, 195–229.

Etgen, J. T., 1988, Elastic prestack migration of two component data, Tech. Rep. 57, SEP.

Foster, D. J., and Mosher, C. C., 1992, Suppression of multiple reflections using the radon transform: Geophysics, **57**, No. 3, 386–395.

Fu, Q., Luo, Y., Kelamis, P. G., Huo, S., Sindi, G., and Weglein, A. B., 2010, The inverse scattering series approach towards the elimination of land internal multiples: SEG Expanded Abstracts.

Hampson, D., 1986, Inverse velocity stacking for multiple elimination, *in* SEG Technical Program Expanded Abstracts 1986, Society of Exploration Geophysicists, 422–424.

Hernandez, M., and Innanen, K., 2014, Identifying internal multiples using 1d prediction: physical modelling and land data examples: Canadian Journal of Geophysical Exploration, **39**, No. 1, 37–47.

Herrera, W., and Weglein, A. B., 2013a, Eliminating first-order internal multiples with downward reflection at the shallowest interface: Theory and initial examples, *in* SEG Technical Program Expanded Abstracts 2013, Society of Exploration Geophysicists, 4131–4135.

Herrera, W., and Weglein, A. B., 2013b, Eliminating first-order internal multiples with downward reflection at the shallowest interface: theory and initial examples: SEG Technical Program Expanded Abstracts, **83**, 4131–4135.

Innanen, K. A., 2017, Time-and offset-domain internal multiple prediction with nonstationary parameters: Geophysics, **82**, No. 2, V105–V116.

Innanen, K. A. H., and Pan, P., 2015, Large dip artifacts in 1.5d internal multiple prediction and their mitigation: CSEG Geoconvention.

Keating, S., Sun, J., Pan, P., Innanen, K. A. H., Trad, D., and Geng, Y., 2016, Nonstationary l1 adaptive subtrraction with application to internal multiple attenuation: CSEG Geoconvention.

Kelamis, P. G., Erickson, K. E., Verschuur, D. J., and Berkhout, A., 2002, Velocity-independent redatuming: A new approach to the near-surface problem in land seismic data processing: The Leading Edge, **21**, No. 8, 730–735.

Li, Z., Li, Z., Wang, P., and Zhang, M., 2016, Reverse time migration of multiples based on different-order multiple separation: Geophysics, **82**, No. 1, S19–S29.

Liu, F., Sen, M. K., and Stoffa, P. L., 2000, Dip selective 2-d multiple attenuation in the plane-wave domain: Geophysics, **65**, No. 1, 264–274.

Liu, Y., Chang, X., Jin, D., He, R., Sun, H., and Zheng, Y., 2011, Reverse time migration of multiples for subsalt imaging: Geophysics, **76**, No. 5, WB209–WB216.

Löer, K., Curtis, A., and Meles, G. A., 2016, Relating source-receiver interferometry to an inverse-scattering series to derive a new method to estimate internal multiples: Geophysics, **81**, No. 3.

Lumley, D. E., Nichols, D., Rekdal, T. et al., 1995, Amplitude-preserved multiple suppression, *in* 1995 SEG Annual Meeting, Society of Exploration Geophysicists.

Luo, Y., Kelamis, P. G., Fu, Q., Huo, S., Sindi, G., Hsu, S.-Y., and Weglein, A. B., 2011, Elimination of land internal multiples based on the inverse scattering series: The Leading Edge, **30**, No. 8, 884–889.

Luo, Y., Zhu, W., Kelamis, P. G. et al., 2007, Internal multiple reduction in inverse-data domain: SEG Expanded Abstracts. San Antonio:[sn], 125–129.

Ma, J., Sen, M. K., and Chen, X., 2009, Free-surface multiple attenuation using inverse data processing in the coupled plane-wave domain: Geophysics, **74**, No. 4, V75–V81.

Malcolm, A. E., and de Hoop, M. V., 2005, A method for inverse scattering based on the generalized bremmer coupling series: Inverse Problems, **21**, No. 3, 1137.

Malcolm, A. E., De Hoop, M. V., and Ursin, B., 2011, Recursive imaging with multiply scattered waves using partial image regularization: A north sea case study: Geophysics, **76**, No. 2, B33–B42.

Malcolm, A. E., Ursin, B., and De Hoop, M. V., 2009, Seismic imaging and illumination with internal multiples: Geophysical Journal International, **176**, No. 3, 847–864.

Matson, K. H., 1997, An inverse-scattering series method for attenuating elastic multiples from multicomponent land and ocean bottom seismic data: Ph.D. thesis, University of British Columbia.

Matson, K. H., and Weglein, A. B., 1996, Removal of elastic interface multiples from land and ocean bottom data using inverse scattering: SEG Expanded Abstracts, 1526–1530.

Morse, P. M., and Feshbach, H., 1953, Methods of theoretical physics: McGraw-Hill Book Co.

Nita, B. G., and Weglein, A. B., 2009a, Pseudo-depth / intercept-time monotonicity requirements in the inverse scattering algorithm for predicting internal multiple reflections: Communications in Computational Physics, **5**, No. 1, 163–182.

Nita, B. G., and Weglein, A. B., 2009b, Pseudo-depth/intercept-time monotonicity requirements in the inverse scattering algorithm for predicting internal multiple reflections: Communications in Computational Physics, **5**, No. 1, 163.

Ocola, L. C., 1972, A nonlinear least-squares method for seismic refraction mapping-part ii: Model studies and performance of reframap method: Geophysics, **37**, No. 2, 273–287.

Pan, P., 2015, 1.5 d internal multiple prediction: an application on synthetic data, physical modelling data and land data synthetics: Ph.D. thesis, University of Calgary.

Peacock, K., and Treitel, S., 1969, Predictive deconvolution: Theory and practice: Geophysics, **34**, No. 2, 155–169.

Ramirez, A., and Weglein, A., 2005, Progressing the analysis of the phase and amplitude prediction properties of the inverse scattering internal multiple attenuation algorithm: Journal of Seismic Exploration, **13**, No. 3, 283–301.

Ramirez, A. C., Antal, A., and Sigernes, L. T. W., 2015, Internal multiple study on Asgard fields Smørbuk and Smørbukk Sør, *in* Proceedings of the 77th EAGE conference & exhibition, Madrid, Spain, EAGE.

Ramírez, A. C., and Weglein, A., 2005, Progressing the analysis of the phase and amplitude prediction properties of the inverse scattering internal multiple attenuation algorithm.: J. of Seismic Expl., **13**, 283–301.

Ras, P., Volterrani, S., Hannan, A., Rao, N., Al-Ashwak, S., Kidambi, V., and Al-Qadeeri, B., 2012, A well-driven interbed demultiple workflow for deep carbonate reservoirs of kuwait: EAGE Expanded Abstracts.

Sacchi, M. D., and Porsani, M., 1999, Fast high resolution parabolic radon transform, *in* SEG Technical Program Expanded Abstracts 1999, Society of Exploration Geophysicists, 1477–1480.

Schuster, G., Yu, J., Sheng, J., and Rickett, J., 2004, Interferometric/daylight seismic imaging: Geophysical Journal International, **157**, No. 2, 838–852.

Slob, E., Wapenaar, K., Broggini, F., and Snieder, R., 2014, Seismic reflector imaging using internal multiples with marchenko-type equations: Geophysics, **79**, No. 2, S63–S76.

Sonika, S., Zarkhidze, A., Heim, J., and Dragoset, W., 2012, Complementary data-driven methods for interbed demultiple of land data: EAGE Expanded Abstracts.

Stoffa, P. L., Sen, M. K., Seifoullaev, R. K., Pestana, R. C., and Fokkema, J. T., 2006, Plane-wave depth migration: Geophysics, **71**, No. 6, S261–S272.

Stolt, R. H., 1978, Migration by Fourier transform: Geophysics, **43**, No. 1, 23–48.

Stolt, R. H., and Weglein, A. B., 2012, Seismic imaging and inversion: Volume 1: Application of linear inverse theory, vol. 1: Cambridge University Press.

Sun, J., and Innanen, K. A. H., 2015, 1.5 d internal multiple prediction in the plane wave domain: CSEG Geoconvention.

Sun, J., and Innanen, K. A. H., 2016a, Extension of internal multiple prediction: 1.5 d to 2d in double plane wave domain: CSEG Geoconvention.

Sun, J., and Innanen, K. A. H., 2016b, Interbed multiple prediction on land: which technology, and which domain?: Recorder, **41**, No. 10, 24–29.

Sun, J., and Innanen, K. A. H., 2016c, Inverse-scattering series internal-multiple prediction in the double plane-wave domain, *in* SEG Technical Program Expanded Abstracts 2016, Society of Exploration Geophysicists, 4555–4560.

Sun, J., and Innanen, K. A. H., 2017, Multicomponent inverse scattering series internal multiple prediction in the tp domain, *in* 2017 SEG International Exposition and Annual Meeting, Society of Exploration Geophysicists.

Sun, J., and Innanen, K. A. H., 2018, Multidimensional inverse-scattering series internal multiple prediction in the coupled plane-wave domain: Geophysics, **83**, No. 2, V73–V82.

Sun, J., Innanen, K. A. H., Trad, D., and Geng, Y., 2018a, Multicomponent inverse scattering series internal multiple prediction part i: analysis of input preparation: CSEG Geoconvention.

Sun, J., Innanen, K. A. H., Trad, D., and Geng, Y., 2018b, Multicomponent inverse scattering series internal multiple prediction part ii: domains and implementions: CSEG Geoconvention.

Taner, M., 1980, Long period sea-floor multiples and their suppression: Geophysical Prospecting, **28**, No. 1, 30–48.

Trad, D., 2003, Interpolation and multiple attenuation with migration operators: Geophysics, **68**, No. 6, 2043–2054.

Trad, D., Ulrych, T., and Sacchi, M., 2003, Latest views of the sparse radon transform: Geophysics, **68**, No. 1, 386–399.

Trad, D. O., Ulrych, T. J., and Sacchi, M. D., 2002, Accurate interpolation with high-resolution time-variant radon transforms: Geophysics, **67**, No. 2, 644–656.

Treitel, S., Gutowski, P., and Wagner, D., 1982, Plane-wave decomposition of seismograms: Geophysics, **47**, No. 10, 1375–1401.

van Trier, J., 1985, Inversion of seismic data in the fourier domain and prestack stolt migration, Tech. Rep. 48, SEP.

Verschuur, D. J., 1991, Surface-related multiple elimination, an inversion approach: Ph.D. thesis, Technische Univ., Delft (Netherlands).

Verschuur, D. J., Berkhout, A. J., and Wapenaar, C. P. A., 1992, Adaptive surface-related multiple elimination: Geophysics, **57**, 1166–1177.

VerWest, B., 2002, Suppressing peg-leg multiples with parabolic radon demultiple, *in* 64th EAGE Conference & Exhibition.

Weglein, A. B., 2016, Multiples: Signal or noise?: Geophysics, **81**, No. 4, V283–V302.

Weglein, A. B., Araújo, F. V., Carvalho, P. M., Stolt, R. H., Matson, K. H., Coates, R. T., Corrigan, D., Foster, D. J., Shaw, S. A., and Zhang, H., 2003, Inverse scattering series and seismic exploration: Inverse problems, **19**, No. 6, R27.

Weglein, A. B., Gasparotto, F. A., Carvalho, P. M., and Stolt, R. H., 1997, An inverse-scattering series method for attenuating multiples in seismic reflection data: Geophysics, **62**, No. 6, 1975–1989.

Wu, Z. J., Sonika, S., and Dragoset, W., 2011, Robust internal multiple prediction: SEG Expanded Abstracts.

Yilmaz, Ö., 2001, Seismic data analysis, vol. 1: Society of Exploration Geophysicists Tulsa.

Zou, Y., and Weglein, A. B., 2013, A new method to eliminate first order internal multiples for a normal incidence plane wave on a 1d earth, *in* 2013 SEG Annual Meeting, Society of Exploration Geophysicists.

Zuberi, M., and Alkhalifah, T., 2014a, Generalized internal multiple imaging (gimi) using feynman-like diagrams: Geophysical Journal International, **197**, No. 3, 1582–1592.

Zuberi, M. A. H., and Alkhalifah, T., 2014b, Generalized internal multiple imaging: Geophysics, **79**, No. 5, S207–S216.